

RESERVOIR CAPACITY ESTIMATES IN SHALE PLAYS BASED ON EXPERIMENTAL
ADSORPTION DATA

by
Tan Ngo

A thesis submitted to the Faculty and the Board of Trustees of the Colorado School of Mines in partial fulfillment of the requirements for the degree of Master of Science (Petroleum Engineering)

Golden, Colorado

Date: _____

Signed: _____

Tan Ngo

Signed: _____

Dr. Ronny Pini

Thesis Advisor

Golden, Colorado

Date: _____

Signed: _____

Dr. Erdal Ozkan

Professor and Interim Head

Department of Petroleum Engineering

ABSTRACT

Fine-grained sedimentary rocks, such as mudrocks, are characterized by a complex porous framework containing pores in the nanometer range that can store a significant amount of natural gas (or any other fluids) through adsorption processes. Unfortunately, although the adsorbed gas can take up to a major fraction of the total gas-in-place in these reservoirs, the ability to produce it is limited, and the current technology focuses primarily on the free gas in the fractures. A better understanding and quantification of adsorption/desorption mechanisms in these rocks is therefore required, in order to allow for a more efficient and sustainable use of these resources. Additionally, while water is still predominantly used to fracture the rock, other fluids, such as supercritical CO₂ are being considered; here, the idea is to reproduce a similar strategy as for the enhanced recovery of methane in deep coal seams (ECBM). Also in this case, the feasibility of CO₂ injection and storage in hydrocarbon shale reservoirs requires a thorough understanding of the rock behavior when exposed to CO₂, thus including its adsorption characteristics. Shale reservoirs are widely distributed in the U.S. with existing infrastructures used for gas and oil production operation; should CO₂ injection in such reservoirs prove feasible, the capacity of geologic formations for CO₂ storage will increase significantly.

The main objectives of this Master's Thesis are as follows: (1) to identify the main controls on gas adsorption in mudrocks (TOC, thermal maturity, clay content, etc.); (2) to create a library of adsorption data measured on shale samples at relevant conditions and to use them for estimating GIP and gas storage in shale reservoirs; (3) to build an experimental apparatus to measure adsorption properties of supercritical fluids (such as CO₂ or CH₄) in microporous materials; (4) to measure adsorption isotherms on microporous samples at various temperatures and pressures.

The main outcomes of this Master's Thesis are summarized as follows. A review of the literature has been carried out to create a library of methane and CO₂ adsorption isotherms on shale samples from various formations worldwide. Large discrepancies have been found between estimates of the adsorbed gas density from different measurement techniques using representative fluids (such as CH₄ and CO₂) at elevated pressures, and the adsorbed density can range anywhere between the liquid and the solid state of the adsorbate. Whether these discrepancies are associated with the inherent heterogeneity of mudrocks and/or with poor data quality requires more experiments under well-controlled conditions. Nevertheless, it has been

found in this study that methane GIP estimates can vary between 10-45% and 10-30%, respectively, depending on whether the free or the total amount of gas is considered. Accordingly, CO₂ storage estimates range between 30-90% and 15-50%, due to the larger adsorption capacity and gas density at similar pressure and temperature conditions.

A manometric system has been designed and built that allows measuring the adsorption of supercritical fluids in microporous materials. Preliminary adsorption tests have been performed using a microporous 13X zeolite and CO₂ as an adsorbing gas at a temperature of 25°C and 35°C and at pressures up to 500 psi. Under these conditions, adsorption is quantified with a precision of +/- 3%. However, relative differences up to 15-20% have been observed with respect to data published in the literature on the same adsorbent and at similar experimental conditions. While it cannot be fully explained with uncertainty analysis, this discrepancy can be reduced by improving experiment practice, thus including the application of a higher adsorbent's regeneration temperature, of longer equilibrium times and of a careful flushing of the system between the various experimental steps.

Based on the results on 13X zeolite, virtual tests have been conducted to predict the performance of the manometric system to measure adsorption on less adsorbing materials, such as mudrocks. The results show that uncertainties in the estimated adsorbed amount are much more significant in shale material and they increase with increasing pressure. In fact, relative uncertainties in the adsorbed amount can reach up to 80 and 200% at 500 and 1600 psia, respectively. The latter can be reduced (i) by increasing the mass of adsorbent material (15.2% and 42.3% when the mass of adsorbent is doubled as compared to the experiment with 13X zeolite) and/or (ii) by increasing the precision of the pressure transducers (uncertainty is further reduced to 3% and 8.4% from case (i) when the transducers with 0.05% accuracy are used. These experiments are justified by the need of extending the current data set on gas adsorption of mudrocks, thus enabling a more reliable estimate on the available gas reserves in shale reservoir and the potential of carbon dioxide storage

TABLE OF CONTENTS

ABSTRACT	iii
LIST OF FIGURES	vii
LIST OF TABLES.....	ix
ACKNOWLEDGEMENTS	xi
CHAPTER 1	1
INTRODUCTION	1
1.1 Objectives	3
1.2 Organization of Thesis	4
2.1 Pore Structure of Shales	6
2.2 Concept of gas adsorption.....	7
2.2.1 Adsorption isotherm models	9
2.2.2 Interpreting adsorption through a graphical approach.....	10
2.3 Current data set of adsorption on shale samples	13
2.4 Controls on adsorption	22
2.4.1 Total Organic Carbon (TOC)	22
2.4.2 Thermal maturity.....	24
2.4.3 Clay Content.....	25
2.4.4 Moisture.....	26
2.4.5 Temperature and pressure.....	27
CHAPTER 3	28
USING ADSORPTION DATA FOR GIP AND STORAGE ESTIMATES	28
CHAPTER 4	32
DETERMINATION OF EXCESS ADSORPTION	32
4.1 Materials	32
4.2 Experimental Methods	32
4.3 Manometric Method.....	33
4.4 Virtual experiments	34
4.4.1 System volume calibration using helium gas	34
4.4.2 Adsorbent volume	38
4.4.3 CO ₂ excess adsorption on 13 X zeolite at 25°C and 35°C up to 500 psi	39
4.4.4 CO ₂ excess adsorption on 13X zeolite at 25°C and 35°C up to 1,600 psi	41
4.5 Experimental tests	42
4.5.1 System volume calibration using helium gas	42

4.5.2 Adsorbent volume	43
4.5.3. CO ₂ excess adsorption on 13X zeolite at 25°C and 35°C.....	44
4.6 Virtual tests on shale sample	48
4.6.1 CO ₂ excess adsorption on New Albany shale - Case 1	48
4.6.2 CO ₂ excess adsorption on New Albany shale- Case 2	49
4.6.2 CO ₂ excess adsorption on New Albany shale- Case 3	51
4.7 Other tests	52
4.7.1 Leak-off test	52
4.7.2 Blank test	52
CHAPTER 5	54
RESULTS AND DICUSSION	54
5.1. System volume	54
5.2 Excess adsorption.....	55
CHAPTER 6	58
CONCLUSIONS AND FUTURE RECOMMENDATIONS.....	58
6.1 Summary and conclusions	58
6.2 Future recommendations.....	59
LIST OF SYMBOLS.....	61
REFERENCE CITED	63
APPENDIX A-DERIVATION OF EQUATIONS AND UNIT CONVERSIONS	69
A.1 Unit Conversions.....	69
A.2 Derivation of Equations	70
A.2.1 Equation 4.1-Volume ratio in an empty system.....	70
A.2.2 Equation 4.2-Volume ratio with reference volume.....	71
A.2.3 Equation 4.3-Error analysis in adsorbent volume	71
A.2.4 Equation 4.4- Error analysis in excess adsorption	72
A.2.5 Equation 4.9- Excess adsorption amount	73
APPENDIX B- GRAPHICAL METHOD	74
APPENDIX C-LANGMUIR ADSORPTION ISOTHERM.....	76
APPENDIX D-VIRTUAL EXPERIMENT	78
D.1 Selection of apparatus size.....	78
D.2 Uncertainty in excess adsorption isotherm	81

LIST OF FIGURES

Figure 1.1: Map of the United States shale plays in the Lower 48 states. Sedimentary basins are highlighted in purple. Current plays are highlighted in red. Prospective future plays are highlighted in orange (EIA, 2013).	1
Figure 2.1: Images of the variegated population of pores the Barnett Shale sample. A) Spherical nanopores with diameter ranging from 18-46nm. B) Complex large pore structure (550 nm diameter). C) and D) Tube-like and elliptical pores (20nm). Images taken from secondary electron (Loucks et al., 2009).	6
Figure 2.2: Gas adsorption behavior within shale sample.	7
Figure 2.3: Excess adsorption isotherms of CO ₂ as a function of bulk density measured at 45°C on Permian Shale sample from Brazil. The dashed line has been used to fit a straight line to determine adsorbed gas density. This technique is known as Graphical method. (Weniger et al., 2010).	10
Figure 2.4: CH ₄ adsorption on North America shale plays. References are provided in Table 2.2. Note that 1MPa is approximately 145 psi.	16
Figure 2.5: CH ₄ adsorption from Europe shale reservoir. References are provided in Table 2.2. Note that 1MPa is approximately 145 psi.	17
Figure 2.6: CH ₄ adsorption from Asia shale reservoir. References are provided in Table 2.2. Note that 1MPa is approximately 145 psi.	18
Figure 2.7: CO ₂ adsorption from North and South America shale reservoir. References are provided in Table 2.3. Note that 1 MPa is approximately 145 psi.	19
Figure 2.8: CO ₂ adsorption from different type of clays. References are provided in Table 2.3. Note that 1MPa is approximately 145 psi.	20
Figure 3.1: Percent difference between Ambrose method and conventional method for CH ₄	30
Figure 3.2: Percent difference between Ambrose method and conventional method for CO ₂	31
Figure 4.1: Schematic diagram of the manometric system	34
Figure 4.2: Figure illustrates the standard deviation of dose volume value if system volume is 82.2 cm ³	36
Figure 4.3: Figure illustrates the standard deviation of dose volume value if system volume is 150 cm ³	37
Figure 4.4: Figure illustrates the standard deviation of dose volume value if system volume is 400 cm ³	38

Figure 4.5: CO ₂ excess adsorption isotherm at 25°C and 35°C as a function of equilibrium pressure. Note that the uncertainty of dose volume, uptake volume and adsorbent volume also included here in this plot. The relative error of excess adsorption at 500 psi for 25°C and 35°C are approximately 1.6%.	40
Figure 4.6: CO ₂ excess adsorption isotherm at 25°C and 35°C as a function of equilibrium density. Note that the uncertainty of dose volume, uptake volume and adsorbent volume also included here in this plot. The relative error of excess adsorption at 1,600 psi for 25°C and 35°C are 19.9% and 18.6%, respectively.	41
Figure 4.7: CO ₂ excess adsorption isotherm at 25°C and 35°C as a function of equilibrium pressure. The relative error of excess adsorption at 500 psi for 25°C and 35°C are 2.6% and 2.5%, respectively.....	46
Figure 4.8: CO ₂ excess adsorption isotherm at 25°C and 35°C as a function of equilibrium density. The relative error of excess adsorption at 500 psi for 25°C and 35°C are 2.6% and 2.5%, respectively.	47
Figure 4.9: CO ₂ excess adsorption isotherm of New Albany shale as a function of equilibrium pressure as computed from a virtual experiment together with experimental data from Chareonsuppanimit et al. (2012). Error bars and percentage error of excess adsorption are also included in the plot. Mass of adsorbent sample is 22.695 g.	49
Figure 4.10: CO ₂ excess adsorption isotherm of New Albany shale as a function of equilibrium pressure as computed from a virtual experiment together with experimental data from Chareonsuppanimit et al. (2012). Error bars and percentage error of excess adsorption are also included in the plot. Mass of adsorbent sample is 50g.....	50
Figure 4.11: CO ₂ excess adsorption isotherm of New Albany shale as a function of equilibrium pressure as computed from a virtual experiment together with experimental data from Chareonsuppanimit et al. (2012). Error bars and percentage error of excess adsorption are also included in the plot. Mass of adsorbent sample is 50g in this case and uncertainty in pressure gauge is 0.05%.	51
Figure 4.12: Excess adsorption from blank test at 25°C. The blank test results have been corrected with excess adsorption data from 13X zeolite.....	53
Figure 5.1: CO ₂ excess adsorption on 13X zeolite at 25°C and 35°C obtained from this study and Cavenati study (Cavenati et al., 2004).....	55
Figure B.1: Excess adsorption isotherms of CO ₂ as a function of bulk density measured at 45°C on Permian shale sample. The dashed line has been used to fit a straight line to determine adsorbed gas density. This technique is known as Graphical Method. Weniger et al. (2012)	75
Figure D.1: Uncertainty in excess adsorption for New Albany shale using virtual test.	80

LIST OF TABLES

Table 2.1: Density of adsorbed CH ₄ and CO ₂ using different approaches and adsorbent materials.....	12
Table 2.2: Adsorption data set from multiple unconventional plays around the world on CH ₄	14
Table 2.3: Adsorption data set from multiple unconventional plays around the world on CO ₂	15
Table 2.4: A review on the effect of different properties of shale sample on excess adsorbed amount. The effects are shown with three abbreviations: N (negative), P (positive), n/a (Not available)	23
Table 3.1: Shale and reservoir properties using to estimate GIP (CH ₄) and gas storage capacity (CO ₂).....	29
Table 4.1: Equipment used for adsorption experiment.....	33
Table 4.2: Uncertainty results of dose volume, uptake volume, and adsorbent volume from Virtual experiment.	39
Table 4.3: Inputs used to determine adsorption isotherm curve of 13X zeolite in virtual experiment at 25°C and 35°C.	40
Table 4.4: Volume ratio between uptake volume and dose volume from helium gas expansion in empty system volume.....	42
Table 4.5: Value of dose volume and uptake volume from helium gas expansion at different pressure step and their standard deviation	43
Table 4.6: Results of 13X zeolite volumes from helium gas expansion.	44
Table 4.7: Excess adsorption results at 25°C on 13X zeolite	46
Table 4.8: Excess adsorption results at 35°C on 13X zeolite.	46
Table 4.9: Parameters used to plot excess adsorption isotherm in New Albany shale in Case 1.	48
Table 4.10: Adsorption parameters used to plot excess adsorption in New Albany shale in Case 2.	50
Table 4.11: Adsorption parameters used to plot excess adsorption in New Albany shale in Case 3.	51
Table 4.12: Excess adsorption results from blank test at 25°C.....	53
Table 5.1: Uncertainty in dose volume, uptake volume and adsorbent volume at different system volumes.	54

Table 5.2: Uncertainties in dose volume, uptake volume and adsorbent volume from Virtual and Experimental test.	54
Table 5.3: CO ₂ adsorption of 13X zeolite at different regenerating temperature.....	57
Table B.1: Excess adsorption data from Permian shale in Brazil (Weniger et al., 2010).....	74
Table C.1: Excess adsorption data from Permian shale in Brazil (Weniger et al., 2010).....	76
Table C.2: Adsorption parameters b and q_{sc} obtained from Langmuir adsorption model. The adsorption isotherm curve is from Permian shale in Brazil (Weniger et al., 2010).....	77
Table D.1: An example of virtual experiment in an empty volume system to determine volume ratio. This example is conducted for 400 cm ³ volume system.....	80
Table D.2: An example of virtual experiment in a system with reference volume to determine dose volume and uptake volume. This example is conducted for 400 cm ³ volume system.....	80
Table D.3: Input parameters used to determine uncertainty in excess adsorption of New Albany shale.....	81
Table D.4: Calculation and results of excess adsorption in New Albany shale using virtual test.....	82

ACKNOWLEDGEMENTS

First, I would like to express my deepest gratitude to my advisor Dr. Ronny Pini for his continuous support, patience, encouragement and immense knowledge during my M.Sc study and research. His guidance and insightful thoughts helped me in this research and writing of this thesis. I could not have imagined having a better advisor.

I would also like to thank my thesis committee members, Dr. Ramona Graves, Dr. Azra Tutuncu for their support and insightful comments. I am extending my sincere gratitude to Dr. Graves for financial support of my master program and to Dr. Tutuncu for her lab equipment support.

Special thanks go out to Joe Chen for his ideas and assistance in installing the manometric system. I am sincerely grateful for his time and sharing his expertise.

I would also like to extend my appreciation to all the students, professors, and faculties in the Petroleum Engineering Department of the Colorado School of Mines for their help. Specially, I appreciate Denise Winn-Bower, Patti Hassen, and Terri Snyder for their generous assistance and support.

I would like to thank my grandparents, parents, uncles and aunts, brother and sisters, and all my relatives. They were always supporting, believing, and encouraging me throughout my lifetime of education. Without their unconditional loves and support, I would not be able to be the person I am today.

I would also like to thank my friends at Colorado School of Mines, Abdulla Kerimov, Binh Bui, Olawale Adekunle, Ogemdi Isiguzo, Cedric Sedro, Susanna Brusio, Guillermo Gallego, and many others for their friendship and support during my study at Colorado School of Mines. They each gave me a great memories and made my time here an unforgettable experience.

CHAPTER 1 INTRODUCTION

The large volumes of newfound shale gas reserves indicate that this resource will play a major role in maintaining and securing future energy supply. In 2013, the U.S Energy Information Administration (EIA, 2013) reported that there are 6,634 trillion cubic feet of technically recoverable shale gas outside the U.S. and 665 trillion cubic feet within the country (EIA, 2013). A summary of where these plays occur in the U.S. is shown in Figure 1.1.

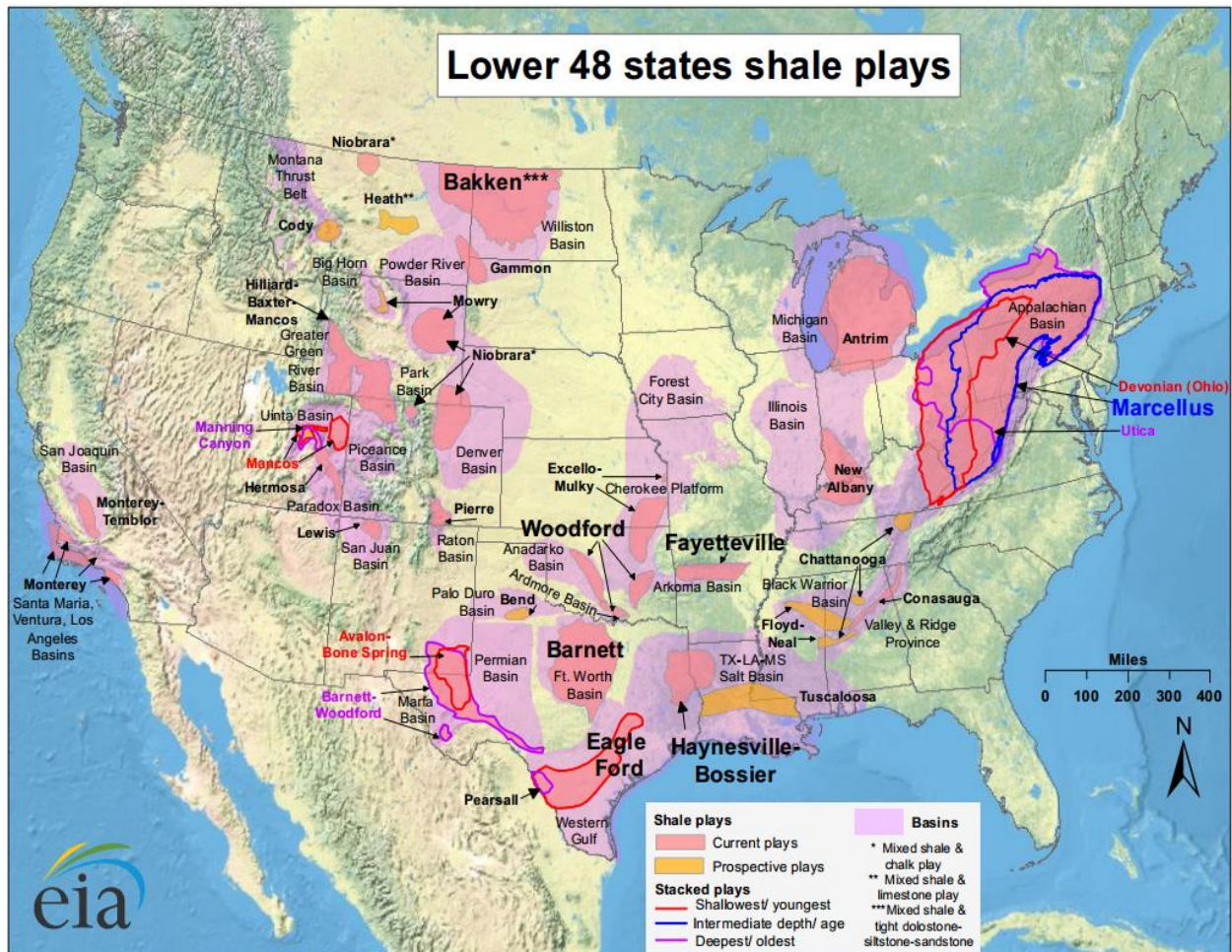


Figure 1.1: Map of the United States shale plays in the Lower 48 states. Sedimentary basins are highlighted in purple. Current plays are highlighted in red. Prospective future plays are highlighted in orange (EIA, 2013).

However, despite major recent advances in drilling and completion technology, these plays are still poorly exploited. In fact, production is nowadays achieved through massive drilling and the simultaneous stimulation of the reservoir. As a result, current technology focuses primarily on the recovery of free gas from hydraulic fractures, while the adsorbed gas that is

retained in the matrix of the rock is left behind (NSF, 2012). As discussed below, the latter is thought to account for up to 50-80% of total resources (Montgomery et al., 2005, Lane et al., 1991; Curtis, 2002), thus dramatically affecting the efficiency of the recovery operation. In this context, a better understanding of the mechanisms of adsorption that control storage and gas release in these reservoirs is needed to fully disclose Gas-In-Place (GIP) and recoverable reserve. Additionally, while water is still predominantly used to fracture the rock, other fluids, such as supercritical CO₂ are being considered. Hereby, the relatively low viscosity of supercritical CO₂ leads to breakdown pressures that are considerably lower than those observed with water injection under the same in situ rock stress and flow rate (Ishida et al., 2012). Also in this case, the feasibility of CO₂ injection and storage in hydrocarbon shale reservoirs requires a thorough understanding of the rock behavior when exposed to CO₂, thus including its adsorption characteristics. Shale reservoirs are widely distributed in the US with existing infrastructures used for gas and oil production operation; should CO₂ injection in such reservoirs prove feasible, the capacity of geologic formations for CO₂ storage will increase significantly.

As anticipated above, one feature that distinguishes unconventional from conventional gas reservoirs is the manner in which the gas is stored. In conventional reservoirs, the recoverable gas exists as a compressed fluid in the pores and cracks of the reservoir rock; this is known also as free gas and its behavior can be described by an equation of state, such as the real gas law. On the other hand, unconventional reservoirs contain fine-grained sediment rocks, such as mudrocks or coals, have significantly lower permeability and their porosity is limited to the existing nanopores. These nanopores are associated to minerals, such as clays, and organic materials, and they can retain significant amount of gas in the form of a condensed fluid by physical adsorption (Ambrose et al., 2012). Mathematically, the volume of fluid stored in a shale reservoir can be estimated with a relationship of the following form:

$$GIP = \rho \left[\frac{\phi(1 - S_w)}{\rho_b} - \frac{n^a}{\rho^a} \right] + n^a \quad (1.1)$$

GIP is the total gas in place including both free gas volume and adsorbed gas volume, ρ is free gas phase density, ρ_b is bulk rock density, ρ^a is adsorbed gas phase density, ϕ total porosity fraction, S_w is the residual water saturation, and n^a is amount of adsorbed fluid. The first term on the right hand side of Equation 1.1 is the amount of free gas; note that it includes the effect of

pore space reduction due to gas adsorption (n^a/ρ^a). The second term accounts for the amount of adsorbed gas, which can be obtained through the measurement of an adsorption isotherm. Several comments are worth making with respect to this equation. First, the available experimental data set of adsorption isotherms on shale samples at representative conditions is rather scarce and, accordingly, GIP estimates are still uncertain. Secondly, despite its association with gas storage in shale reservoirs, current methodologies to estimate volume capacities are improperly accounting for gas adsorption. Common practices neglect the volume occupied by the adsorbed fluid, n^a/ρ^a , thus resulting in the overestimation of the pore volume available for free gas storage (Ambrose et al., 2012). Yet, when this volume is accounted for, assumptions are made regarding the value of the density of the adsorbed fluid, ρ^a ; the key of the problem is that at sub-critical conditions, the adsorption process is dictated by the vapor-liquid transition and the adsorbed fluid takes the density similar to the one of the saturated liquid. However, at reservoir conditions most gases are in the supercritical state: here, a phase transition is absent and accordingly the density of the adsorbed fluid is not known a priori. As discussed in Chapter 2, this value is often assumed and a variety of methods can be applied to this purpose, thus leading to as many different results.

1.1 Objectives

As described above, the adsorption mechanism is important in unconventional reservoirs since the adsorbed gas can take up a major fraction of the total gas in place (20-80%) (Lane et al., 1991; Curtis, 2002). In practice, the ability to produce the adsorbed gas is still limited and current technology focuses primarily on the free gas in the fractures. Therefore, a better understanding and quantification of adsorption/desorption in these reservoirs is required, in order to allow for a more efficient and sustainable uses of these resources. Additionally, the density of the adsorbed fluid is a key parameter for disclosing reliable estimates of gas reserves and storage capacities, but its estimation still represents a major challenge. Large discrepancies have been found between estimates from different measurement techniques using representative fluids such as CO₂ and CH₄ at supercritical conditions and the adsorbed density can range anywhere between the liquid and the solid state of the adsorbate (Pini, 2014). The main objectives of this Master's Thesis are as follows:

- 1) To understand the adsorption control mechanism of fluids in mudrocks (TOC, thermal maturity, clay content, etc.).

- 2) To create a library of adsorption data measured on shale samples at relevant conditions and to analyze these data through the concepts of excess adsorption; these will be used to provide estimates for the density of adsorbed gas.
- 3) To build an experimental apparatus to measure adsorption properties of supercritical fluids (such as CO₂ or CH₄) in microporous materials. The system shall hold pressures up to 1,800 psi and temperatures up to 70°C.
- 4) To measure adsorption isotherms on microporous samples at various temperatures and pressures.

1.2 Organization of Thesis

The remainder of this thesis is organized as follows:

Chapter 1 briefly introduces the importance of gas adsorption and gas storage capacity in unconventional reservoirs together with the objectives of the present Master Thesis. This chapter shows that the current methodology to estimate GIP may be inappropriate for unconventional plays, since it does not take into account for pore space reduction due to adsorbed gas at reservoir conditions, thus overestimate the total GIP.

Chapter 2 contains an in-depth literature review of gas adsorption in source rocks. First, this chapter gives a brief introduction of source rock, its unique characteristics and parameters that controls adsorption. It also addresses the complexity of measuring adsorbed gas density and how it may vary from play-to-play or even from well-to-well within the same reservoir. A methodology is presented to estimate the adsorbed gas density from measured adsorption isotherms.

Chapter 3 introduces a new methodology to estimate GIP and storage capacities. A comparison of GIP in term of free and total gas between the conventional method and the new method has been performed to understand the uncertainties in gas reserve and storage capacities estimates.

Chapter 4 first introduces the approach that has been used design the adsorption apparatus and to measure adsorption. The analysis of potential sources of uncertainty is carried out and the equations are presented to account for them. Results are presented of CO₂ adsorption on a benchmarking material (13X zeolite) at two temperatures (25°C and 35°C) and in the pressure range of 500psia.

Chapter 5 discusses the outcomes from the adsorption tests and provides a comparison with a selection of data from the literature. Suggestions for improving experiment practice are presented, thus including the extension to the measurement of adsorption in shale.

Chapter 6 summarizes this research study and presents future recommendations.

CHAPTER 2 LITERATURE REVIEW

2.1 Pore Structure of Shales

Mudrocks are characterized by a complex pore structure that reflects the inherent heterogeneity of natural materials. A thorough study carried out by Loucks and coworkers on reservoir samples from the Barnett Shale reports that porosity in these rocks is predominantly characterized by so-called intra-particle organic pores, i.e. pores with sizes ranging between 5-800 nm and that are located within the organic matter of the rock (Loucks et al., 2009). Figure 2.1 shows intra-particle organic nanopores and illustrates the variation of shapes present inside the organic matter. It should be noted that the minimum pore size reported in the study by Loucks and coworkers was defined by the resolution of the applied technique (analysis of SEM images) and that smaller pores could therefore also be present. With respect to the IUPAC definition, therefore, we anticipate that all sorts of nanopores can be present in mudrocks, thus including micro- (< 2 nm), meso- (2-50 nm) and macropores (> 50 nm). Most importantly, the density of these nanopores can be very high, with most of the grains containing hundreds of nanopores and porosities ranging from 6 up to 30% for entire grains (Loucks et al., 2009). This is an important observation for mainly two reasons. First, nanopores are directly associated with adsorption of gas, due to the strong interactions between fluid molecules and solid constituents in these highly confined environments. Second, the relatively large value of porosity suggests that adsorption can significantly contribute to gas storage in mudrocks, in addition to simple gas compression that is characteristic of conventional reservoirs.

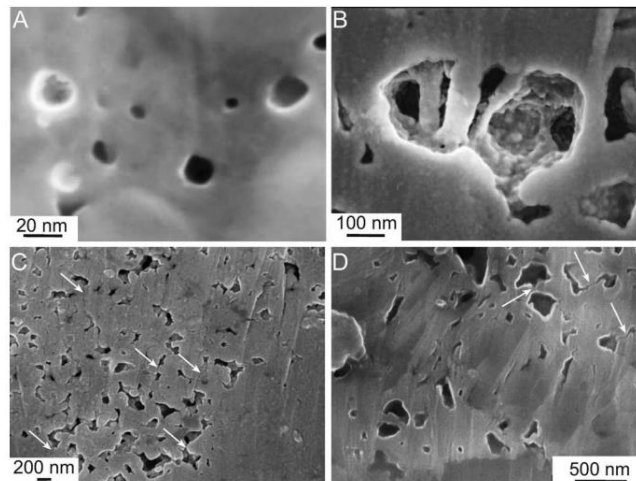


Figure 2.1: Images of the variegated population of pores the Barnett Shale sample. A) Spherical nanopores with diameter ranging from 18-46nm. B) Complex large pore structure (550 nm

diameter). C) and D) Tube-like and elliptical pores (20nm). Images taken from secondary electron (Loucks et al., 2009).

2.2 Concept of gas adsorption

In a shale gas system, gas is stored in two different states, namely free gas and adsorbed gas (Montgomery et al., 2005). This situation can be depicted as shown in Figure 2.2, where a schematic is shown of an idealized fractured shale sample. Free gas is present within the fracture as well as inside the large pores, which include both macro- and meso-pores. Additionally, adsorbed gas is present on the surface of these large pores and it completely fills the micropores. The latter contribute to the vast majority of adsorbed gas.

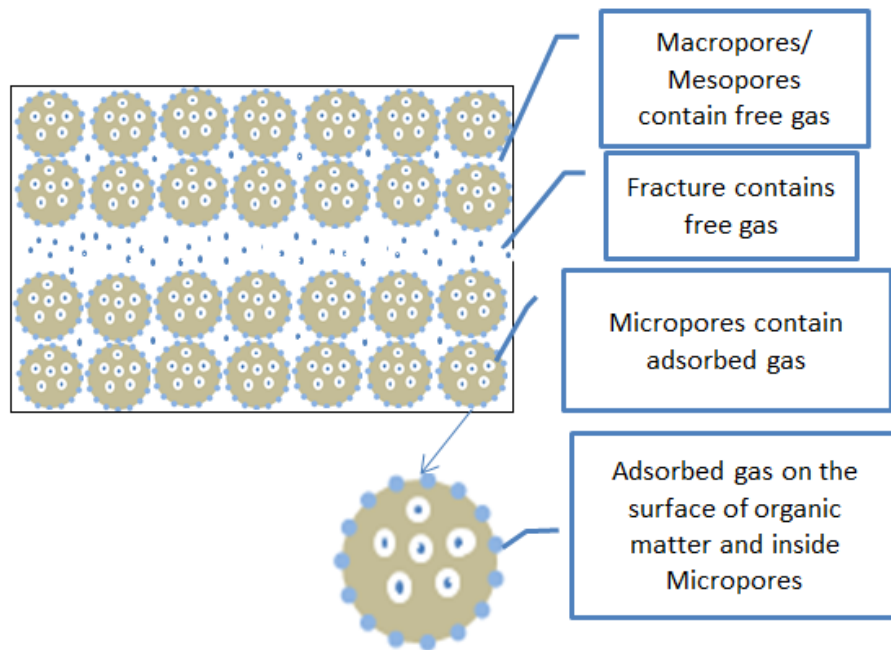


Figure 2.2: Gas adsorption behavior within shale sample.

From a physical standpoint, adsorption refers to the creation of a phase within the pores of the adsorbent material with a different (and significantly larger) density, as compared to the one of the homogeneous bulk fluid. In practical terms, adsorption can be seen as a condensation phenomenon of the gas within the pores of the material; as a matter of fact, conventional techniques to quantify porosity and pore size distributions exploit adsorption as a controlling mechanism (Kuila and Prasad, 2013). Hereby, experiments are conducted at low pressures (sub-atmospheric conditions) and the vapor-liquid equilibrium controls the process, thus ensuring that at saturation pressure the entire pore-space is filled with liquid adsorbate (Dubinin et al., 1960). The interest of gas adsorption at elevated pressures has recently gained momentum due to the

huge potential of natural gas production from unconventional reservoirs. High-pressure adsorption is synonymous of adsorption at above-critical (or super-critical) temperatures; hereby, a clear phase-transition is absent and accordingly the properties of the adsorbed fluid (density and volume) are not well defined. As a matter of fact, the measurement and the interpretation of the experimentally obtained adsorption data at these conditions still represent a technical and scientific challenge, and the actual mechanism of adsorption of a supercritical fluid is still far from being understood (Zhou et al., 2001).

Section 2.3 will discuss the adsorption isotherms of CH₄ and CO₂ on several shale samples around the world at different temperature reading and reservoir properties. These data are plotted as a function of pressure and they are reported in terms of excess adsorbed amounts. The latter is the truly measurable quantity in a high-pressure adsorption experiment and it is defined as the difference between the actual amount adsorbed, m^a , and the amount that would be present in the same volume at the density of the fluid in the bulk phase, ρV^a (Pini, 2014). The excess adsorption has been defined because we cannot know a priori the volume (and accordingly the density) of the adsorbed fluid. Mathematically, this measure is defined by Equation 2.1:

$$m^{excess} = m^a - \rho V^a \quad (2.1)$$

Where m^{excess} is the excess adsorbed amount, m^a is the actual amount adsorbed, ρ is the density in the bulk phase, and V^a is the adsorbed volume. From Equation 2.1, note that m^a and V^a can be written as $V^a \rho^a$ and m^a / ρ^a , respectively. Equation 2.1 can be further simplified in term adsorbed gas density and adsorbed amount and can be seen in Equation 2.2.

$$m^{excess} = m^a \left(1 - \frac{\rho}{\rho^a} \right) \quad (2.2)$$

The concept of excess adsorption is very important at high-pressure condition. It is also a useful tool to determine the adsorbed volume and adsorbed gas density without using any assumptions, thus reducing the uncertainty in the final results. The following section will demonstrate how Equation 2.2 can be used in Langmuir adsorption isotherm model to estimate excess adsorption. In Section 3.3.4 we will show the operating equations to obtain excess adsorbed amounts experimentally by using the manometric method to measure adsorption

isotherms. In addition, excess adsorption data have been reviewed and gathered from the literature on different shale plays can be seen in Section 2.3.

2.2.1 Adsorption isotherm models

Adsorption is highly controlled by the type of adsorbent material. There are many types of adsorption isotherm models that have been developed for microporous solids, such as coals and shale. Langmuir has developed one of the first methods of describing an adsorption isotherm. There are three main assumptions on his model; (1) the adsorbent material has a fixed number of adsorption sites; (2) these vacant adsorption sites have all the same size and are energetically equivalent; (3) each site can only contain one adsorbed molecule (monolayer) and there are no interactions between neighboring adsorbed molecules (Langmuir, 1918). The general form of Langmuir equation can be seen in the following.

$$m^a = \frac{q_{sc} b \rho}{1 + b \rho} \quad (2.3)$$

Where, m^a is the adsorbed amount at density ρ , q_{sc} is the saturation capacity from Langmuir model, b is Langmuir constant, which is a function of temperature. q_{sc} and b parameters can be obtained by fitting with the adsorption isotherm curve.

Note that Langmuir original equation is limited to low-pressure conditions. At higher pressures, it cannot capture the behavior of excess adsorption, which is the truly measurable quantity and that is characterized by a maximum (Section 2.2.2). The Langmuir equation can be modified to take into account for the volume and density of adsorbed phase using the concept of excess adsorption, i.e. Equation 2.4. The modified Langmuir equation can be seen in the following:

$$m^{excess} = \frac{q_{sc} b \rho}{1 + b \rho} \left(1 - \frac{\rho}{\rho^a} \right) \quad (2.4)$$

Here, m^{excess} is the excess adsorbed amount and ρ^a is the adsorbed gas density. In most case, ρ^a are normally assumed to be the liquid density; however, this assumption is not appropriate and will be discussed later in this thesis. The second term on the right hand side (RHS) of Equation 2.4 comes from the definition of excess adsorption as can be seen in Equation 2.2. In the next section, the concept of excess adsorption will be coupled with another method known as Graphical approach to estimate the adsorbed gas density.

2.2.2 Interpreting adsorption through a graphical approach

The interpretation of adsorption isotherms measured at elevated pressures requires a thorough understanding of the definition of excess adsorption, i.e. Equation 2.1. At relatively low pressures, the density of the bulk free phase is small and the term $V^a \rho$ becomes negligible; accordingly, $m^{excess} = m^a$. In other words, the behavior of the measured adsorption isotherms follows closely the one predicted by a Langmuir-like model. On the contrary, at high-pressures the term $V^a \rho$ becomes comparable to m^a and needs to be taken into account. This effect becomes particularly important when a fluid is used, whose critical temperature is close to the temperature at which the experiment is carried out. The manifestation of such situation is that the excess adsorption isotherm reaches a maximum followed by a decrease as the pressure increases. When the isotherm is plotted as a function of the fluid's bulk density this decrease has to become linear when m^a and V^a are constant, a condition that is met once adsorption saturation is reached. In other words, the volume occupied by the adsorbed fluid can be estimated from the slope of the linear descending portion of the isotherm and, accordingly, its density from the intersection of that line with the horizontal axis ($m^{excess} = 0$). This method will be applied on excess adsorption isotherms reported in literature for various shale samples. The result of adsorbed gas density for both CO₂ and CH₄ at different adsorbent material can be found in Table 2.1 (ie. page 12). Figure 2.3 illustrates an example how to estimate adsorbed gas density of CO₂ using graphical method in Permian Shale sample from Brazil.

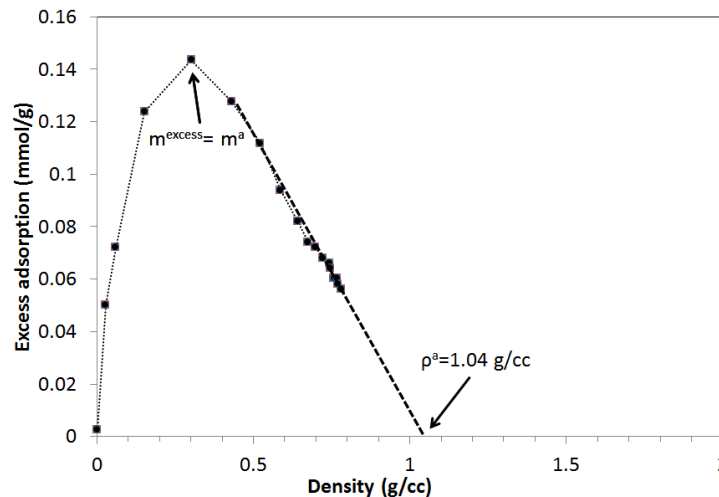


Figure 2.3: Excess adsorption isotherms of CO₂ as a function of bulk density measured at 45°C on Permian Shale sample from Brazil. The dashed line has been used to fit a straight line to determine adsorbed gas density. This technique is known as Graphical method. (Weniger et al., 2010).

The adsorbed phase density is a key parameter in the calculation of the total adsorption capacity of an adsorbent. As previously discussed, at high-pressure conditions, a phase transition of the fluid from gas to liquid is missing, thus resulting in many assumptions on the actual value of adsorbed gas density. Several assumptions have been made in literature to address the problem. A common assumption is that adsorbed phase fluid density is the same as the liquid density, meaning that there would be no excess adsorption once the fluid reaches saturation (Sircar et al., 1971). However, this assumption does not address the case of CO₂ after the saturation point, since there is still excess adsorption beyond the critical point (as it can be seen in Figure 2.3), indicating that the density of adsorbed CO₂ is greater than the liquid saturation density. Others assumed that the pore volume of the adsorbent material is equal to the adsorbed volume, since any molecule inside the pores is considered to be adsorbed (Wakasugi et al., 1981). Another method to estimate the adsorbed fluid density uses the close packing density of molecules at a fixed diameter (DeGance, 1992). An experimental study by Haydel and Kobayashi in 1967 shows that the adsorbed phase density for methane and propane on silicate gel is close to the inverse of the van der Waals volume of the adsorbate. Other approaches involve molecular simulations or the use of optical/imaging techniques. Another interesting and practical approach is given by the graphical interpretation of the measured excess adsorption isotherm. The results from this last approach are summarized in Table 2.1 together with a selection of results from the techniques listed above. There are several interesting points that can be taken from Table 2.1. First, adsorbed gas density values vary significantly among different adsorbents; when the so-called graphical interpretation approach is applied, estimates for CO₂ range around 1 g/cm³ for activated carbons and reach values as high as 1.75 g/cm³ for 13X zeolite, the latter being even larger than the solid density of CO₂ (1.6 g/cm³). These results raise some questions regarding the reliability of the measured adsorption data and/or the applicability of the estimation technique. Most importantly and with specific relevance to this study, large variations exist also when the same material is subject to similar pressure and temperature conditions, as it is the case for coals (0.93-1.49 g/cm³) and shales (0.79-1.08 g/cm³). Interestingly, similar outcomes are observed with CH₄ where adsorbed gas density varies significantly using the same experimental approach on various shale samples (0.2-0.78 g/cm³). The fact that in other cases discrepancies are observed when different techniques are applied on the same material suggests that some of the assumptions underlying these methods need to be

revisited. For instance, in most of these studies, the volume of adsorbent material is often required. The latter is typically estimated using helium gas, since the latter is assumed to be an inert gas and does not react with adsorbent materials. However, recent observations with 13X zeolite suggest that the adsorbent's volume can be overestimated when helium is used and that other methods should be applied (Pini 2014). It is one of the goals of this study to apply a similar procedure as described in Pini 2014 to shale samples.

Table 2.1: Density of adsorbed CH₄ and CO₂ using different approaches and adsorbent materials

Adsorbed Fluid	Reference	Adsorbent materials	Adsorbed Density (g/cm ³)	Range of CO ₂ /CH ₄ (g/cm ³)
CH ₄	Ambrose et al. (2012)	Graphite	0.34	0.2-0.78
	Haydel et al. (1967)	Silica Gel	0.37	
	Mavor et al. (2004)	Coal	0.42	
	Rolniak et al. (1980)	Zeolite 13X and 5A	0.16-0.32	
	Moffat et al. (1955)	Carbon Black	0.23	
	Gasparik et al. (2012)	Shale	0.2-0.64	
	Gasparik et al. (2013)		0.53	
	Gasparik et al. (2014)		0.42-0.78	
	Moghaddam et al. (2013)		0.19	
	Rexer et al. (2014)		0.76	
	Rexer et al. (2013)		0.26	
	Tan et al. (2014)		0.3-0.5	
Melnochenko et al. (2006)	Silica Aerogel		1.07	0.35-1.25
Di Giovanni et al. (2001)	Silica Gel	1.09		
Radlinski et al. (2009)	Coal	0.20-0.60		
Fitzgerald et al. (2005)		1.40		
Weniger. P et al. (2012)		0.93-1.49		
Steriotis el al. (2004)	Activated Carbon	0.52-0.59		
Humayun and Tomasko (2000)		1.01-1.04		
Sudibandriyo et al., 2003		0.99		
Van Hemert et al. (2009)		0.99		
Pini et al. (2006)		1.05		
Gensterblum et al. (2009)		0.95-1.01		
Weniger et al. (2010)		0.79-1.08		
Chareonsuppanimit et al. (2012)		Shale/Clay	1.25	
Busch et al. (2008)	0.84-1.2			
Jeon et al. (2014)	0.35-0.84			
Gao et al. (2004)	NAY Zeolite	0.8-1.3		
Hocker et al. (2003)	Zeolite 13X	1.59-1.75		
Pini (2014)		1.14-1.23		
Steriotis el al. (2002)	Carbon slit-pore	0.57-0.75		
Kurniawan et al. (2006)		0.88		
Liu and Welcox (2012)		0.81-0.90		

2.3 Current data set of adsorption on shale samples

The data set presented in the following has been gathered from published studies that report adsorption data on clay samples and mudrocks from various basins around the world. The latter include plays situated in North America (Barnett, New Albany, Muskwa, Duvernay, Montney), in Europe (Mesozoic, Paleozoic, Posidonia, Alum, Carboniferous), in South America (Irati, Rio Bonito, Ponta Grossa), and Asia (Longmaxi, Niutitang, Muderong). Most of the collected data refer to the adsorption of CH₄, because of the need to improve reserves estimates for gas plays. Few studies have included CO₂ adsorption (Weniger et al., 2010, Chareonsuppanimit et al., 2012, Busch et al., 2008, Jeon et al., 2014) due to a more recent interest on the sequestration potential in the same plays. Table 2.2 and Table 2.3 (ie. page 15) contain detailed rock properties information on each sample, including controls of adsorption, such as TOC, thermal maturity, and clay content. Table 2.2 provides CH₄ adsorption on source rock while Table 2.3 covers CO₂ adsorption on source and different type of clay minerals. Furthermore, the data set has been divided into five groups, namely CH₄ adsorption on North America shale plays (Figure 2.4, ie. page 16)), CH₄ adsorption on Europe shale reservoir (Figure 2.5, ie. page 17), CH₄ adsorption on Asia shale plays (Figure 2.6, ie. page 18), CO₂ adsorption from North and South America shale plays (Figure 2.7, ie. page 19), and CO₂ adsorption on pure clay minerals (Figure 2.8, ie. page 20). Excess adsorbed amount from these figures have been converted from mmol/g to SCF/ton. The standard temperature and standard pressure that was used are 59°F and 14.7 psi. The conversion number from mmol/g to SCF/ton are 759.078. Derivation of this number can be seen in Appendix A.

As can be seen in Table 2.2 and Table 2.3 no two shale reservoir systems are exactly alike. The adsorbed CH₄ density from Table 2.2 is ranging from 0.19 to 0.88 g/cm³ while the adsorbed CO₂ density from Table 2.3 is ranging from 0.36 to 1.30 g/cm³. The sample properties, such as TOC, clay content, and thermal maturity, vary significant from basin to basin, even from well to well. For example, two shale samples from Gasparik et al. (2014), HAD-103 and HAD 119, are both from Posidonia formation in Europe. They have the same TOC content and thermal maturity, however, the total clay contents are significantly different from each other, 35.9% and 16.2%, respectively. On an interesting note, these two samples have the similar adsorbed CH₄ density (0.7 g/cm³), as obtained from graphical method described earlier.

Table 2.2: Adsorption data set from multiple unconventional plays around the world on CH₄

References	Location	Sample ID	Acronym	Formation	Geological Age	Sample type	Gases	P/T conditions	TOC	Maturity	Clay content			Adsorbed Gas Density (g/cm ³)
											Illite-Smectite	Kaolinite	Chlorite	
Beaton et al. (2010)	North America	8995	NA-1	Muskwa Shale	Frasnian	Shale	CH ₄	20 Mpa/70 C	0.92	n/a	n/a	n/a	0.402	
	North America	9261	NA-2	Duvernay Shale	Frasnian	Shale	CH ₄	27 Mpa/72 C	n/a				0.560	
	North America	9256	NA-3	Montney Shale	Lower Triassic	Shale	CH ₄	27 Mpa/85 C	n/a				0.560	
Gasparik et al. (2012)	Europe	Aalburg 1	E-1	Mesozoic Shale	Oxfordian	Shale	CH ₄	25 Mpa/65C	1.02	n/a	60.2	4.7	6.5	0.640
	Europe	Aalburg 2	E-2			Shale	CH ₄	25 Mpa/65C	5.04		52	5	2.3	0.500
	Europe	Sleen 1	E-3			Shale	CH ₄	25 Mpa/65C	0.82		53.8	9.6	0	0.530
	Europe	Geverik	E-4	Paleozoic Shale	Namurian	Shale	CH ₄	25 Mpa/65C	6.1		33.4	0	0	0.200
Gasparik et al., (2014)	Europe	HAD-103	E-5	Posidonia	Lower Toarcian	Shale	CH ₄	25 Mpa/65C	6.7	1.5	35.9			0.720
	Europe	HAD-119	E-6	Posidonia	Lower Toarcian	Shale	CH ₄	25 Mpa/65C	7.7	1.5	16.2			0.780
	Europe	WIC-149	E-7	Posidonia	Lower Toarcian	Shale	CH ₄	25 Mpa/65C	11.7	0.5	n/a			0.520
	Europe	S2-2	E-8	Alum	Upper Cambrian	Shale	CH ₄	25 Mpa/65C	7.5	2.4	60.7			0.760
	Europe	S1/23	E-9	Carboniferous	Mississippian	Shale	CH ₄	25 Mpa/65C	5.5	4.2	42.1			0.420
	North America	M1-576	NA-4	Barnett	Mississippian	Shale	CH ₄	25 Mpa/65C	4.5	1	43			0.680
	North America	R	NA-5	Barnett	Mississippian	Shale	CH ₄	25 Mpa/65C	4.1	0.7	n/a			0.880
Moghaddam et al. (2013)	Europe	n/a	E-10	Carboniferous	Mississippian	Shale	CH ₄	12Mpa/ 62 C	n/a	n/a	n/a			0.193
Rexer et al. (2014)	Europe	HAR7060	E-11	Posidonia	Lower Toarcian	Shale	CH ₄	14 Mpa/45 C	5.78		n/a	26.2	6.6	0
	Europe	HAR7090	E-12	Posidonia	Lower Toarcian	Shale	CH ₄	14 Mpa/45 C	7.41	23.9		3.9	0.7	0.760
Rexer et al. (2013)	Europe	#1	E-13	Alum Shale	Upper Cambrian	Shale	CH ₄	14 Mpa/45 C	6.35	1.6	29.9	0.7	4.2	0.260
Tan et al. (2014)	Asia	G009507	A-1	Longmaxi	Lower Silurian Shale	Shale	CH ₄	23 Mpa/46 C	3.34	2.5-3	21.08			0.300
	Asia	G009509	A-2	Longmaxi	Lower Silurian Shale	Shale	CH ₄	23 Mpa/46 C	1.68	2.5-3	28.88			0.380
	Asia	G011298	A-3	Longmaxi	Lower Silurian Shale	Shale	CH ₄	23 Mpa/46 C	4.15	2.5-3	8.53			0.500
	Asia	G011313-1	A-4	Niutitang	Lower Cambrian	Shale	CH ₄	23 Mpa/46 C	1.38	3-3.5	23.28			0.320
	Asia	G009521	A-5	Niutitang	Lower Cambrian	Shale	CH ₄	23 Mpa/46 C	2.85	3-3.5	19.81			0.480
	Asia	G009518	A-6	Niutitang	Lower Cambrian	Shale	CH ₄	23 Mpa/46 C	7.44	3-3.5	7.2			0.480
	Asia	G009517	A-7	Niutitang	Lower Cambrian	Shale	CH ₄	23 Mpa/46 C	6.02	3-3.5	5.97			0.380

Table 2.3: Adsorption data set from multiple unconventional plays around the world on CO₂

References	Location	Sample ID	Acronym	Formation	Geological Age	Sample type	Gases	P/T conditions	TOC	Maturity	Clay content			Adsorbed Gas	
											Illite-Smectite	Kaolinite	Chlorite	Density (g/cm ³)	
Weniger et al. (2010)	South America	08-154	SA-1	Irati	Permian	Shale	CO ₂	23 Mpa/45C	1.62	n/a	n/a		1.100		
	South America	08-168	SA-2	Irati	Permian	Shale	CO ₂	23 Mpa/45C	24.21						
	South America	08-170	SA-3	Irati	Permian	Shale	CO ₂	23 Mpa/45C	11.66						
	South America	07-114	SA-4	Rio Bonito	Permian	Shale	CO ₂	23 Mpa/45C	17.3	2.61			1.000		
	South America	07-117	SA-5	Rio Bonito	Permian	Shale	CO ₂	23 Mpa/45C	21.09	1.51			1.300		
	South America	07-166	SA-6	Rio Bonito	Permian	Shale	CO ₂	23 Mpa/45C	n/a	n/a			1.280		
	South America	07-181	SA-7	Rio Bonito	Permian	Shale	CO ₂	23 Mpa/45C	11.13	1.05			0.800		
	South America	08-100	SA-8	Ponta Grossa	Devonian	Shale	CO ₂	23 Mpa/45C	1.29	n/a			0.820		
	South America	08-101	SA-9	Ponta Grossa	Devonian	Shale	CO ₂	23 Mpa/45C	0.7				0.860		
Chareonsuppanimit et al. (2012)	North America	C-14907	NA-6	New Albany	Devonian	Shale	CO ₂	14 Mpa/55 C	5.54	n/a			1.250		
Busch et al. (2008)	Asia	n/a	A-8	Muderong	Cretaceous	Montmorillonite	CO ₂	15MPa/ 45 C	0.5	n/a	27	26	5	1.200	
	Asia	n/a	A-9	Muderong	Cretaceous	Illite	CO ₂	15MPa/ 45 C	0.5		n/a	n/a	n/a	n/a	0.970
	Asia	n/a	A-10	Muderong	Cretaceous	Kaolinite	CO ₂	15MPa/ 45 C	0.5						0.840
Jeon et al. (2014)	North America	n/a	NA-7	n/a	n/a	Montmorillonite	CO ₂	13MPa/45 C	n/a	n/a	n/a	n/a	n/a	0.938	
	North America	n/a	NA-8	n/a	n/a	Illite	CO ₂	13MPa/45 C	n/a					0.357	

In another study, Rexer et al. (2014) also performed high pressure CH₄ adsorption experiments on samples from the Posidonia formation. These samples, HAR 7060 and HAR 7090, were analyzed by X- Ray Diffraction and Eval Pyrolysis analysis to obtain mineral compositions and TOC content. While the clay and TOC content of HAR7060 and HAR7090 are relatively close (30% and 6%, respectively), the adsorbed CH₄ density of these two samples are significantly different from each other, namely 0.26 g/cm³ for HAR7060 and 0.76 g/cm³ for HAR7090. Deviation in adsorbed CO₂ density within the same formation can also be seen in the data reported by Weniger et al. (2010). In their study, three different shale samples from Irati formation were analyzed. The TOC content of each samples are 1.62%, 24.21% and 11.66%, respectively, while thermal maturity and clay content were not provided. Interestingly, the adsorbed CO₂ densities of three samples are the highest for the lowest TOC content and relatively the same for the other two, i.e. 1.1 g/ cm³ and 0.85 g/cm³, respectively.

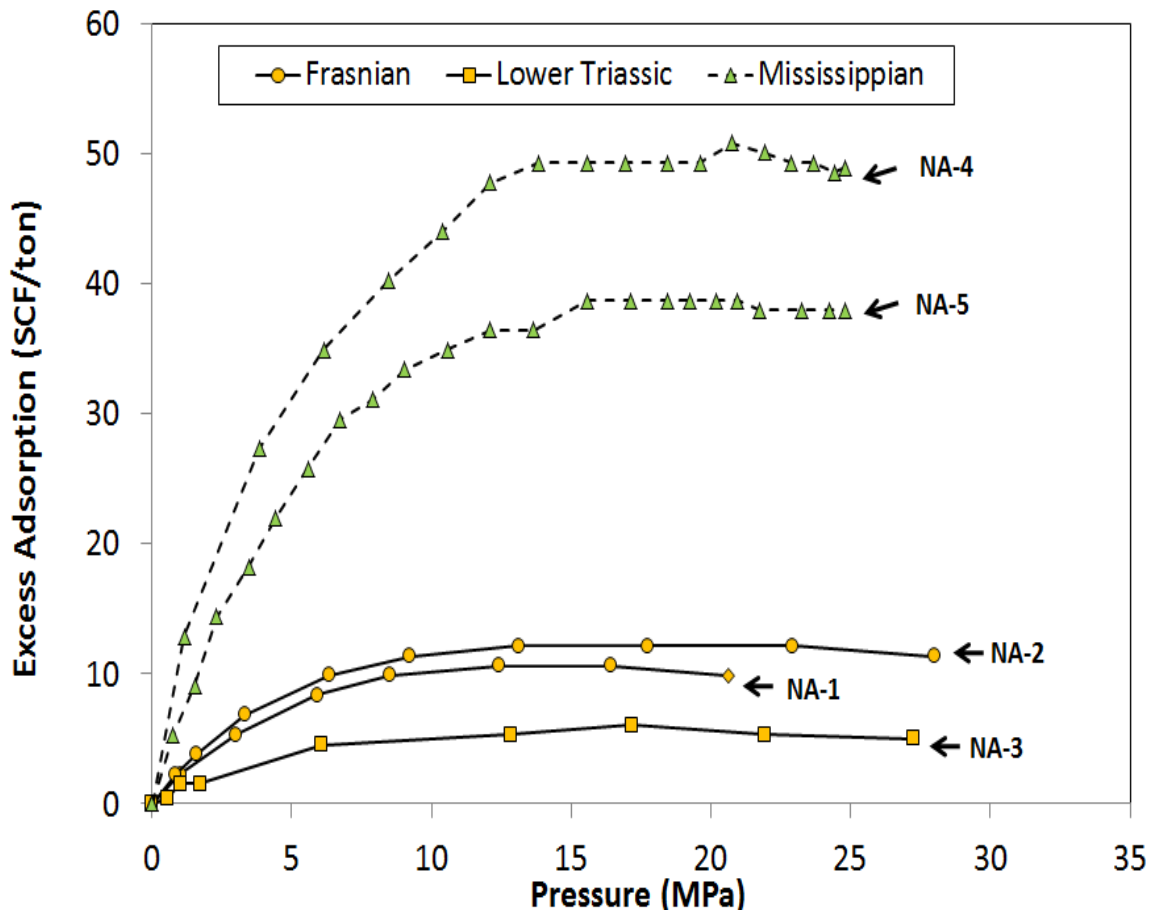


Figure 2.4: CH₄ adsorption on North America shale plays. References are provided in Table 2.2. Note that 1MPa is approximately 145 psi.

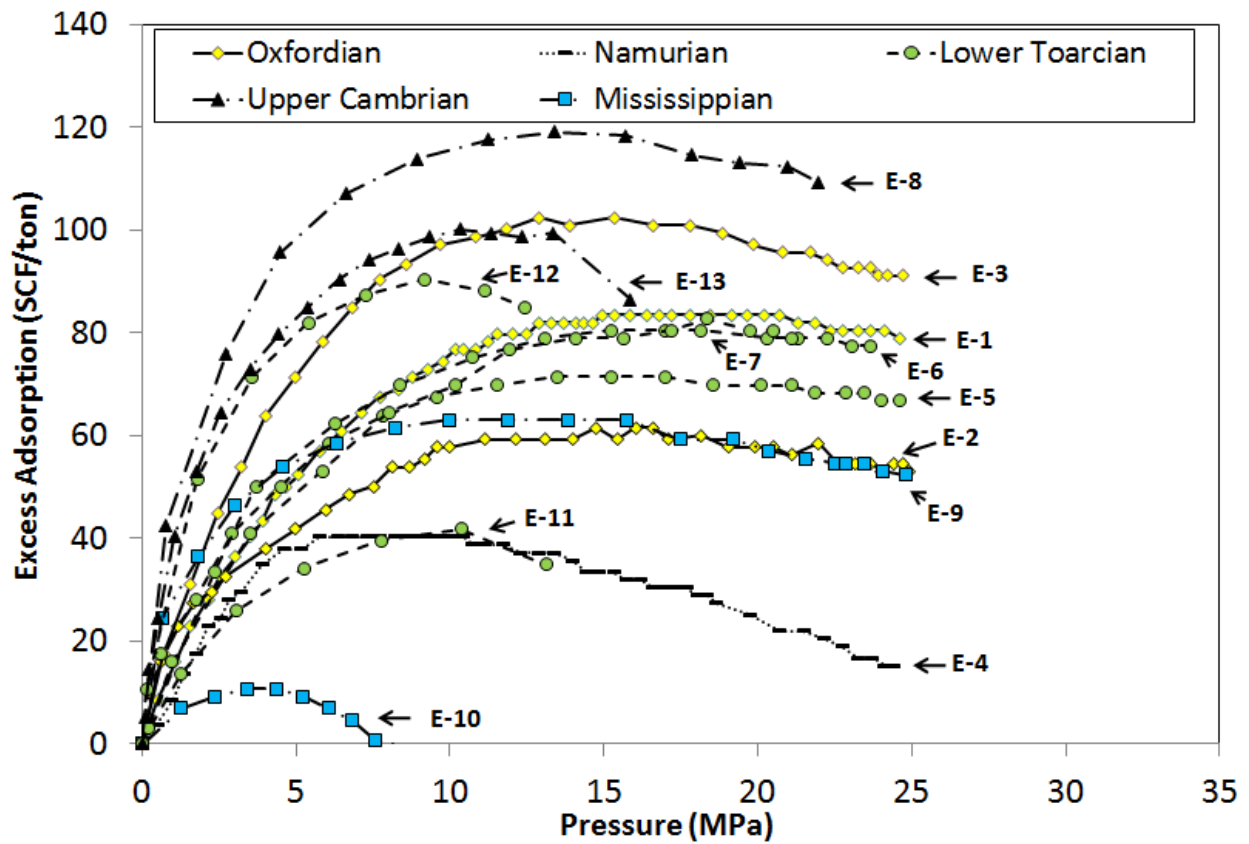


Figure 2.5: CH₄ adsorption from Europe shale reservoir. References are provided in Table 2.2. Note that 1MPa is approximately 145 psi.

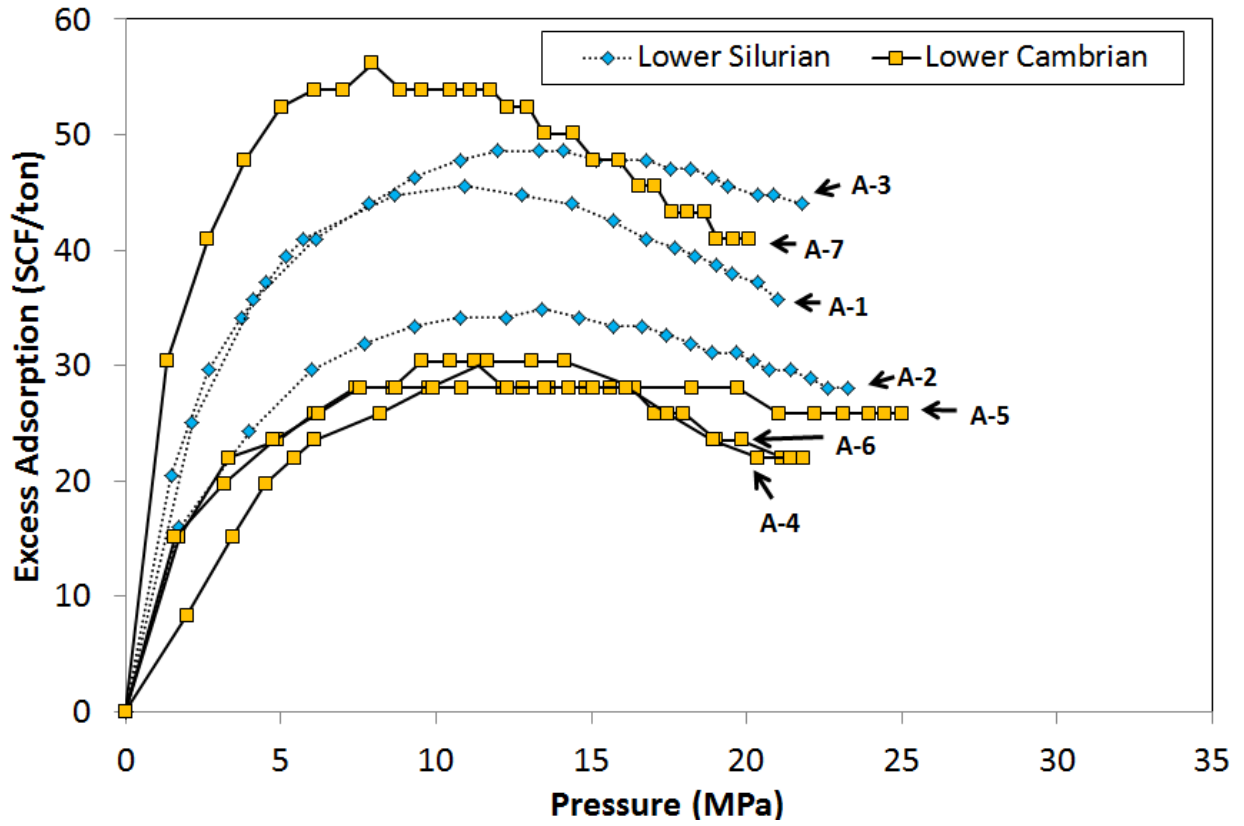


Figure 2.6: CH₄ adsorption from Asia shale reservoir. References are provided in Table 2.2. Note that 1MPa is approximately 145 psi.

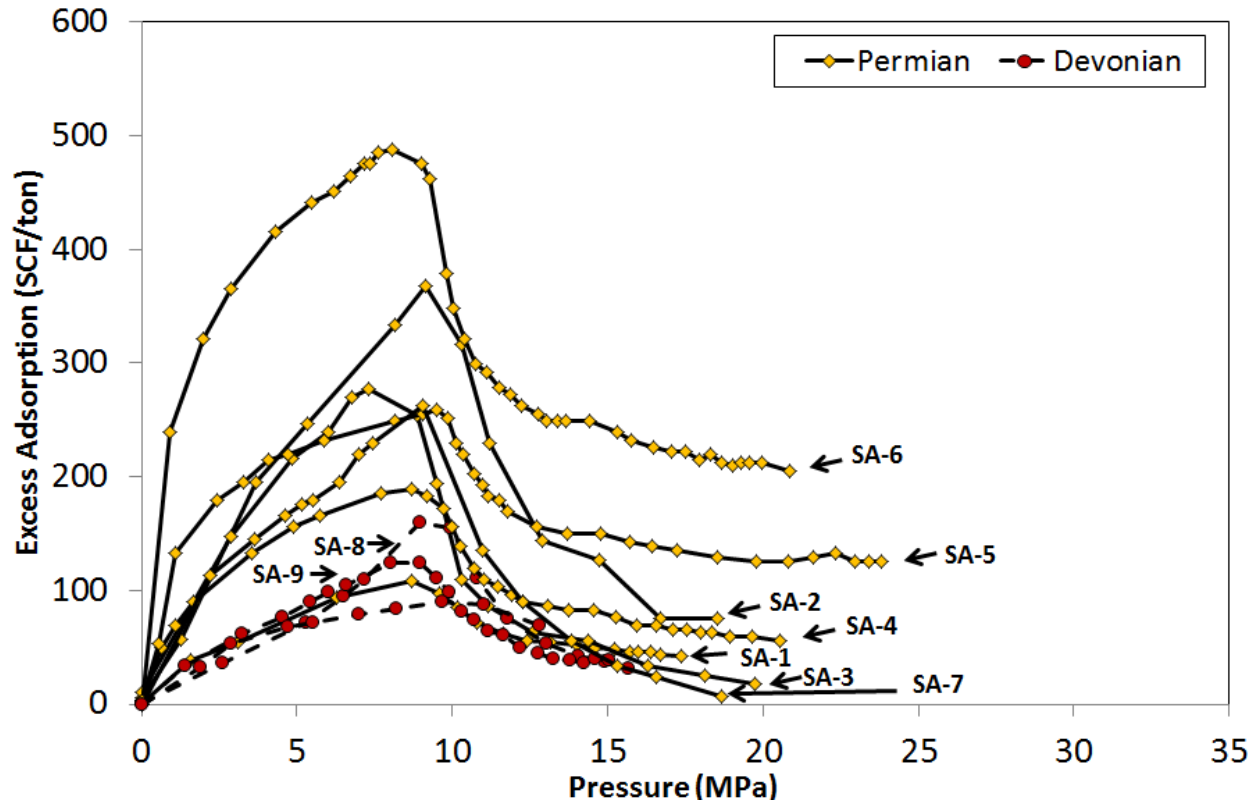


Figure 2.7: CO₂ adsorption from North and South America shale reservoir. References are provided in Table 2.3. Note that 1MPa is approximately 145 psi.

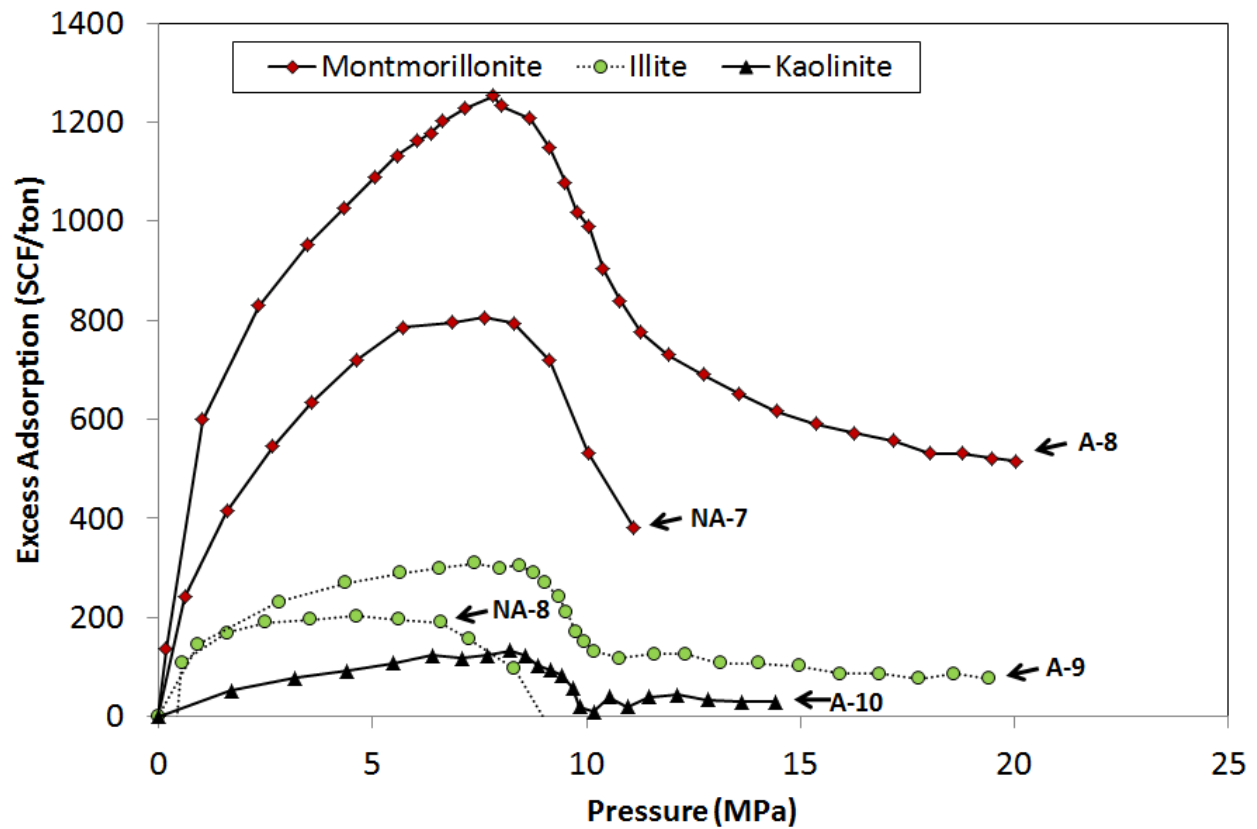


Figure 2.8: CO₂ adsorption from different type of clays. References are provided in Table 2.3. Note that 1MPa is approximately 145 psi.

Several interesting features can be observed from Figure 2.4 to 2.8. The excess adsorbed amounts for CO₂ and CH₄ are significantly different in different type of materials, thus confirming that the adsorption process depends on the type of adsorbate and on its specific interactions with the solid. For example, the excess adsorbed amount of CO₂ in shale reservoir reaches up to 450 SCF/ton, while for CH₄ excess adsorbed values reach a maximum of 120 SCF/ton. The excess adsorbed amount of CO₂ in clay material is much larger than for shale samples. In particular, adsorbed amounts in clay can reach up to 1,300 SCF/ton, i.e. almost three times the maximum value observed for shale samples. Moreover, out of the three different types of clays, montmorillonite (1,300 SCF/ton) adsorbs more than illite (300 SCF/ton) and more than kaolinite (100 SCF/ton).

In addition, the behavior of excess adsorption for CO₂ on both clays and shale samples shows a similar trend, as they both increase up to about 8 MPa followed by a steep nonlinear decline as can be seen in Figure 2.7 (ie. page 19) and Figure 2.8 (ie. page 20). As it can be seen in Figure 2.4 (ie. page 16) and Figure 2.6 (i.e. page 18), this trend does not appear in the case of CH₄ adsorption isotherms at the sample pressure condition for several reasons. The maximum increase in excess adsorbed amount is related to the rapid increase in the density of CO₂ in the corresponding pressure range. At the corresponding pressure, saturation of m^a and V^a are also reached, meaning that m^a and V^a will be relatively constant as pressure increases. Therefore, at this pressure the term ρV^a becomes suddenly very large. In the case of CH₄, the density is much smaller as compared to CO₂ at the same pressure and the term ρV^a is much smaller. Accordingly, the maximum increase in excess adsorbed amount of CH₄ is believed to occur at much higher pressure as can be seen in Figure 2.4, 2.5, and 2.6. From the previous figures, it can be observed that the maximum increase in excess CH₄ adsorption is ranging from 15 to 18 MPa. However, some of the adsorption isotherms show maximum peak in excess adsorption at much lower pressure. For example, one sample Mississippians shows a maximum increase in excess adsorption at 4 MPa. Other example from Frasnian formation in Figure 2.4 shows peak in excess adsorption at much higher pressure, approximately 22 MPa. The inconsistency in maximum excess adsorption in CH₄ could relate to multiple sources, such as error during measurements, assumptions used to determine adsorbent volume, or due to adsorption mechanism of the material itself. The latter will be addressed in the following section.

2.4 Controls on adsorption

The previous section has undoubtedly evidenced the variability of adsorption isotherm across different shale samples. Shales contain both organic- and inorganic matter and like any other natural material, are inherently complex. For instance, it was shown in Section 2.3 that excess adsorption values of CO₂ on pure clay minerals tend to be greater than those for shale materials; this observation in turn suggests that clays contribute significantly to the adsorption capacity of shales, while the presence of inert material in a reservoir shale sample reduces the amount of adsorbed gas per unit mass. In addition to clay content, other properties, such as total organic carbon (TOC), thermal maturity, moisture content, pressure and temperature conditions can potentially affect adsorption capacity. These controls are reviewed in the following and have been used in the literature to identify guidelines to evaluate shale samples. We anticipate that, although useful, these guidelines should be taken as approximations. As shown in Table 2.4 in most cases observations are in fact still contradictory with regards of whether a given property (such as the clay content or thermal maturity) has a positive or negative impact on adsorption. Accordingly, a definitive explanation regarding the actual mechanism of adsorption in shale samples is still missing and the actual contribution of mineral vs. organic matter not yet resolved. These observations highlight once more the complexity of gas adsorption on these unconventional reservoirs and the need for experimental data under different geological settings.

2.4.1 Total Organic Carbon (TOC)

Total organic carbon content represents the organic matter (OM) content of the petroleum system. TOC in a source rock has three basic components, hydrocarbon (i.e. OM transformed and retained as hydrocarbon), convertible carbon (OM that can be converted into hydrocarbons), and residual organic carbon (i.e. OM that will not produce hydrocarbon) (Jarvie et al., 2007). While TOC content is an important parameter in shale reservoir and can have significant effect on gas adsorption capacity, results are so far controversial. Some authors have presented a positive correlation between TOC on CH₄ adsorption capacity on shale samples from all around the world and have used this correlation to estimate gas in place (GIP) (Ross and Bustin, 2009, Weniger et al., 2010, Rexer et al., 2013, Zhang et al., 2012, Wang et al., 2013, Gasparik et al., 2014, Tan et al., 2014). Others have found no correlation between TOC content and adsorption capacity, as it is the case for dry shales from Paleozoic and Mesozoic shale from Netherlands with TOC ranging from 0.4% to 14.1% (Gasparik et al., 2012).

Table 2.4: A review on the effect of different properties of shale sample on excess adsorbed amount. The effects are shown with three abbreviations: N (negative), P (positive), n/a (Not available)

Reference	Gases	Sample Type	Method	TOC	Thermal Maturity	Clay Content	Moisture	Temperature	Pressure
Gasparik et al. (2012)	CH ₄	Shale	Manometric	N	N	P	n/a	n/a	P
Gasparik et al. (2013)	CH ₄	Shale	Manometric	n/a	n/a	n/a	N	P	P
Gasparik et al. (2014)	CH ₄	Shale	Manometric	P	P	N	N	N	P
Hu et al. (2015)	CH ₄	shale	Manometric	n/a	P	n/a	n/a	N	P
Moghaddam et al. (2013)	CH ₄	Shale	Manometric	n/a	n/a	n/a	n/a	N	P
Rexer et al. (2013)	CH ₄	Shale	Manometric	n/a	n/a	n/a	n/a	N	P
Rexer et al. (2014)	CH ₄	Shale	Manometric	P	P	P	n/a	N	P
Tan et al. (2014)	CH ₄	shale	Manometric	P	P	N	n/a	n/a	P
Weniger et al. (2010)	CO ₂ /CH ₄	Shale	Manometric	P	N	n/a	N	n/a	P
Chareonsuppanimit et al. (2012)	CH ₄ /CO ₂	Shale	Volumetric	n/a	n/a	n/a	n/a	n/a	P
Guo et al. (2013)	CH ₄	Shale	Volumetric	n/a	n/a	n/a	n/a	N	P
Guo et al. (2014)	CH ₄	Shale	Volumetric	N	P	P	n/a	n/a	P
Wang et al. (2013)	CH ₄	Shale	Volumetric	P	n/a	N	n/a	n/a	P
Zhang et al. (2012)	CH ₄	Shale	Volumetric	P	P	n/a	n/a	N	P
Ji (2012)	CH ₄	Clay	Volumetric	n/a	n/a	P	n/a	N	P
Lui et al. (2013)	CH ₄	Clay	Volumetric	n/a	n/a	P	N	N	P
Busch et al. (2008)	CO ₂	Clay	Manometric	n/a	n/a	P	P	n/a	P

In the latter case, the argument was brought that TOC is not the sole indicator, but the type of organic matter is also controlling adsorption capacity.

Organic matter is indeed further divided into an insoluble (kerogen) and a soluble (bitumen) component. The sum total of the bitumen and kerogen is called TOC. The major constituents of kerogen are carbon, hydrogen, and oxygen; Kerogen breaks down into hydrocarbon molecules when exposed to elevated temperatures and pressures over a long period of time. There are three types of kerogen, which are classified based on their respective compositions and evolution paths in a van Krevelen diagram (Levine, 1987). In particular, the hydrogen-carbon (H/C) ratio decreases from Type I- to Type III-kerogen, while the oxygen-carbon (O/C) ratio increases (McCarthy et al., 2011). One of the results of this evolution is that the relative amount of aromatic hydrocarbons as compare to aliphatic and naphthenic hydrocarbon increases. In this context, Zhang et al. (2012) suggests that adsorption increases when the kerogen contains a larger amount of higher aromatic structures; accordingly, Chalmers and Bustin (2008) concluded that gas adsorption decreases in the order Type III- > Type II- > Type I-kerogen.

Bitumen, as previous mentioned, is a soluble material. It tends to fill the pore throats and complicate the adsorption process in source rocks. Several studies have performed experiments to see how adsorption isotherm behaves before and after extracting bitumen. A study by Valenza and co-workers show that surface area of shale sample increases as bitumen extracted (Valenza et al., 2013). A more recent study by Gou and co-workers show that adsorbed CO₂ and CH₄ volume in bitumen attracted shales were much higher than for the unextracted shales (Guo et al., 2014). Despite the possibility of some gas dissolved in bitumen, the reduced surface area of the source rocks due to the presence of bitumen leads to a net decrease in gas adsorption (Ellis et al., 2014)

2.4.2 Thermal maturity

As described above, kerogen and bitumen generate petroleum in the form of oil and gas when exposed to elevated pressures and temperature for a sufficient amount of time. The degree to which this transformation has occurred is referred to as thermal maturity and is one of the most important parameters that are being used to assess the potential of shale plays and source rocks in general. There are three levels of maturity that are recognized by petroleum geochemists: early, peak, and late. Vitrinite reflectance (R_o) and Rock-Eval pyrolysis (T_{max}) are

methodologies applied to quantify the stage of thermal maturation. For the former, a R_o value of 0.5 or lower represents the early stage, where minimal amounts of hydrocarbons have been generated. Accordingly, a R_o value between 0.6 and 0.78 represents peak maturity, and a R_o value of 0.78 and above usually indicates late maturity.

Rock-Eval pyrolysis involves a temperature-programmed heating of a small amount of rock sample (100mg) in an inert-gas atmosphere (helium or nitrogen). This determines the quantity of free hydrocarbons present in the sample, known as the S1 peak. The pyrolysis oven temperature when determining S1 peak is at 300°C for several minutes. The amount of nonvolatile hydrocarbons and oxygen-containing compounds are also determined during the thermal cracking of the kerogen in the rock sample, which are known as the S2 and S3 peaks, respectively. Once S1 is determined, the oven temperature is programmed to increase at 25 °C per minute to a maximum temperature of 850°C. The temperature at which the maximum amount of S2 hydrocarbons is generated is known as Tmax. Tmax is a useful indicator of maturity, as the higher the value the more mature the source rock is (McCarthy et al., 2011). S3 maximum temperature corresponds to CO₂ that is released from thermal cracking of the kerogen during the pyrolysis experiment.

As it was the case for TOC, the debate is still open regarding the role of thermal maturity of shale on gas adsorption. Weniger and co-workers (Weniger et al., 2010) and Gasparik and co-workers (Gasparik et al., 2012) suggest that adsorption is not associated with thermal maturity based on experimental observations. On the contrary, a study by Hu and co-workers propose that oil and gas generation cause structural changes of the solid, insoluble organic matter in terms of additional mesoporosity and, accordingly, surface area. These in turn translate into higher adsorption capacity. In agreement with these arguments, similar positive correlations between thermal maturity and adsorption capacity on shale have been reported in other studies (Tan et al., 2014, Rexer et al., 2014, Gasparik et al., 2014).

2.4.3 Clay Content

Beside organic matters clay minerals represent a major component of mudrocks. Major shale reservoirs, such as Haynesville, Eagle Ford, Barnett and Marcellus possess an average clay content of 27%, 8%, 45%, and 50%, respectively. Illite/smectite, kaolinite and chlorite represent some the major constituents of the clay fraction; accordingly, some studies have focused on the adsorption properties of pure clay minerals as a first step towards the evaluation of the potential

of shale reservoir. However, also in this case, it is not surprising that the scientific community is not in complete agreement with regards to the role of clay content on gas adsorption. On the one hand, due to their high internal surface area and micropore volume clay minerals can significantly contribute to gas adsorption in clay-rich shales reservoir. Following these arguments, several studies report a positive correlation between adsorption capacity and clay content (Gasparik et al., 2012, Rexer et al., 2013, Ji et al., 2012, Busch et al., 2008, Liu et al., 2013), with the exception of the studies by Wang et al. (2013), Gasparik et al. (2014) who report a decrease in gas adsorption with increasing clay content. When pure clays are considered adsorption capacities decreases in the order of montmorillonite > illite/smectite mixed > kaolinite > illite (Ji et al., 2012 and Liu et al., 2013). These studies propose that gas adsorption takes place on the external surface of illite and kaolinite, while adsorption takes place interlayer of montmorillonite and interface of the clay mineral. Generally, studies seem to agree on the fact that the contribution of clay minerals to gas adsorption is an order of magnitude less when compared to organic matter (Ji et al., 2012, Gasparik et al., 2014, Tan et al., 2014) and it becomes negligible in the presence of moisture because of the high affinity of water to clay surface that prevent the access of gas molecules to the adsorption sites (Ross and Bustin, 2009). Beside the negative effect of moisture on gas adsorption, swelling is another factor that contributes less gas adsorption. Swelling has been observed in coal material at relative high pressure. Swelling was increased linearly with the amount of CO₂ adsorbed (Kelemen et al., 2009 and van Bergen et al., 2009). A similar scenario has also occurred in shaly clay sample. Studies by Busch et al. (2008) have shown that specific surface area of a highly shale clay sample before and after the adsorption experiment has been changed. This change in specific surface area, however, only occurs at high pressure condition, thus could possible relate to the swelling effect in clay.

2.4.4 Moisture

Several studies from literature have shown that moisture content generally limits adsorption capacity in shale reservoirs (Gasparik et al., 2014, Weniger et al., 2010, Zhang et al., 2012, Gasparik et al., 2013, and Liu et al., 2013). In fact, moisture occupies surface sites of clay minerals, causing these particles to swell and block pore throats, which would eventually reduce porosity, permeability and restrict access to adsorption sites. It has also been shown that the decrease in adsorption with moisture is limited by a critical value of the moisture content beyond

which no effects are seen. Interestingly, moisture content has a different effect on gas adsorption depending on the type of gases adsorbate. Day et al. (2008) argues that at the same moisture content, CO₂ would have more adsorption capacity than CH₄ because CO₂ has smaller kinetic diameter compared to CH₄. The latter would allow CO₂ to enter some of inaccessible sites that CH₄ would not be able to get into.

2.4.5 Temperature and pressure

Together with pressure, temperature is a primary control of the physical state of shale gas. Gas adsorption is an exothermic process; thus, the adsorption capacity of organic rich shale decreases with increasing temperature (Gasparik et al., 2014, Meghaddam et al., 2013, Rexer et al., 2013, Rexer et al., 2013, Zhang et al., 2012, Ji et al., 2012, Gasparik et al., 2013, Gou 2013). Some studies show that the adsorption capacity decrease by a factor of approximately two when temperature is doubled (Marc et al., 2009). In other words, with constantly increasing stratigraphic temperature, the adsorption capacity of organic rich shale decreases constantly, and the ratio of free gas rises continuously. A study by Lu and coworkers (Lu et al., 1995) simulated the gas adsorption capacity of Antrim shale at different temperatures and found that it decreases gradually as temperature rises from 25 °C to 60 °C. Chalmers and Bustin in 2008 found that temperature and gas adsorption capacity exhibit a negative exponential relationship, with the latter decreasing rapidly with rising temperature. A report by Guo in 2013 shows that under the combined effect of temperature and pressure, the influence of pressure on gas adsorption capacity is greater than that of temperature in the low temperature and low-pressure section, while the opposite is true in the high-temperature and high-pressure zone.

Pressure is directly correlated with depth. In general, the adsorption capacity of organic rich shale rises with increasing pressure. Specifically, the adsorption capacity increases rapidly at low pressure, and it gradually flattens with increasing pressures, eventually reaching a plateau. This is also the typical behavior predicted by a Langmuir-like adsorption curve. Note that when the experimental results are plotted as excess adsorbed amounts (Section 2.2 and 2.3), the isotherm is characterized by a maximum; the latter doesn't imply that beyond it, adsorption decreases, but it reflects simply the increase in adsorption (m^a) is smaller than the corresponding increase in the buoyant term (ρV^a).

CHAPTER 3

USING ADSORPTION DATA FOR GIP AND STORAGE ESTIMATES

The conventional GIP calculation consists of a volumetric component representing hydrocarbons stored in the pore space of the reservoir system as free gas. However, as mentioned above, this methodology is not applicable to an unconventional reservoir system, as gas is additionally adsorbed on the large internal surface area of the nanopores within the organic and inorganic components of shale. A second volumetric term is required to take into account for adsorbed gas. Ambrose et al. (2012) has regarded the volume occupied by the adsorbed phase into their GIP estimation calculation, as given by Equation 3.1.

$$G_{st} = \frac{32.0368}{B_g} \left[\frac{\phi(1 - S_w)}{\rho_b} - \frac{1.318 * 10^{-6} \hat{M}}{\rho_a} \left(G_{sL} \frac{p}{p + p_L} \right) \right] + \left(G_{sL} \frac{p}{p + p_L} \right) \quad (3.1)$$

Where G_{st} is total gas storage capacity, B_g is gas formation volume factor, ϕ is total porosity fraction, S_w is water saturation, ρ_b is bulk rock density, ρ_a is adsorbed phase density, \hat{M} is apparent molecular weight, G_{sL} is the Langmuir storage capacity, p is reservoir pressure, p_L is Langmuir pressure. 32.0368 and $1.318E^{-6}$ are the conversion constants to convert the total GIP value into unit of SCF/ton at standard temperature and pressure. These numbers will be derived later in Appendix A. In this study, we use standard temperature of 59°F or 15°C and standard pressure of 14.7 psi or 1 atm.

By using Equation 3.1, Ambrose and coworkers in 2012 have shown that conventional methods directly applied to unconventional reservoirs neglect the volume occupied by the adsorbed phase, thus overestimating the pore volume available for free gas storage and, accordingly, the GIP. More realistic estimates can be 10-25% lower than estimates with the conventional approach. In the following, we are arguing that the current uncertainty in adsorbed density values further increases this discrepancy. Note that there are many similarities between Equation 1.1 (based on our analysis) and Equation 3.1 (based on Ambrose's analysis). Both of these equations properly account for the volume occupied by the adsorbed gas in the free gas volume. If we generalize Equation 3.1 in terms of adsorbed gas density (ρ_a), free gas density (ρ), amount of adsorbed fluid (n^a), then Equation 3.1 becomes Equation 1.1. In Equation 3.1, reservoir parameters, such as formation volume factor, porosity, water saturation, bulk rock density and reservoir pressure can be obtained through field measurements. Langmuir storage

capacity, Langmuir pressure and adsorbed phase density can be estimated from laboratory studies using equilibrium adsorption isotherms. Ambrose and co-workers estimated the adsorbed density of methane by using molecular simulations and report a value of 0.34 g/cm^3 . However, as shown in Table 2.4 (i.e page 23), many other alternatives to estimate this value exist; in the following, we investigate the sensitivity of storage capacity estimates to the actual value of the adsorbed phase density, by considering both methane (CH_4) and carbon dioxide (CO_2). To this aim, representative parameters of a shale reservoir are used, as summarized in Table 3.1. Figure 3.1 shows the obtained methane GIP for three cases: (i) conventional approach than neglects the volume of the adsorbed phase (blue line), (ii) Ambrose’s approach that assumes an adsorbed density of 0.34 g/cm^3 (star symbol), and (iii) Ambrose’s approach by assuming any value of the adsorbed density between the critical and solid density of methane. In the latter case, we further distinguish between GIP based solely on free gas (red line) and total GIP (green line). Figure 3.2 (ie. page 31) shows the corresponding situation for CO_2 . As can be seen from these figures, the relative difference of estimated GIP by considering free and total amount of CH_4 can vary between 10-45% and 6-27%, respectively. In the case of CO_2 , discrepancies are even greater and range between 30-90% and 15-50%, respectively. There are several reasons to explain the significant differences between CO_2 and CH_4 . First, CO_2 has a much greater density when compared to CH_4 ; moreover, CO_2 has a much larger adsorption capacity than CH_4 in shale reservoir. Note that irrespectively of the fluid considered, there is a unique trend showing relative differences increasing with decreasing adsorbed density. It can be concluded that GIP estimates are very sensitive to the value of the adsorbed density; therefore, exact value of this parameter is required to avoid uncertainty in the final calculation.

Table 3.1: Shale and reservoir properties using to estimate GIP (CH_4) and gas storage capacity (CO_2).

Properties	CH_4 Values	CO_2 Values	unit
Porosity, ϕ	0.08	0.08	Fraction
Water Saturation, S_w	0.35	0.35	Fraction
Oil Saturation, S_o	0	0	Fraction
Bulk Rock Density, ρ_b	2.5	2.5	g/cm^3
Z factor	1	0.7	Fraction
Langmuir Pressure, P_L	1800	1800	psia
Gas Formation Volume Factor, B_g	0.0046	0.0031	rcf/scf
Molecular Weight, M	16	44	lb/lb-mol
Langmuir Storage Capacity, G_{sL}	120	240	scf/ton
Pressure, P	4000	4000	psia
Temperature, T	180	180	$^{\circ}\text{F}$

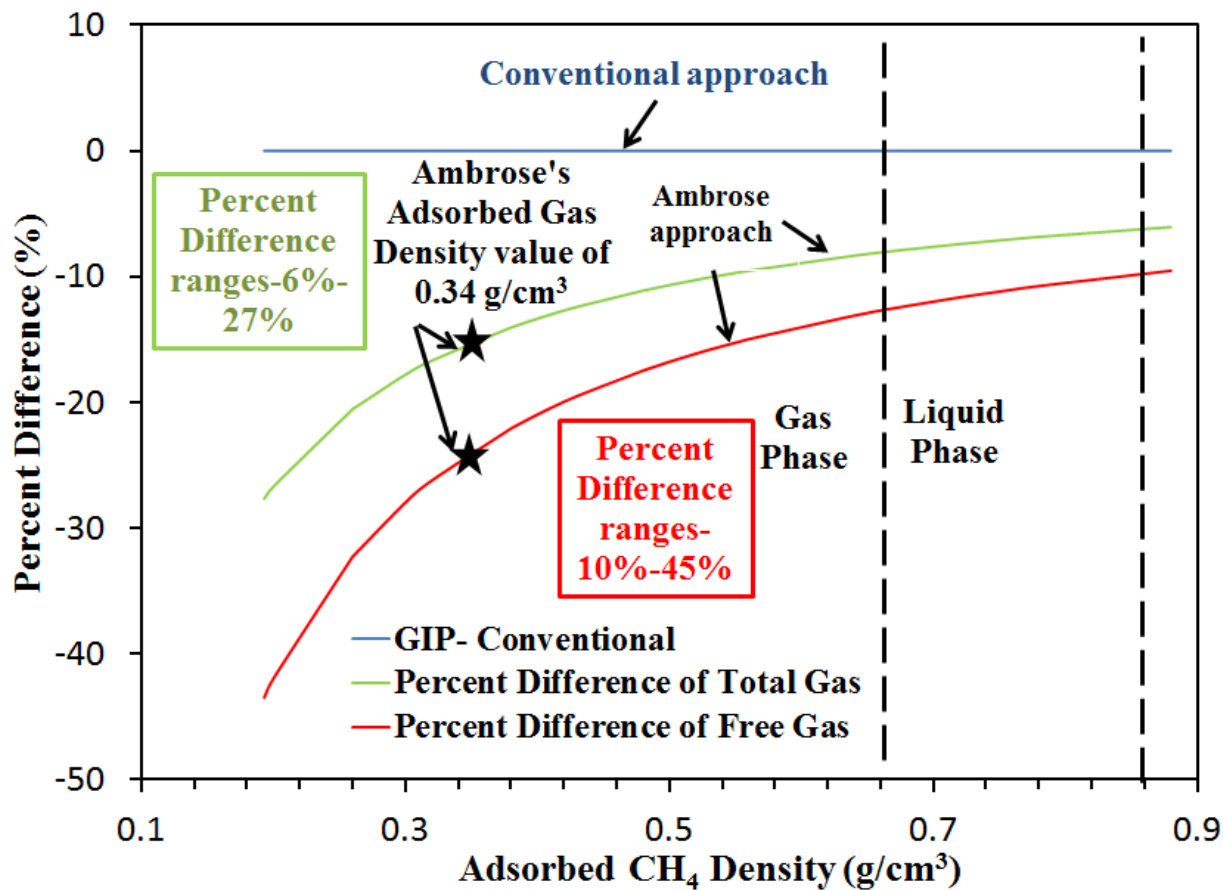


Figure 3.1: Percent difference between Ambrose method and conventional method for CH₄.

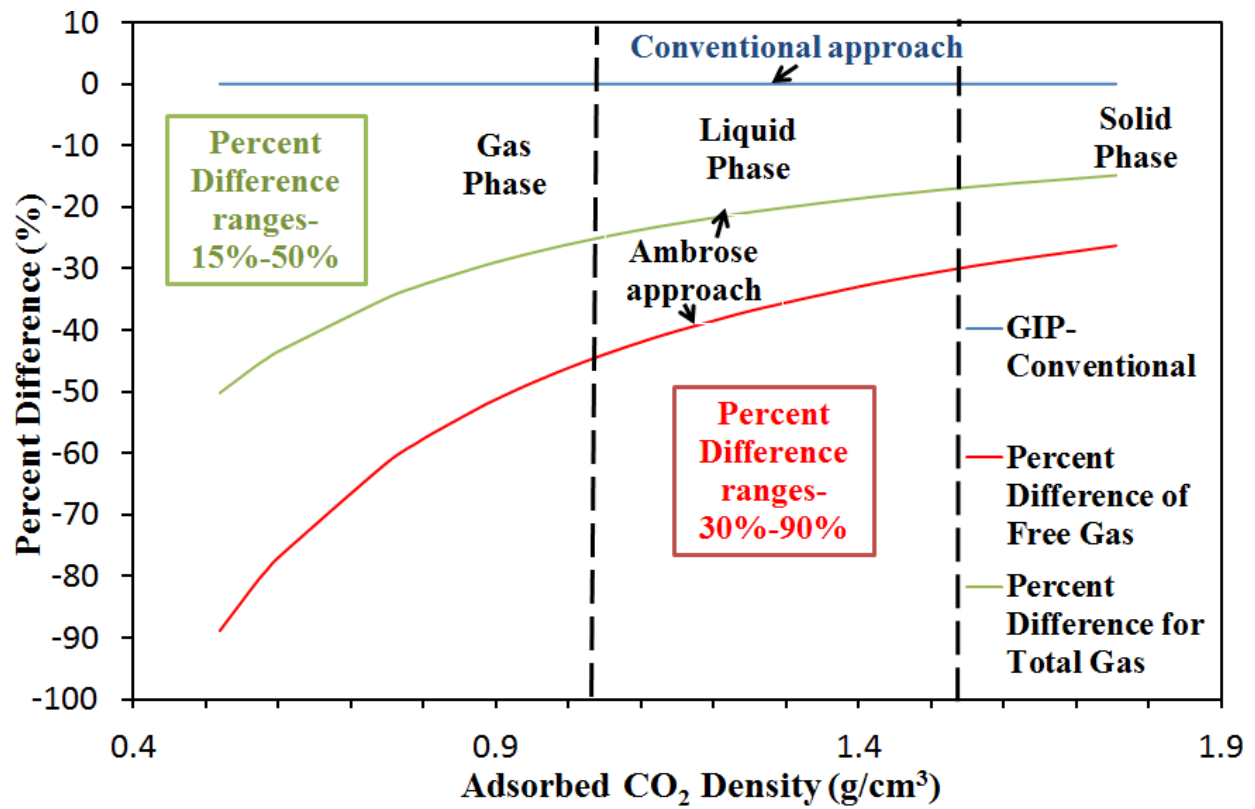


Figure 3.2: Percent difference between Ambrose method and conventional method for CO₂.

CHAPTER 4 DETERMINATION OF EXCESS ADSORPTION

4.1 Materials

Synthetic 13X zeolite in pellet form (Z10-03, Lotm 60009369.05, 1.6-2.5mm) from Zeochem AG (Uetikon am See, Switzerland) were selected in this study as a benchmarking adsorbent to design our system, mainly because adsorption isotherms on this material have been published in the literature (see Pini 2014, Cavenati et al., 2004, Hyun et al., 1982). 13X zeolite possess also a well-defined pore structure that allows for an interpretation of the adsorption isotherm that is more straightforward.

Helium (99.999% purity, from General Air service and supply) and CO₂ (99.999% purity, from General Air service and supply) gases were used to conduct the adsorption experiments. Due to its inertness towards most materials, helium is used to determine the skeletal volume of the sample material.

The sample is regenerated at a temperature of 215°C and under vacuum for 12 hours prior to each experiment. After the regeneration process, the sample is quickly weighted and placed inside the apparatus. Gas adsorption may occur during the previous step, thus possibly causing uncertainty in the final result. The manometric apparatus is therefore placed inside the oven to be dried at 215 °C and under vacuum for another 12 hours. Next, the entire system is allowed to cool down and is placed inside a water bath for the helium and CO₂ adsorption experiments. Note that the regeneration temperature for 13X zeolite performed in this study is below its requirement, which is approximately 550°C (Pini, 2014).

4.2 Experimental Methods

There are various experimental procedures for the determination of supercritical adsorption isotherms. The choice of each technique depends on the primary variable to be measured, namely pressure (manometric technique), weight (gravimetric technique), or gas flow (volumetric technique) (Santos, 2012). The manometric method is based on material balances and Boyle's law, and it will be used in this study. An extensive description of the principles of the manometric approach can be found in several papers published in literature; these include Mavor et al. (1990), Zhou et al. (2001), and Krooss et al. (2002). However, despite its simplicity, the manometric technique is prone to measurement errors, which may become even more significant when high-pressures conditions and weakly adsorbing materials are used. As

discussed in some recent studies, these problems can be effectively minimized when a careful design of the adsorption apparatus is carried out (Quinglin et al., 2003, Mohammad et al., 2009, Sircar et al., 2013). One of the key parameters that are used to reduce the error in a manometric system is to optimize the ratio between void volume and the dose cell volume. Gasparik and co-workers has stated in their studies that ratio volume of a manometric system should be in range of 2-6 (Gasparik et al., 2014). The ratio volume, 5.61, from literature will be implemented here in the apparatus design. In addition, virtual experiments have been carried out to see how uncertainties of pressure gauge affect the estimation of dose volume and uptake volume, as well as the excess adsorbed amount.

4.3 Manometric Method

The manometric method is based on the concept of mass conservation. The accuracy of excess adsorption values depends heavily on the accurate knowledge of system pressure, and temperature and void volume. Figure 4.1 illustrates a schematic diagram of the manometric apparatus used in this study. The latter consists of a dose cell (from Swagelok, withstanding pressures up to 1,800 psi), a sample cell (from Swagelok, withstanding pressures up to 1,800 psi), three high-pressure valves (from HIP), two 2 μ m filters (from Swagelok), and two pressure transducers (from APG digital pressure gauge, 3,000 psi with 0.25% accuracy). The 2- μ m filters are placed at the entrance and exit of the sample cell to prevent small particles from entering the valves. The entire system is placed inside a thermostat bath (from Thermo Fisher scientific) that can operate at temperatures up to 100°C with an accuracy of 0.1°C. Table 4.1 lists other equipment that was used for the adsorption experiment.

The dose volume consists of the space within the tubing between Valve 1 and Valve 2. The sample volume includes the sample cell, filters, and space between Valve 2 and Valve 3. The ratio between sample volume and dose volume in this system is about 6, as suggested from previous literature studies (Gasparik et al., 2014). The actual values of the dose and sample volume are selected based on virtual experiments, as explained in the next section.

Table 4.1: Equipment used for adsorption experiment

Quantity	Equipment	Manufacturer	Limitation	Accuracy (%)
2	Pressure gauge	APG digital pressure gauges	up to 3,000 psi	0.25
1	Thermo Bath	Thermo Fisher Scientific	up to 100 °C	0.1 ° K
2	Filter	Swagelok	2 μ m	-
5	Pressure valve	HIP	up to 15,000 psi	-
1	Vacuum pump	Milwaukee	under 10 psi	-

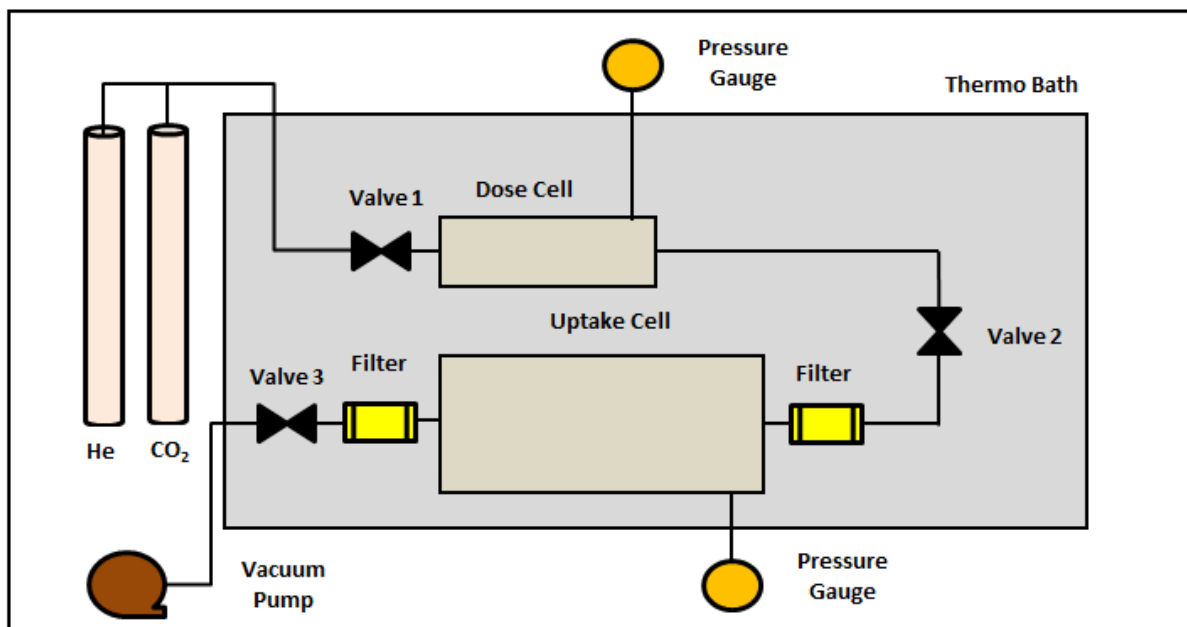


Figure 4.1: Schematic diagram of the manometric system

4.4 Virtual experiments

The goal of this section is to predict the uncertainties in measured quantities (dose and uptake volumes, adsorbent volume and adsorbed amount) based on the uncertainties of the pressure transducers. To this aim, a virtual experiment is performed that essentially solves a simple material balance, namely initial amount of gas in the system equal to final amount of gas in the system. The virtual experiment is carried out in the stages, namely (1) estimation of the empty volumes of the two reservoir cells, (2) estimation of the volume of the solid adsorbent, and (3) estimation of the adsorbed amount. While the uncertainty of 0.25% in the pressure gauge readings will affect each one of these three steps, the overall uncertainty in the measured property will increase from (1) to (3), due to error propagation. In the virtual experiment, accuracy of pressure gauge is assumed to be random within the range of 0.25% at each pressure step. The procedures of virtual experiment in determining system volume, adsorbent volume and excess adsorption isotherm uncertainties are explained in details in Appendix D.

4.4.1 System volume calibration using helium gas

The first step in designing the manometric system is to determine the size of the dose volume and uptake volume. Accordingly, the sum of these two volumes represents the system volume. There are three different options of volume system available in the design, which are

400 cm³, 150 cm³, and 82.2 cm³. In order to decide the size of the apparatus, three virtual experiments have been carried out. System volume that has the least uncertainty in dose volume and uptake volume would be selected since they will result the least uncertainty in excess adsorption result. Uncertainty in these volumes is estimated from statistical measures, such as the standard deviation. To this aim, a total of 200 virtual experiments have been carried out, so as to achieve a statistically significant sample population. The following equations have been used to perform virtual experiment in all three scenarios.

$$\frac{V_{SC}}{V_{DC}} = \frac{\rho_j - \rho_{DC,j}}{\rho_{j-1} - \rho_j} \quad (4.1)$$

$$V_{DC} = \frac{V_R (\rho_{j-1} - \rho_j)}{\rho_{DC,j} + \frac{V_{SC}}{V_{DC}} (\rho_{j-1} - \rho_j) - \rho_j} \quad (4.2)$$

Where V_R is the known amount of reference volume (stainless steel spherical balls), V_{sc} is uptake cell volume, V_{dc} is dose cell volume, $\rho_{DC,j}$ is the density in the dose cell at step j , ρ_j is the equilibrium density at step j , ρ_{j-1} is the equilibrium density at previous step. Derivation of these equations is shown in Appendix A. Equation 4.1 is obtained from helium gas expansion in an empty system to determine the volume ratio between uptake cell and dose cell volume. Equation 4.2 is also obtained using helium gas expansion; however, in this equation the uptake cell contains a known amount of reference volume. Note that the reference volume is different in all three cases, so as to maintain a constant system volume /reference volume ratio (arbitrarily set to 8 in this study). Accordingly, the reference volume values are 9.5 cm³, 17.2 cm³ and 45.9 cm³, for a system volume of 82.2 cm³, 150 cm³, and 400 cm³, respectively. Figure 4.2, Figure 4.3, and Figure 4.4 in the following pages show the standard deviation of dose volume at three different system volumes.

As expected, while the relative uncertainty remain constant among the three scenarios (about 2% error), the absolute uncertainty (standard deviation) decreases as system volume decreases. Note that these virtual experiments did not take into account of uncertainty in reference volume. As previously mentioned, reference volume used in this studies are stainless steel spherical balls. Each of these spherical balls possesses a volume uncertainty. As reference

volume increases in case of larger system volume, uncertainty in these systems also increase, thus resulting a negative impact on the overall calculation. Overall, it can be concluded that system volume of 82.2 cm^3 is the best option out of three possible choices. Using the system volume of 82.2 cm^3 , the dose cell volume and uptake cell volume are approximately 69.8 cm^3 and 12.4 cm^3 , respectively. According to virtual experiment, the standard deviations for dose and uptake volume are 0.2 cm^3 and 1 cm^3 , respectively. Using this information, uncertainties in adsorbent volume can be determined, as addressed in the following section.

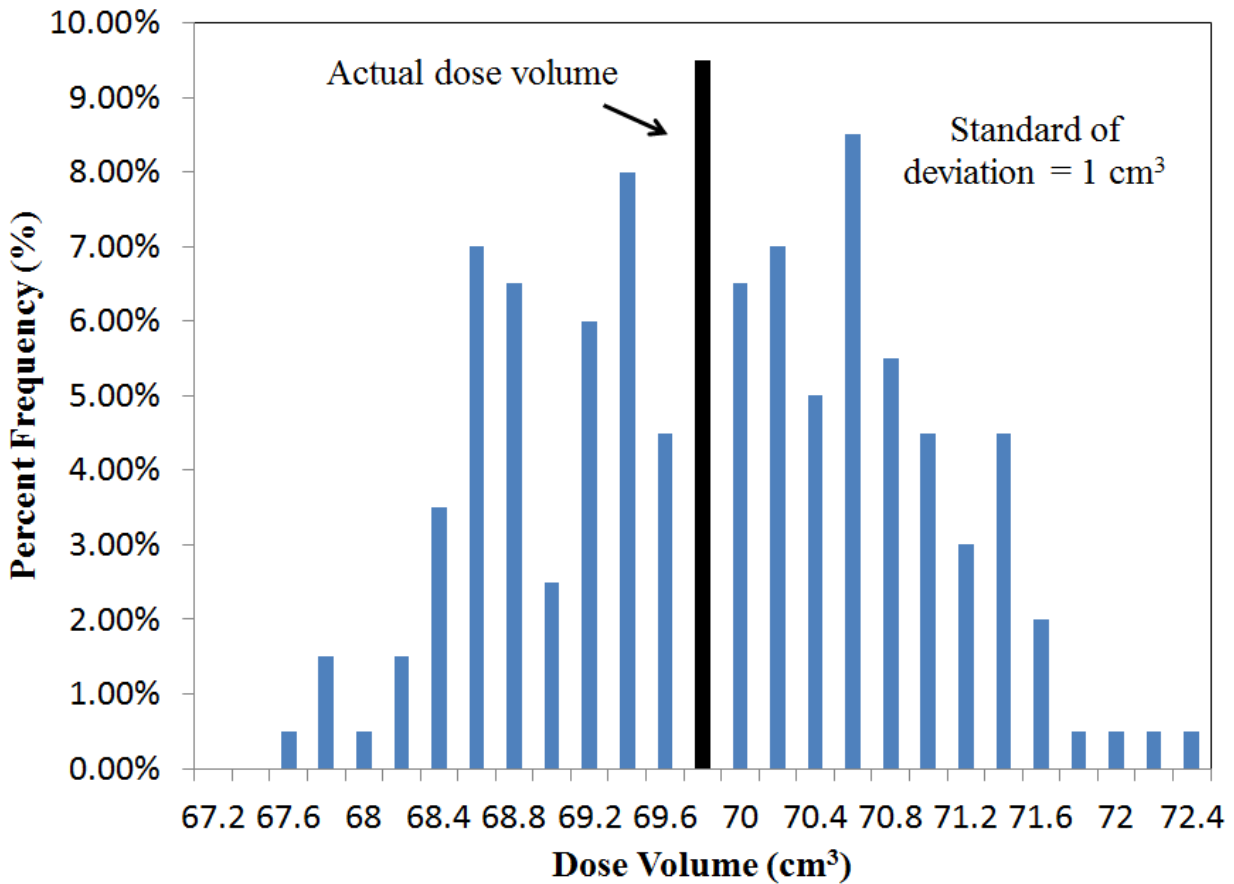


Figure 4.2: Figure illustrates the standard deviation of dose volume value if system volume is 82.2 cm^3 .

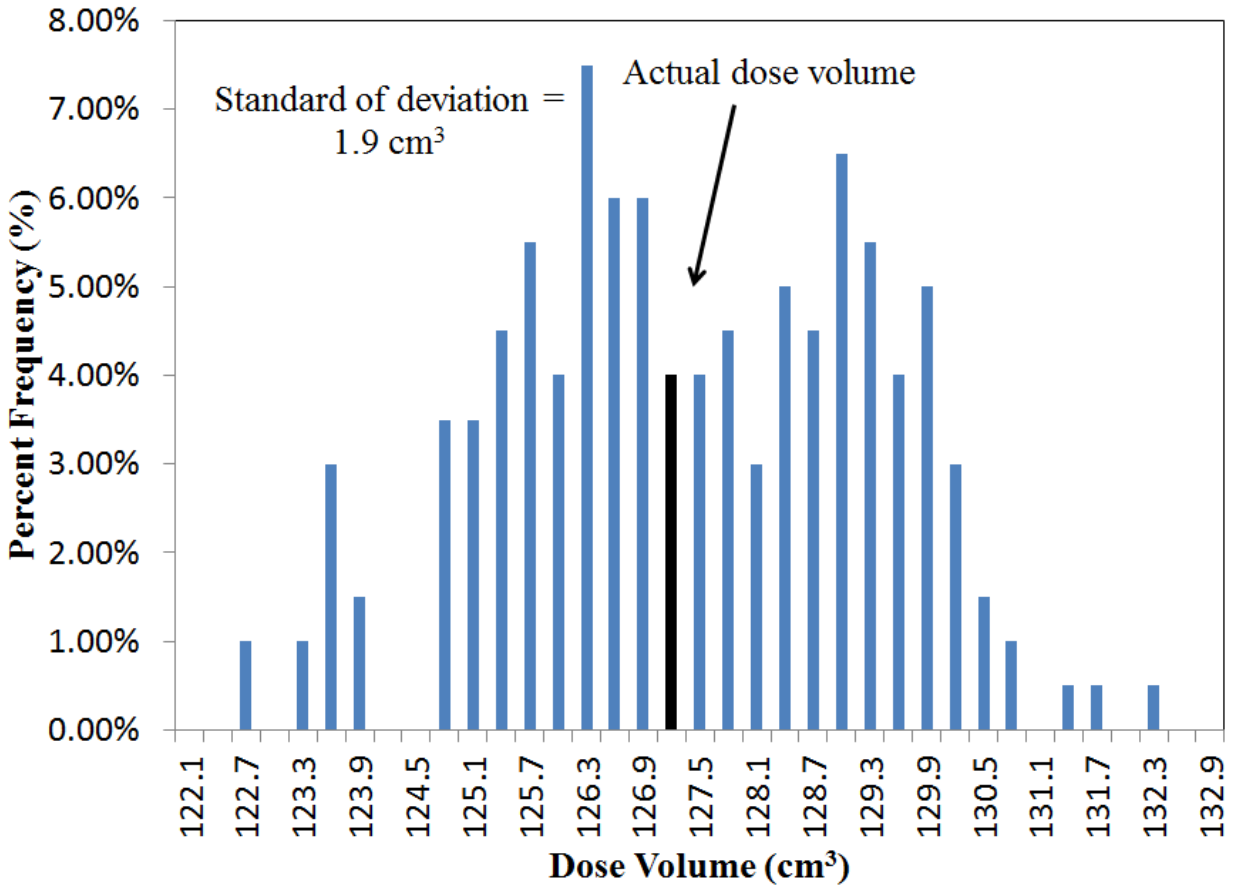


Figure 4.3: Figure illustrates the standard deviation of dose volume value if system volume is 150 cm³.

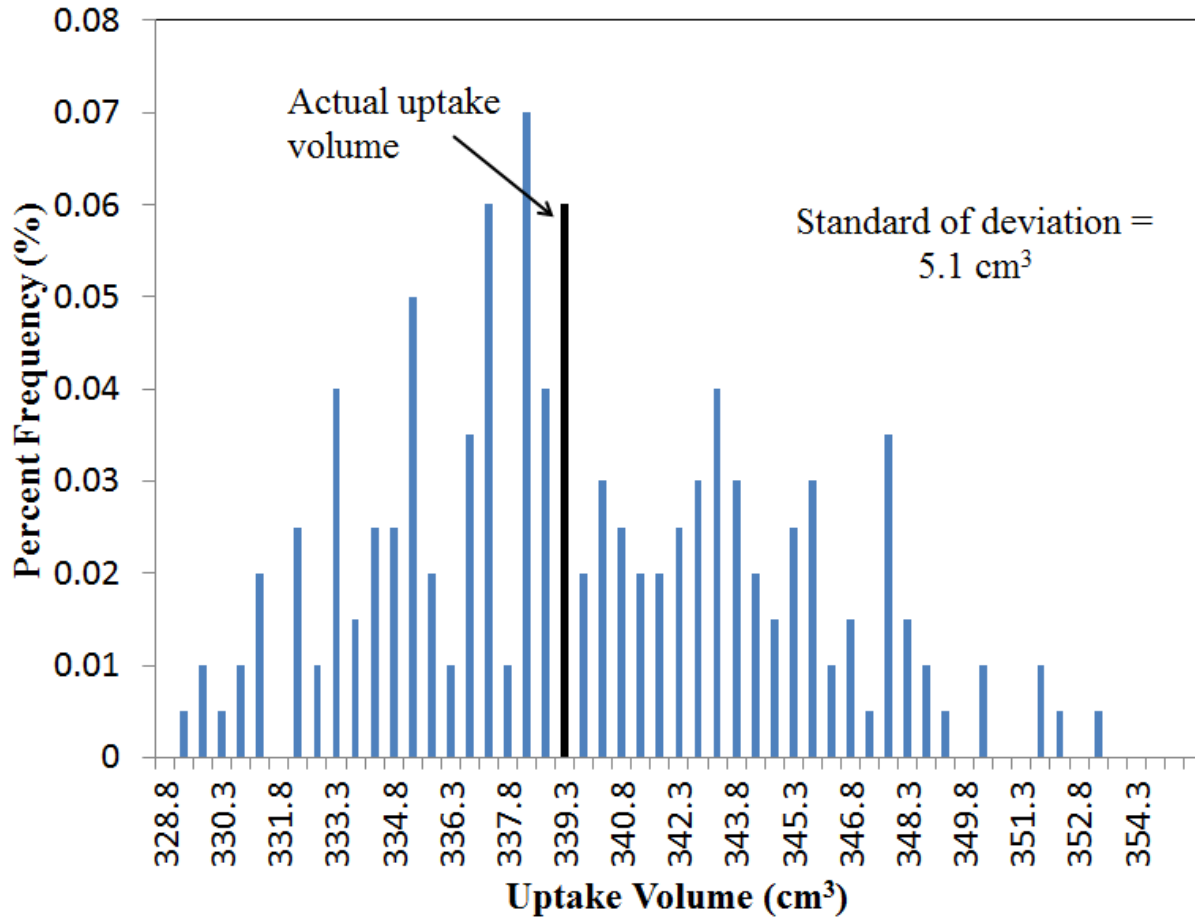


Figure 4.4: Figure illustrates the standard deviation of dose volume value if system volume is 400 cm^3 .

4.4.2 Adsorbent volume

Prior to the adsorption test, the skeletal volume of 13X zeolite materials is determined through helium experiment. The helium test is performed at the same conditions as the adsorption experiment. However, the use of helium for pore volume determination may be problematic (Pini, 2014). In this virtual experiment, helium is assumed to behave as a perfect inert gas, which contributes to no adsorption during the experiment. In addition, the uncertainties of adsorbent volume are mainly impacted by the uncertainty in dose volume and uptake volume. Accordingly, the maximum uncertainty of adsorbent volume based on the previous assumptions is 1.4 cm^3 using error analyses. Note that the uncertainties of adsorbent volume also depend on the total adsorbent amount. As the adsorbent amount increases, the uncertainty of dose and uptake volume decreases, thus reducing the uncertainty in adsorbent volume. The amount of adsorbent volume selected in this virtual experiment was 22.7 g or approximately 9.5 cm^3 . The latter is the adsorbent amount that will be used for the actual adsorption test (Section 4.5). The

error analyses equation that used to estimate uncertainty in adsorbent volume can be seen in Equation 4.3.

$$\sigma V_S = \sqrt{\frac{\sigma V_{DC}^2 (\rho_{DC,j} - \rho_j)^2}{(\rho_j - \rho_{j-1})^2} + \sigma V_{SC}^2} \quad (4.3)$$

Where σV_S is the uncertainty in adsorbent volume, σV_{DC} is the uncertainty in the dose volume, and σV_{SC} is the uncertainty in the sample volume. The derivation of the above equation will be included in the Appendix A. Table 4.2 shows the result of dose volume, uptake volume and adsorbent volume as well as their volume uncertainty using virtual experiment.

Table 4.2: Uncertainty results of dose volume, uptake volume, and adsorbent volume from Virtual experiment.

	Value (cm ³)	Uncertainty (cm ³)
Dose volume (cm ³)	12.4	0.2
Uptake volume (cm ³)	69.8	1.0
Adsorbent volume (cm ³)	9.5	1.4

4.4.3 CO₂ excess adsorption on 13 X zeolite at 25°C and 35°C up to 500 psi

Virtual experiments have been carried out to predict excess adsorption of 13X zeolite. The virtual test here incorporates the uncertainty in dose volume, uptake volume and adsorbent volume, as determined in Section 4.4.1 and 4.4.2, to predict the range of uncertainty in excess adsorption up to 500 psi. To this aim, adsorption data from the literature (Cavenati et al., 2004) has been input to the model, so as to predict the equilibrium fluid density in the system. The adsorption parameters were obtained from Cavenati's study and they were best fitted using Langmuir adsorption isotherm curves (Table 4.3). Using the information in Table 4.3, excess adsorption isotherms and the range of uncertainty at two experimental temperatures, namely 25°C and 35°C, can be estimated using error analysis from Equation 4.4. Derivation of this equation is included in Appendix A. Figure 4.5 shows the excess adsorption isotherms of 13X zeolite at 25°C and 35°C, up to pressure of 500 psi.

$$\sigma m_j^{excess} = \sqrt{(\sigma m_{j-1}^{excess})^2 + \frac{\sigma V_{DC}^2 (\rho_{DC,j} - \rho_j)^2 + (\sigma V_{SC}^2 + \sigma V_S^2) (\rho_j - \rho_{j-1})^2}{m_{AD}^2}} \quad (4.4)$$

Table 4.3: Inputs used to determine adsorption isotherm curve of 13X zeolite in virtual experiment at 25°C and 35°C.

	Temperature (°C)	
	25	35
Solid weight (g)	22.7	
Solid density, ρ_s (g/cm ³)	2.4	
Standard deviation in dose volume (cm ³)	0.2	
Standard deviation in uptake volume (cm ³)	1.0	
Standard deviation in adsorbent volume (cm ³)	1.4	
b (cm ³ /mmol)	24	23
Saturation capacity, qsc (mmol/cm ³)	18	16.5

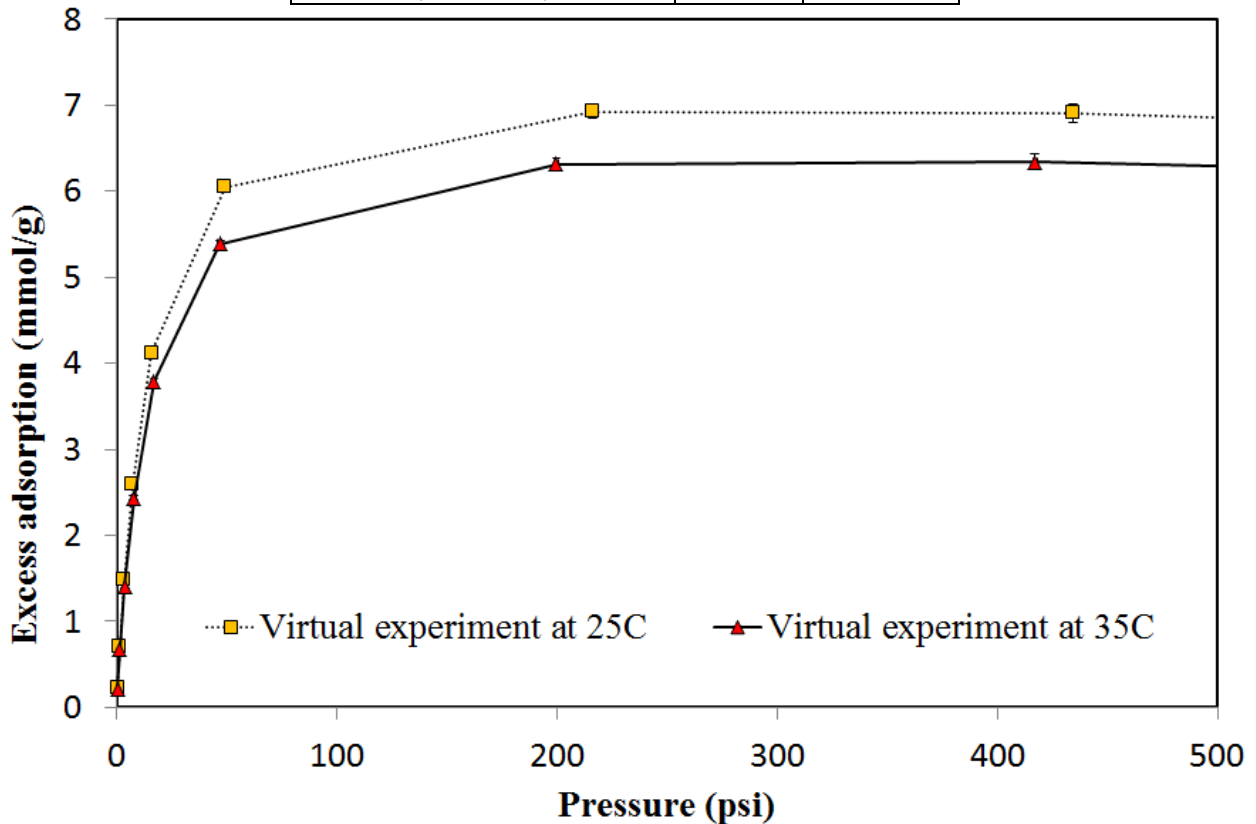


Figure 4.5: CO₂ excess adsorption isotherm at 25°C and 35°C as a function of equilibrium pressure. Note that the uncertainty of dose volume, uptake volume and adsorbent volume also included here in this plot. The relative error of excess adsorption at 500 psi for 25°C and 35°C are approximately 1.6%.

As can be seen from Figure 4.5, the uncertainties of excess adsorption capacity at 25°C and 35°C are relatively small, approximately 1.6%. Note that, the error in uncertainties calculation did not account for cumulative error in density, and only accounted for error in dose volume, uptake volume and adsorbent volume. In the following section, additional virtual experiments have been performed to quantify the uncertainties of excess adsorption at higher pressure.

4.4.4 CO₂ excess adsorption on 13X zeolite at 25°C and 35°C up to 1,600 psi

Virtual experiments have been carried out to predict excess adsorption of 13X zeolite at higher pressure. The virtual test here incorporates the uncertainty in dose volume, uptake volume and adsorbent volume, as determined in Section 4.4.1 and 4.4.2, to predict the range of uncertainty in excess adsorption up to 1,600 psi. To this aim, adsorption data from the literature (Cavenati et al., 2004) has been input to the model, so as to predict the equilibrium fluid density in the system. The adsorption parameters were obtained from Cavenati's study and they were best fitted using Langmuir adsorption isotherm curves (see Table 4.3). Figure 4.6 shows the excess adsorption isotherms of 13X zeolite at 25°C and 35°C, up to pressure of 1,600 psi.

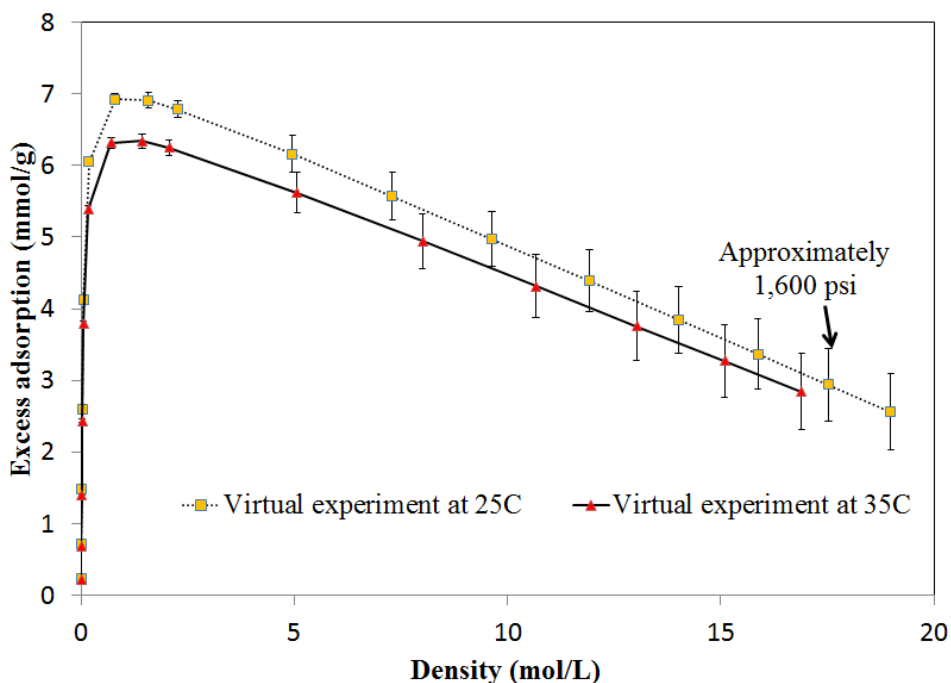


Figure 4.6: CO₂ excess adsorption isotherm at 25°C and 35°C as a function of equilibrium density. Note that the uncertainty of dose volume, uptake volume and adsorbent volume also included here in this plot. The relative error of excess adsorption at 1,600 psi for 25°C and 35°C are 19.9% and 18.6%, respectively.

As can be seen from Figure 4.6, the uncertainties of excess adsorption capacity at 25°C and 35°C in higher pressure are much greater, 19.9% and 18.6%, respectively. Note that, the error in uncertainties calculation did not account for cumulative error in density, and only accounted for error in dose volume, uptake volume and adsorbent volume.

4.5 Experimental tests

In this section, results from multiple experimental tests are described. Besides providing actual experimental data, these results can be compared to those from the virtual experiments, thus including measured uncertainties in system volume, adsorbent volume and excess adsorption isotherm.

4.5.1 System volume calibration using helium gas

As shown in the previous section, a system volume of 82.2cm³ is chosen for the experiments. The experiment is performed at the same condition as the virtual experiment (25°C, pressure range of 300 psi) and using helium gas. The procedure is as follows: helium gas is first injected into dose cell; once pressure has stabilized (typically after about 30 minutes), valve 2 is opened and gas is allowed to expand into sample cell. The pressure reading is recorded before and after expansion to determine the density in dose cell and equilibrium density in the system. The experiment is carried out at increasing pressures and results are summarized in Table 4.4 (volume ratio of dose and uptake cell) and Table 4.5 (dose and uptake volumes) for the different pressure step. Note that the uncertainty of dose volume and uptake volume is also included in

Table 4.4: Volume ratio between uptake volume and dose volume from helium gas expansion in empty system volume

Temperature (°C)	Dosing pressure, P _{dc} (psi)	Dosing density, ρ _{dc} (mol/L)	Equilibrium pressure, P _j (psi)	Equilibrium density, ρ _j (mol/L)	Volume ratio, V _{sc} /V _{dc} (cm ³)	Average volume ratio (cm ³)
25	84.2	0.234	12.8	0.036	5.563	5.609
25	183.7	0.508	38.5	0.107	5.620	
25	250.3	0.691	70.2	0.195	5.643	

Table 4.5: Value of dose volume and uptake volume from helium gas expansion at different pressure step and their standard deviation

Temperature (°C)	Dosing pressure, P _{dc} (psi)	Dosing density, ρ _{dc} (mol/L)	Equilibrium pressure, P _j (psi)	Equilibrium density, ρ _j (mol/L)	Reference Volume (cm ³)	Dose volume (cm ³)	Sample volume (cm ³)	Average dose volume (cm ³)	Average sample volume (cm ³)	Standard deviation in dose volume (cm ³)	Standard deviation in sample volume (cm ³)
25	100.6	0.279	17.2	0.0478	9.5	12.3	68.2	12.4	69.8	0.1	1.1
25	213.6	0.590	50.6	0.1405	9.5	12.5	70.4				
25	308	0.848	94.3	0.2615	9.5	12.5	70.7				

4.5.2 Adsorbent volume

Once dose volume and uptake volume are known, the adsorbent volumes (and its uncertainty) are determined using helium gas. The experiment is carried out similarly to the calibration experiment, though this time the uptake cell is filled with a given amount of adsorbing material. Equation 4.5 shows the material balance equation to determine 13X zeolite volumes.

$$\rho_{DC,J}V_{DC} + \rho_{J-1}(V_{SC} - V_S) = \rho_J(V_{DR} + V_{SC} - V_S) \quad (4.5)$$

Where $\rho_{DC,J}$ is the density in the dose cell at step j , ρ_J is the equilibrium density, V_{dc} is the volume of the dose cell, ρ_{J-1} is the equilibrium density in the system at the previous step. V_{sc} and V_s are uptake cell volume and adsorbent volume, respectively. We can arrange Equation 4.5 and solve for adsorbent volume, V_s . Using Equation 4.6, adsorbent volume can be determined at any pressure steps.

$$V_S = V_{SC} + \frac{V_{DC}(\rho_J - \rho_{DC,J})}{(\rho_J - \rho_{J-1})} \quad (4.6)$$

At each step, the uncertainty in the measured adsorbent volume is estimated from Equation 4.3. The adsorbent volume (and its uncertainty) used in the calculation of adsorbed amount are taken as the average from the three measurements. Table 4.6 shows the result of adsorbent volume at different pressure as well as their standard deviation.

Table 4.6: Results of 13X zeolite volumes from helium gas expansion.

Temperature (°C)	Dosing pressure, P_{dc} (psi)	Dosing density, ρ_{dc} (mol/L)	Equilibrium pressure, P_j (psi)	Equilibrium density, ρ_j (mol/L)	Zeolite Volume (cm^3)	Standard deviation of adsorbent volume (cc)	Standard deviation of adsorbent volume (cm^3)	Average Zeolite volume (cm^3)
25	109.6	0.30	18.7	0.05	8.9	1.3	1.3	9.5
25	197.6	0.55	49.6	0.14	9.7	1.3		
25	196	0.54	74.8	0.21	9.6	1.3		

It is worth noting that the uncertainties in dose volume, uptake volume, and adsorbent volume from experimental test reported in Table 4.5 and Table 4.6 are in close agreement with values estimated from the virtual experiments based on the uncertainty in the pressure readings (Table 4.2, ie. page 39). The uncertainties from virtual experiments are slightly greater than those obtained from experimental test because virtual test has been simulated up to 200 data points. At each of these points, a maximum uncertainty has been assumed. Experimental test, in contrast, only have 3 data points. It is believed that uncertainty in experimental test will increase if more tests are performed.

4.5.3. CO₂ excess adsorption on 13X zeolite at 25°C and 35°C

The measurement of an excess adsorption isotherm involves multiple pressure steps of gas expansion from a dosing cell into an uptake cell. Prior to the adsorption experiment, a procedure was carried out to ensure both dosing and uptake cell are clean and dry. This was done by drying the manometric apparatus and the zeolite material up to 215°C and under vacuum for 12 hours. Then, the manometric system is placed inside the temperature-controlled water bath and vacuum is applied for 1 hour prior to the adsorption measurement. The CO₂ adsorption test is started by filling the dose cell at a given pressure. Once equilibrium in the dose cell is reached (reached after about 1 hours), the valve connecting the dose- to the uptake-cell is opened to allow gas expanding into the uptake cell. System pressure and temperature are measured before and

after the gas expansion in order to determine gas density at that particular pressure step. The excess adsorbed gas amount can be computed subsequently. This procedure is then repeated in sequence by increasing the pressure at each step until reaching desired gas pressure. Using the database of the U.S. National Institute of Standards and Technology (NIST), the density of tested gas can be calculated at any given experimental temperature and pressure condition. Note that the equilibrium time at each expansion step is approximately 1 hour. The operating equation that is enabling to compute excess adsorbed amount from measured pressures is explained in the following. For the first pressure step, the following material balance Equation 4.7 is obtained.

$$n_1 = \frac{\rho_{DC,1}V_{DC} - \rho_j(V_{DC} + V_{SC} - V_S - V_1^a)}{m_{AD}} \quad (4.7)$$

Where n_1 is the adsorbed amount at Step 1 per unit mass adsorbent, $\rho_{DC,1}$ is the density inside dose cell before equilibrium for Step 1, V_{DC} is volume of dose cell, ρ_1 is the density at equilibrium inside the system for Step 1, V_{SC} is volume of uptake cell, V_S is volume of adsorbent, V_1^a is the amount adsorbed volume for Step 1, and m_{AD} is mass of adsorbent material. Accordingly, for Step 2, the following material balance, Equation 4.8, can be derived, where the amount of fluid already present in the sample cell is accounted for.

$$n_2 = \frac{V_{DC}[(\rho_{DC,2} - \rho_2) + (\rho_{DC,1} - \rho_1)] - \rho_2(V_{SC} - V_S - V_2^a)}{m_{AD}} \quad (4.8)$$

Equation 4.8 can be generalized for any j Step to provide the excess adsorbed amount. Excess adsorbed amount at any pressure step can be found using Equation 4.9.

$$m^{excess} = n_j m_{AD} - \rho_j V_j^a = V_{DC} \sum_{i=1}^j (\rho_{DC,i} - \rho_i) - \rho_j (V_{SC} - V_S) \quad (4.9)$$

All terms on the right-hand side of Equation 4.9 can be measured. Pressure inside the dose cell and equilibrium pressure are recorded, and an equation of state is applied to calculate the initial and equilibrium density. Parameters that were obtained from adsorption experiment on 13X zeolite at 25°C and 35°C can be seen from Table 4.7 and Table 4.8, respectively.

Table 4.7: Excess adsorption results at 25°C on 13X zeolite

Temperature (°C)	Dosing pressure, P_d (psi)	Dosing density, ρ_{dc} (mol/L)	Equilibrium pressure, P_j (psi)	Equilibrium density, ρ_j (mol/L)	Excess adsorption (mmol/g)	Cummulative error (%)	Percentage error (%)	Percentage error @500 psi (%)
25	400	1.31	0.1	0.000	0.717	0.01	1.6	2.6
25	588.7	2.17	1.2	0.003	1.890	0.02	1.2	
25	766.2	3.29	7.4	0.021	3.630	0.04	1.0	
25	748.2	3.15	51.6	0.146	4.937	0.05	0.9	
25	784.7	3.44	180	0.535	5.490	0.06	1.1	
25	1142.2	17.57	773	3.344	5.795	0.23	4.0	

Table 4. 8: Excess adsorption results at 35°C on 13X zeolite.

Temperature (°C)	Dosing pressure, P_d (psi)	Dosing density, ρ_{dc} (mol/L)	Equilibrium pressure, P_j (psi)	Equilibrium density, ρ_j (mol/L)	Excess adsorption (mmol/g)	Cummulative error (%)	Percentage error (%)	Percentage error @500 psi (%)
35	397.8	1.236	2.7	0.0073	0.652	0.01	1.7	2.5
35	569.2	1.9192	3.9	0.0105	1.686	0.02	1.2	
35	784.5	3.028	9.7	0.0262	3.285	0.03	1.0	
35	770.6	2.9436	43.6	0.1189	4.581	0.04	0.9	
35	779.5	2.9974	145.1	0.4093	5.223	0.05	1.0	
35	1385.5	15.77	753.6	2.8435	5.813	0.20	3.5	

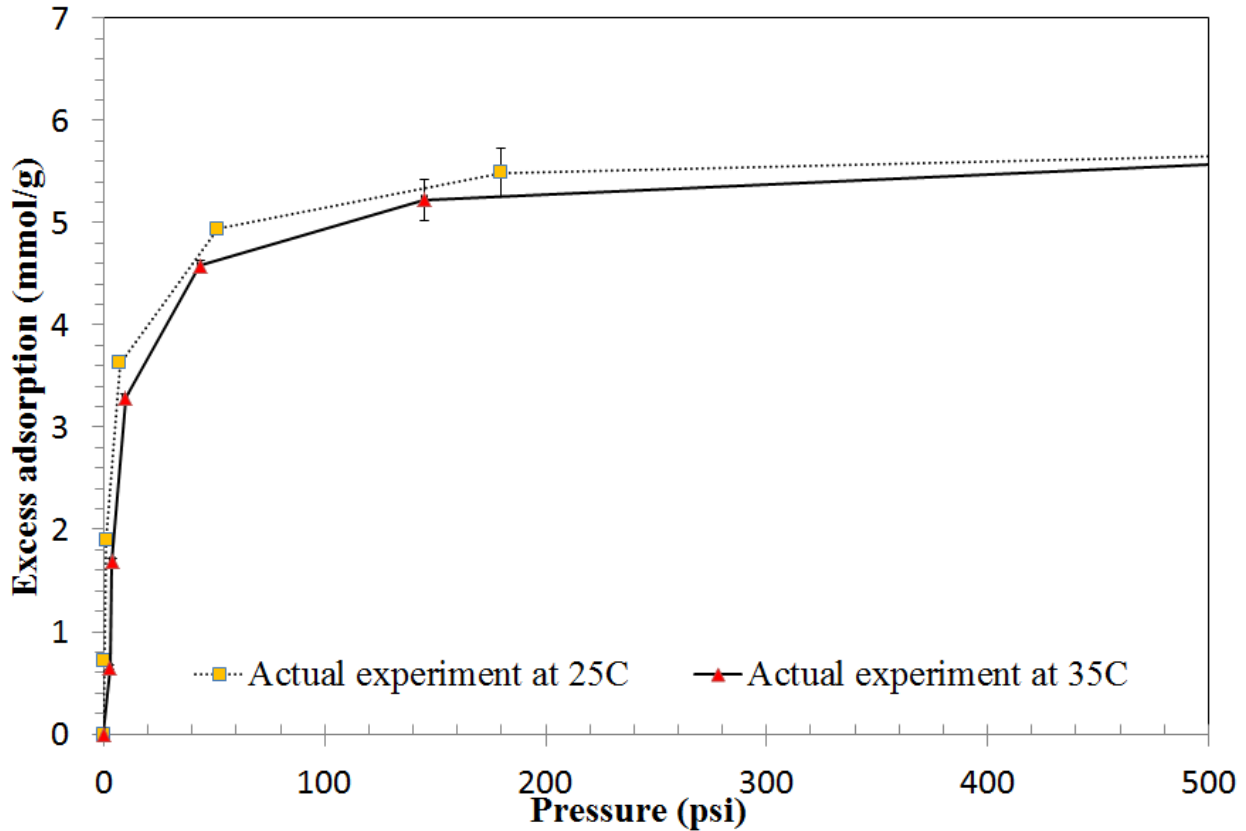


Figure 4.7: CO₂ excess adsorption isotherm at 25°C and 35°C as a function of equilibrium pressure. The relative error of excess adsorption at 500 psi for 25°C and 35°C are 2.6% and 2.5%, respectively.

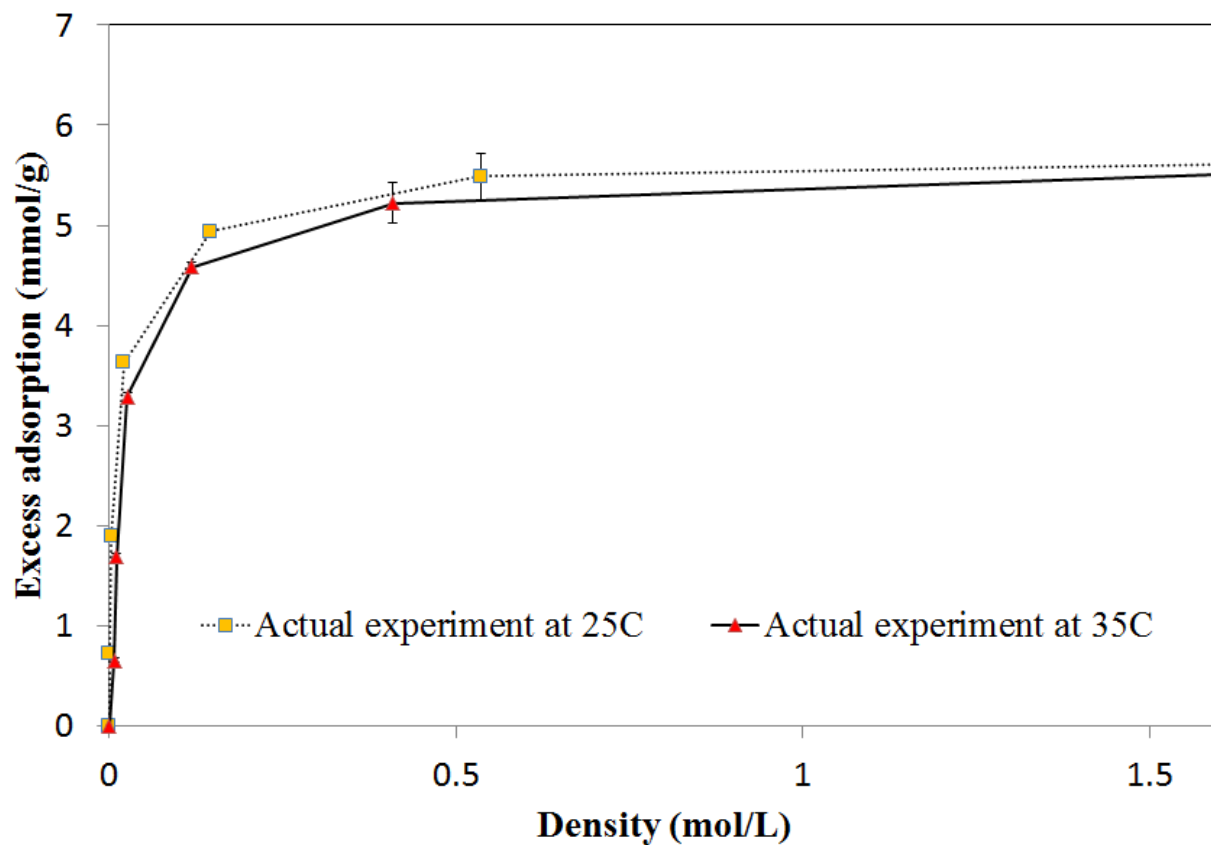


Figure 4.8: CO₂ excess adsorption isotherm at 25°C and 35°C as a function of equilibrium density. The relative error of excess adsorption at 500 psi for 25°C and 35°C are 2.6% and 2.5%, respectively.

Percentage uncertainties in excess adsorption from experimental tests at 25°C and 35°C up to 500 psi on 13X zeolite are slightly greater compared with those from virtual experiment, 2.6% and 2.5%, respectively, as can be seen in Figure 4.7 and Figure 4.8. Note that these values were obtained using linear extrapolation and can be seen in Table 4.7 (ie. page 46) and Table 4.8 (ie. page 46). While the apparent experimental uncertainties are small, the results from these tests are significantly different from those predicted in the previous sections that are based on literature data. The relative difference in excess adsorption values at 500 psi between experimental and virtual tests is approximately 9.4% and 8.2% at 25°C and 35°C, respectively. Also, the effect of temperature on the measured adsorption isotherms is surprisingly rather small, with the isotherm measured at 25°C being just slightly above the one measured at 35°C. These observations suggest that other factors may be affecting these experiments and these potential sources of errors will be addressed in Section 5.

4.6 Virtual tests on shale sample

When compared to a synthetic zeolite, shale can adsorb 10-15 times less CO₂ per unit weight of material. The purpose of this section is to assess the performance of the current manometric system in measuring gas adsorption on shale samples at representative conditions through a series of virtual tests. These virtual tests incorporate the same uncertainty in dose volume, uptake volume and sample volume that were founded in experimental test from Section 4.5.

4.6.1 CO₂ excess adsorption on New Albany shale - Case 1

As an example of general validity, the New Albany shale from Chareonsuppanimit's study (Chareonsuppanimit et al., 2012) is considered for these tests. Its adsorption parameters have been fitted using Langmuir isotherm curve and are reported in Table 4.9 together with other properties that characterize the adsorption isotherm curve. Figure 4.9 shows the excess adsorption isotherm curve of New Albany shale and percentage error at 500 psi and 1,600 psi.

Table 4.9: Parameters used to plot excess adsorption isotherm in New Albany shale in Case 1.

Solid weight (g)	22.7
Solid density, ρ_s (g/cm ³)	2.4
Standard deviation in dose volume (cm ³)	0.1
Standard deviation in uptake volume (cm ³)	1.1
Standard deviation in adsorbent volume (cm ³)	1.3
Saturation capacity, q_{sc} (mmol/cm ³)	0.71
b (cm ³ /mmol)	0.2
Temperature (°C)	55

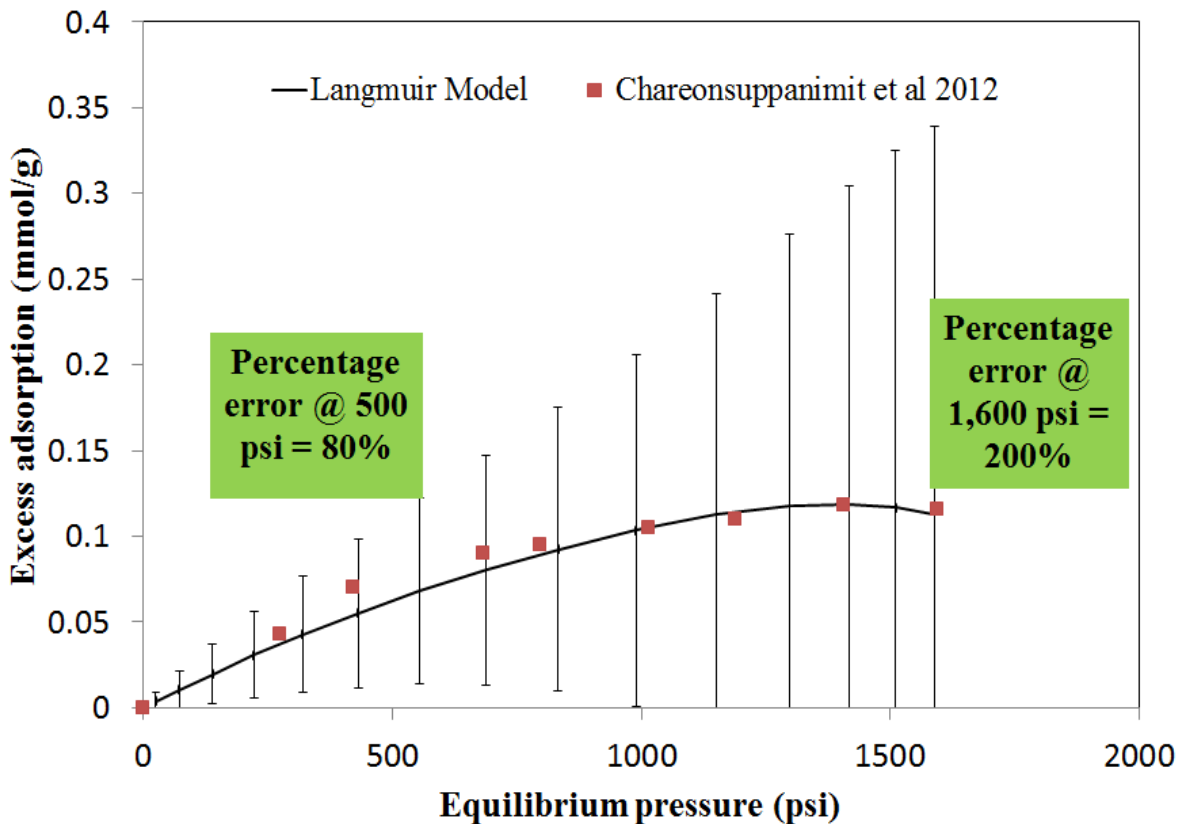


Figure 4.9: CO₂ excess adsorption isotherm of New Albany shale as a function of equilibrium pressure as computed from a virtual experiment together with experimental data from Chareonsuppanimit et al. (2012). Error bars and percentage error of excess adsorption are also included in the plot. Mass of adsorbent sample is 22.695 g.

As can be seen from Figure 4.9, the uncertainty is undoubtedly significant in the computed excess adsorbed amount and it increases with increasing equilibrium pressure. The percentage error of excess adsorption increases from 80% at 500 psi to 200% at 1,600 psi. As shown in the next section, this uncertainty needs to be reduced if this manometric system were to be used to measure adsorption isotherms on shale samples.

4.6.2 CO₂ excess adsorption on New Albany shale- Case 2

For this scenario, the mass of has been increased from 22.695 g to 50g, while keeping unchanged values for dose volume, uptake volume and adsorbent volume. Their uncertainties; however, are different since adsorbent volume has been changed. The latter is used to determine uncertainty in dose volume and uptake volume as previous mention in Section 4.4.2. Table 4.10 provides input parameters that have been used to plot adsorption isotherm.

Table 4.10: Adsorption parameters used to plot excess adsorption in New Albany shale in Case 2.

Solid weight (g)	50
Solid density, ρ_s (g/cm ³)	2.4
Standard deviation in dose volume (cm ³)	0.09
Standard deviation in uptake volume (cm ³)	0.4
Standard deviation in adsorbent volume (cm ³)	0.5
Saturation capacity, q_{sc} (mmol/cm ³)	0.71
b (cm ³ /mmol)	0.2
Temperature (°C)	55

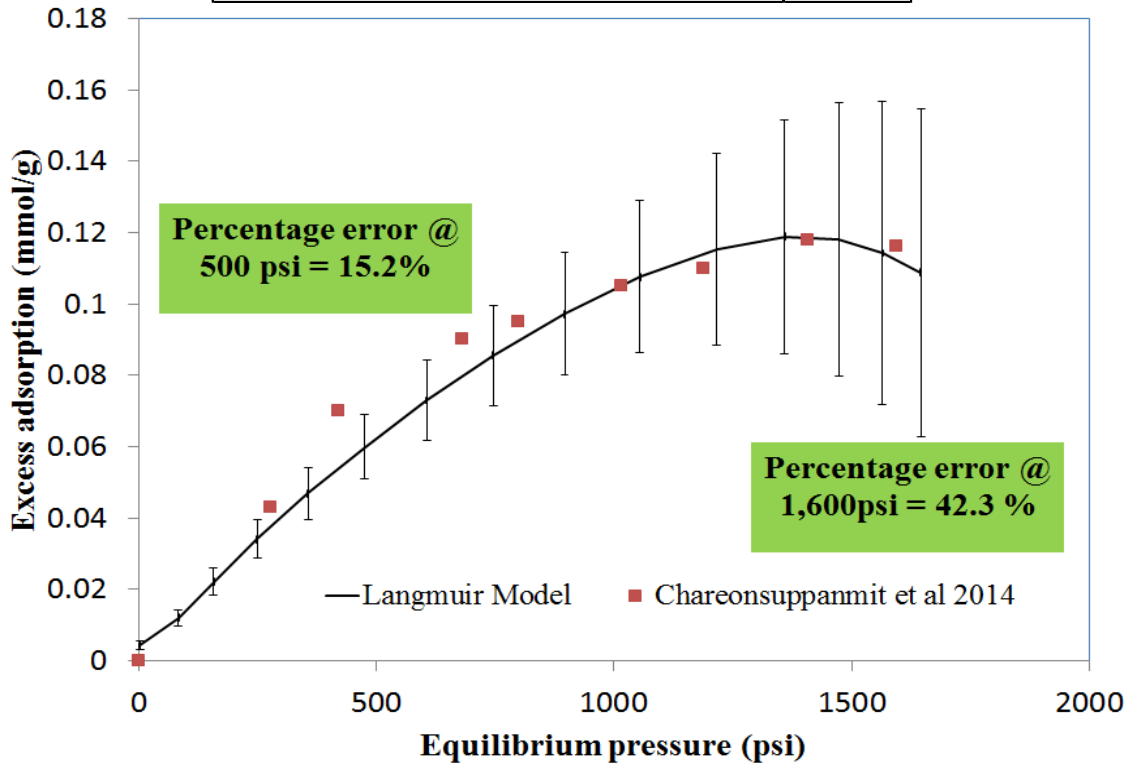


Figure 4.10: CO₂ excess adsorption isotherm of New Albany shale as a function of equilibrium pressure as computed from a virtual experiment together with experimental data from Chareonsuppanimit et al. (2012). Error bars and percentage error of excess adsorption are also included in the plot. Mass of adsorbent sample is 50g.

As can be seen from **Figure 4.10**, increasing in equilibrium pressure still results in greater uncertainty in excess adsorption when accounting errors in dose volume, sample volume and adsorbent volume, but the relative error is now smaller. The percentage error in this case at 500psi and 1,600 psi are 15.2% and 42.3%, respectively. It can be shown that uncertainties in excess adsorption can be further reduced if more materials are used to conduct the adsorption test.

4.6.2 CO₂ excess adsorption on New Albany shale- Case 3

As can be seen from the previous case, uncertainty in excess adsorption can be reduced by increasing the adsorbent volume. In this section, another virtual test has been conducted to see how uncertainties change by reducing the uncertainty in pressure gauge, from 0.25% to 0.05%. Table 4.11 provides input parameters that have been used to plot adsorption isotherm.

Table 4.11: Adsorption parameters used to plot excess adsorption in New Albany shale in Case 3.

Solid weight (g)	50
Solid density, ρ_s (g/cm ³)	2.6
Standard deviation in dose volume (cm ³)	0.02
Standard deviation in uptake volume (cm ³)	0.7
Standard deviation in adsorbent volume (cm ³)	0.1
Saturation capacity, q_{sc} (mmol/cm ³)	0.765
b (cm ³ /mmol)	0.212
Temperature (°C)	55
Uncertainty in pressure gauge(%)	0.05

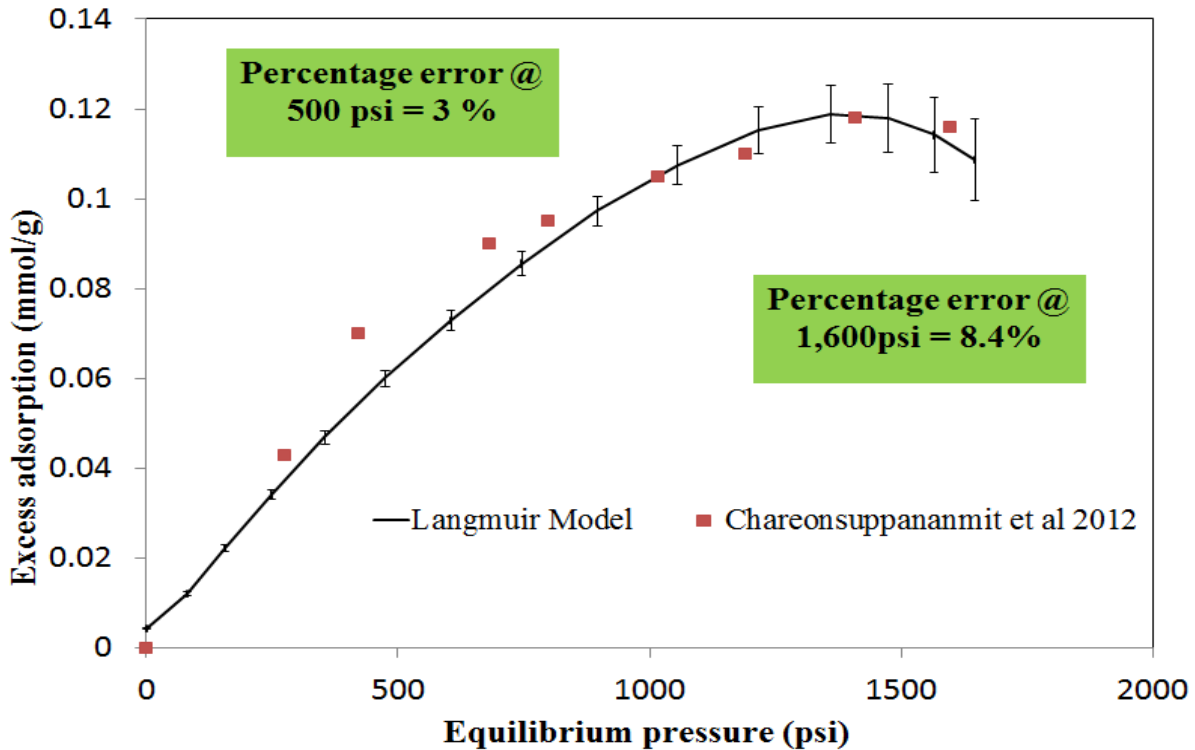


Figure 4.11: CO₂ excess adsorption isotherm of New Albany shale as a function of equilibrium pressure as computed from a virtual experiment together with experimental data from Chareonsuppananmit et al. (2012). Error bars and percentage error of excess adsorption are also included in the plot. Mass of adsorbent sample is 50g in this case and uncertainty in pressure gauge is 0.05%.

The uncertainties in excess adsorption isotherm at 500 psi and 1,600 psi in case 3 have significantly reduced compared to those results from case 2, as can be seen from Figure 4.11. Note that the only input differences between these two cases are uncertainties in pressure gauge. The uncertainties in excess adsorption in case 3 seem now to be more acceptable.

4.7 Other tests

This section introduces experimental tests that used to determine the leakage rate of the manometric system (Leak-off test), and to isolate the adsorption from experimental artifacts (Blank test).

4.7.1 Leak-off test

The accuracy of the excess adsorption isotherm depends on the measurement of the equilibrium pressure. The latter can be effected by gas leakage from the manometric system. The influence of leakage causes the adsorption isotherm to move upwards and could overestimate adsorbed gas density. In this study, a leakage test has been conducted using helium gas at temperature and pressure relevant to the adsorption test, 25°C and 500 psi. The manometric system was tested up to 500 psi and showed a maximum leak rate of 0.2psi/hour. This is considered insignificant and is in agreement with other studies (Belmabkhout et al., 2004).

4.7.2 Blank test

The purpose of performing the blank test is to identify the artifacts that could reflect excess adsorption and quantify the error in the overall excess adsorption isotherm. These artifacts could be inner wall adsorption, gas impurity, and other unknown factor. A blank test is performed similarly to the adsorption test; however, instead of working with an adsorbent material, a non-adsorbing sample is used. It is expected that from such a test, a zero excess adsorption isotherm is obtained. Stainless steel spheres are used to conduct the blank test and their amount is chosen so as to obtain a very similar sample volume as in the adsorption tests. One blank test has been conducted at 25°C temperature. The data and result of this blank test can be seen in Table 4.12. The result from this test is then used to correct 13X zeolite CO₂ excess adsorption as shown in Figure 4.12. The results from the blank test are suggesting that no particular artifact is affecting the experiment, as adsorption is always smaller than 0.004 mmol/g. This corresponds to a relative error of less than 0.1 % for zeolite samples and less than 4% for shale samples.

Table 4.12: Excess adsorption results from blank test at 25°C.

Temperature (°C)	Dosing pressure, P_d (psi)	Dosing density, ρ_{dc} (mol/L)	Equilibrium pressure, P_j (psi)	Equilibrium density, ρ_j (mol/L)	Blank Excess adsorption (mmol/g)
25	123.8	0.360	26.6	0.075	-0.00203
25	244.1	0.745	74.6	0.213	-0.00241
25	263.5	0.811	116.0	0.336	-0.00185
25	234.6	0.713	141.4	0.414	-0.00217
25	316.6	0.998	180.0	0.535	-0.00381

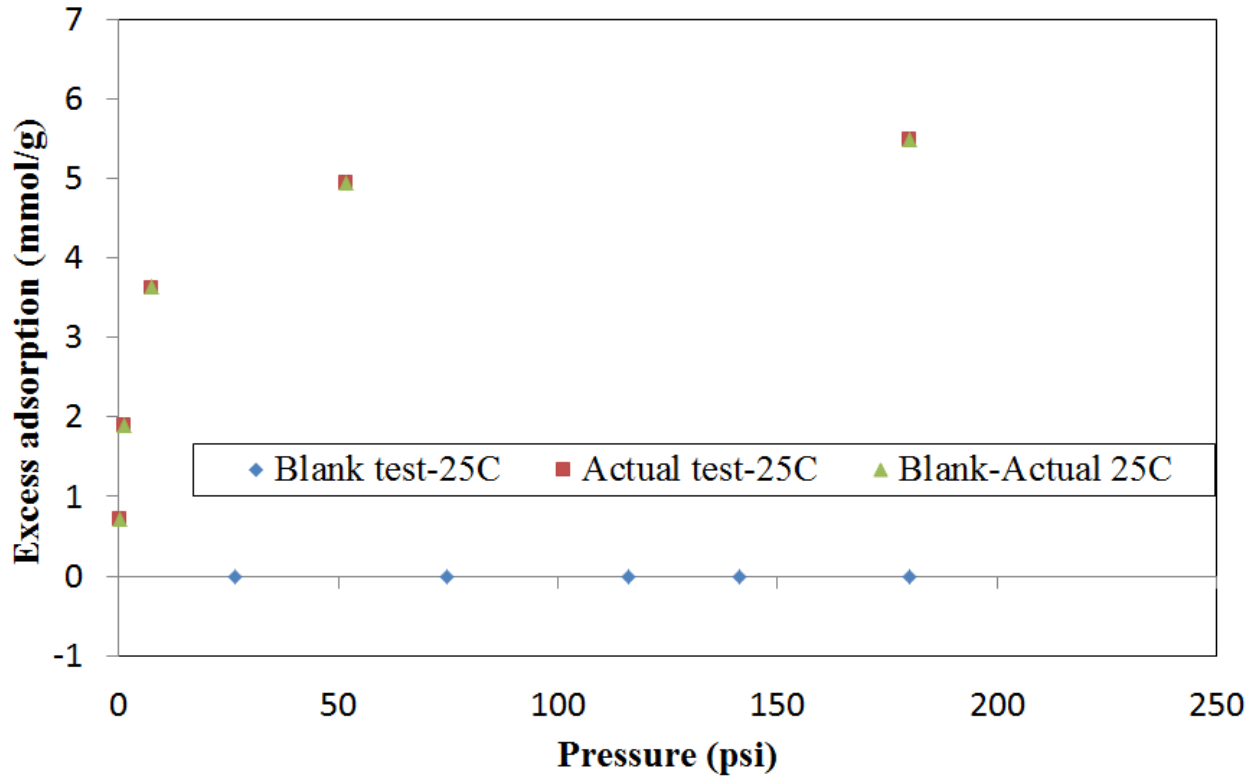


Figure 4.12: Excess adsorption from blank test at 25°C. The blank test results have been corrected with excess adsorption data from 13X zeolite.

CHAPTER 5
RESULTS AND DICUSSION

5.1. System volume

As previously shown, the size of the manometric system impacts the uncertainty in the measured dose- and uptake-cell volumes. By means of virtual experiments, three scenarios have been investigated corresponding to a total volume of 400 cm³, 150 cm³ and 82.2 cm³. The results of these tests are summarized in Table 5.1. As system volume decreases, uncertainties in dose and uptake volume also decrease. Accordingly, among the available options, a system volume of 82.2 cm³ that contains uptake volume of 69.8 cm³ and dose volume of 12.4 cm³ represents the best choice for conducting the experiment.

System Volume (cm ³)	Actual dose volume (cm ³)	Standard deviation of dose volume (cm ³)	Relative error of dose volume (%)	Actual uptake volume (cm ³)	Standard deviation of uptake volume (cm ³)	Relative error of uptake volume (%)	Actual adsorbent volume (cm ³)	Standard deviation of adsorbent volume (cm ³)	Relative error of adsorbent volume (%)
400	60.5	1.0	1.7	339.5	5.1	1.5	46	6.4	13.9
150	22.7	0.4	1.8	127.3	1.9	1.5	17.2	2.7	15.7
82.2	12.4	0.2	1.5	69.8	1.0	1.4	9.5	1.4	14.7

Table 5.1: Uncertainty in dose volume, uptake volume and adsorbent volume at different system volumes.

Moreover, the uncertainties obtained upon repeated experiments using the system with 82.2 cm³ (see Table 5.2) are close agreement with the values reported in Table 5.1. In other words, the virtual experiment represents a reliable method to design the experimental set-up and the assumptions used in these tests are valid. Note that the uncertainties from virtual tests are slightly greater than those from experimental test. This difference is due to the fact that virtual experiment has been performed 200 repetitions for 5 pressure steps while experimental test only conduct in 3 pressure steps. It is believed that if more experimental tests on system volume are carried out, the results of uncertainties would be similar to those from virtual tests.

Table 5.2: Uncertainties in dose volume, uptake volume and adsorbent volume from Virtual and Experimental test.

	Value (cm ³)	Uncertainties in Virtual test (cm ³)	Uncertainties in Experimental test (cm ³)
Dose volume (cm ³)	12.4	0.2	0.1
Uptake volume (cm ³)	69.8	1.0	1.1
Adsorbent volume (cm ³)	9.5	1.4	1.3

5.2 Excess adsorption

It can be seen that excess adsorption isotherm curves conducted at 25°C and 35°C exhibit a common behavior. The adsorbed amount of CO₂ on the 13X zeolite material increases very rapidly with the increase in pressure at lower pressures and it flattens as equilibrium pressure continues to increase as shown in Figure 4.8 (ie. page 47). In addition, the adsorption isotherm curve shows a slight effect of temperature on the CO₂ adsorption capacity. Adsorption is an exothermic process and it is therefore expected that the adsorption capacity decreases as temperature increases, as an increase in temperature provides more internal energy to CO₂ molecules in the gas phase, thus reducing the chance for CO₂ to be adsorbed in the adsorbent surface. However, the observed effect is rather small for the experiments reported here.

The excess adsorption amount of CO₂ on 13X zeolite at 25°C and 35°C up to 500 psi are 5.8mmol/g and 5.6 mmol/g, respectively. These values are significantly lower than previously published data. Excess adsorption from a study by Cavenati (Cavenati et al., 2004) at 25°C and 35°C on 13X zeolite are approximately 7.00 and 6.60 mmol/g, respectively (Cavenati et al., 2004). A comparison between the two data sets is shown in Figure 5.1.

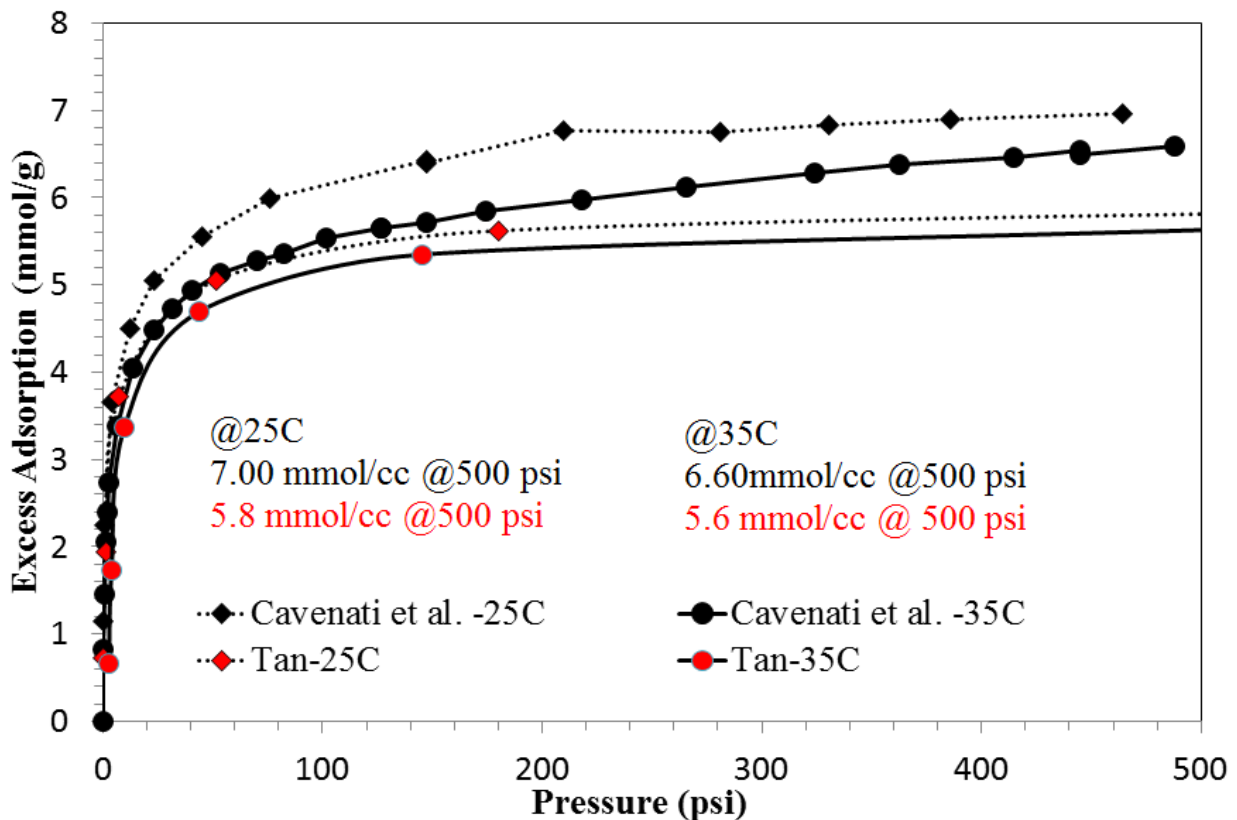


Figure 5.1: CO₂ excess adsorption on 13X zeolite at 25°C and 35°C obtained from this study and Cavenati study (Cavenati et al., 2004).

As anticipated above, the uncertainty analysis cannot explain these differences, as the applied method seems to be rather precise under the applied temperature and pressure conditions. It is believed that the lower adsorption values observed in this study may be the result of poor experiment practice; some of the potential sources of errors are as follows:

- Gas impurity: helium tests are normally conducted to determine the effective pore volume prior to the adsorption test. Without flushing and vacuuming the pressure line carefully, helium could possibly reside within the pressure line, thus reducing the density of the adsorbing CO₂ gas.
- Equilibrium time: in this study, only one hour has been waited to reach pressure and adsorption equilibrium. This time may be too short; it is suggested to longer tests are carried out to define the optimum equilibrium time. Also, this time may vary for different materials. Longer time may be needed at lower pressures to allow for gas to fully adsorb into smaller pores. Insufficient equilibration times will result an underestimation of the adsorption capacity of the zeolite materials and possibly affect the isotherm adsorption curve. Sample material such as shale contains significant amount of nanopores would require lengthy time to reach equilibrium. A true equilibrium might never be found due to kinetic restrictions (Gasparik et al., 2014). On the other hand, lengthy equilibration time requires manometric system that has low to none leakage rate or explicitly consider leakage rate in the mass balance equation (Van Hemert et al., 2009).
- Moisture: presence of residual moisture could be associated with the relatively low temperature (215°C) used for the regenerating of the samples. The suggested temperature for fully regenerating 13X zeolite materials is approximately 500°C. Therefore, it is possible that some of the pores within the zeolite cages are still partly occupied by other impurities, such as water. CO₂ adsorption data at 14.7 psi on 13X zeolites regenerated at different temperatures are summarized in Table 5.3. It can be seen that there is indeed a tendency for adsorption to increase with increasing regenerating temperature. For example, studies of Siriwardance et al. (2001) and McEwen et al. (2013) show excess adsorption of 3.6 and 1.7 mmol/g, respectively, when drying 13X zeolite at 25°C. Other studies show excess adsorption varies from 4.1 to 4.5 mmol/g when adsorbents regenerated at 320°C (Cavenati et al., 2004 and

Delago et al., 2014). The excess adsorption further increases from 4.3 to 4.7 mmol/g when 13X zeolite dried at 350°C (Hauchlum et al., 2014, Bezerra et al., 2011). When comparing excess adsorption from our study to those that have similar regenerating temperature at the same equilibrium pressure (14.7 psi) and temperature (25°C), our result, 4.0 mmol/g, is similar with other studies (3.9- 4.1 mmol/g) (Hyun et al., 1982 and McEwen et al., 2013).

The discrepancy between adsorption data measured in this study with literature data is believed to be a combination of the various sources of error listed above. Among them, the presence of residual moisture seems to play the most important role.

Table 5.3: CO₂ adsorption of 13X zeolite at different regenerating temperature.

Reference	Regenerating temperature (°C)	Pressure range (psi)	Testing temperature (°C)	Excess adsorption @ 14.7 psi (mmol/g)
Delago et al. (2014)	320	87	25	4.1
			35	3.8
Hyun et al. (1982)	194	20	25	3.9
Cavenati et al. (2004)	320	464	25	4.5
			35	4.1
Siriwardance et al. (2001)	25	350	25	3.6
Bezerra et al. (2011)	350	145	25	4.68
Hauchlum et al. (2014)	350	14.5	25	4.25
			35	3.9
McEwen et al. (2013)	25	14.7	25	1.7
	200			4.1

CHAPTER 6

CONCLUSIONS AND FUTURE RECOMMENDATIONS

6.1 Summary and conclusions

One feature that distinguishes unconventional from conventional gas reservoirs is the manner in which gas is stored. In conventional reservoirs, gases are stored as a compressive fluid in pore space and naturally fracture rocks. Fine-grained sedimentary rocks in shale reservoirs are characterized by a complex pore structure containing pores in the nanometer range that can store a significant amount of gas by adsorption. It is estimated that adsorbed gas can be a major fraction of the total GIP, up to 80%, due to the much larger density of the adsorbed fluid as compared to the density of gas. As a result, it is essential to quantify adsorbed gas content in unconventional reservoirs in order to disclose more reliable gas reserve and storage capacities estimates.

A conventional GIP calculation is commonly applied to estimate gas reserves and storage capacities. However, the former neglects the effect of pore space reduction due to gas adsorption in unconventional reservoirs, thus overestimating GIP. The modified volumetric GIP calculation developed by Ambrose and coworkers (Ambrose et al., 2012) takes into account the previous effect by arbitrarily choosing a value for the density of the adsorbed gas. However, a summary from literature studies highlights that larger discrepancies exist between estimates from different measurement techniques using representative fluids (such as CH₄ and CO₂) at elevated pressures, and the adsorbed density can actually range anywhere between the liquid and the solid state of the adsorbate. Examples have been performed in this study to demonstrate the variability in both the computed GIP (CH₄) and storage capacity (CO₂) due to the corresponding uncertainty in the adsorbed gas density by considering adsorption data on various shale plays situated all around the world. The range of adsorbed gas density of CH₄ and CO₂ for these shale plays varies between 0.19-0.88 g/cm³ and 0.36-1.30 g/cm³, respectively. Accordingly, these estimates further indicate that the relative difference of estimated GIP by considering free and total amount of CH₄ can vary between 10-45% and 6-27%, respectively. In case of CO₂, discrepancies are even greater and range between 30-90% and 15-50%, respectively.

A manometric system has been designed to measure excess adsorption data on porous solids that would enable the measurement of new adsorption data on shale samples. As a first step in this direction, synthetic 13X zeolite in pellet form has been used as a benchmarking

adsorbent to ensure the accuracy of our system. The system volume was calibrated using helium gas and an uncertainty analysis has been carried out to estimate errors in the measured volumes of the various components within the system, thus including dosing reservoirs and adsorbent's volume. These uncertainties have been used to predict errors in the estimated by means of simple rules of error propagation. The computed relative error takes a value of about 3% at 25°C and 35°C and at 500 psi.

CO₂ adsorption isotherms have been measured on 13X zeolite at 25 and 35°C and up to 500 psi. A disagreement of about 10% has been found when these data are compared with those reported in the literature. The lower regeneration temperature applied in this study is believed to be the reason for such discrepancies, thus allowing for some impurities to remain within the pore space of the adsorbent.

Virtual experiments have been conducted to investigate the potential of the current system to measure adsorption on less adsorbing material such as mudrocks. It is shown that relative uncertainties in measured adsorption isotherms are much larger and can be as high as 200% at 1600 psi. Guidelines are provided to significantly reduce these errors and include an increase in the adsorbent volume (and mass) together with a higher accuracy of the pressure transducers.

6.2 Future recommendations

Several changes can be implemented to the current system to better estimate excess gas adsorption on 13X zeolite materials.

- The current drying temperature needs to be increased from 215°C to 500°C to ensure completely removal of residual moisture.
- If possible, pressure gauges should be attached next to the dose cell and uptake cell to have a more accuracy pressure reading. In addition, ensure that the pressure gauges are completely submerged in the water bath. The latter step would help in reducing uncertainties at higher pressures since CO₂ gas density is very sensitive to slight temperature variations.
- A larger thermal bath could be utilized to ensure complete submersion of manometric system. This would ensure equilibrium across the entire system.

- The accuracy of the current pressure gauges should be improved from 0.25% to 0.05% to better estimate excess adsorption in weakly adsorbing materials.

The literature is still in disagreement with respect to the role of TOC, thermal maturity, and clay content on the adsorption capacity on shales. As a result, more studies need to be carried out to further understand the factors that control adsorption mechanisms in mudrocks.

A standardized method to measure the adsorption on weakly adsorbing material should be developed, thus including adsorbent characterization, regeneration and adsorption measurement. In this context, inter-laboratory comparison and benchmarking studies could be beneficial.

LIST OF SYMBOLS

B_g	gas formation volume factor, reservoir volume/surface volume
B_o	temperature dependence (cm^3/mol)
G_a	adsorbed- gas storage capacity (SCF/ton)
G_f	free- gas storage capacity (SCF/ton)
G_{sL}	Langmuir storage capacity (SCF/ton)
G_{st}	total gas storage capacity (SCF/ton)
M	apparent molecular weight (lbm/lbm-mol)
m^a	actual amount adsorbed (SCF/ton or mol)
m_{AD}	mass of adsorbent material (g)
m^{excess}	excess adsorbed amount (SCF/ton or mol)
n^a	amount of adsorbed fluid (mol)
n_1	adsorbed amount at step 1 (mol)
p	pressure (psia)
q_{sc}	saturation capacity (mmol/cm^3)
p_L	Langmuir pressure (psia)
R	universal gas constant ($0.08314 \text{ L}\cdot\text{bar}/\text{k}\cdot\text{mol}$)
S_w	water saturation (fraction)
T	temperature ($^{\circ}\text{F}$)
V^a	actual adsorbed volume (cm^3)
V_{DC}	dose chamber volume (cm^3)
V_s	solid volume (cm^3)
V_{SC}	sample chamber volume (cm^3)
ΔU	energy adsorption (kcal/mol)
ρ	free gas phase density (mol/cm^3)
ρ_b	bulk rock density (g/cm^3)
ρ^a	adsorbed gas phase density (mol/cm^3)
ρ_j	density at equilibrium for step j (mol/cm^3)
ρ_1	density at equilibrium inside the system for step 1 (mol/cm^3)
ρ_{j-1}	density at equilibrium for previous step j (mol/cm^3)
ρ_{DCj}	density inside dose chamber before equilibrium for step j (mol/cm^3)

$\rho_{DC,1}$ density inside dose chamber before equilibrium for step 1 (mol/cm^3)
 φ total porosity (fraction)

REFERENCE CITED

- Ambrose R.J., Hartman R.C., Diaz-Campos.M., Akkutlu I.Y., Sondergeld C.H. 2012. Shale Gas-in-Place Calculations Part I: New Pore-Scale Considerations. SPE Journal. Volume 17. Pages 219-229.
- Belmabkhout, Y., Frere, M., Weireld, G. 2004. High-pressure adsorption measurements. A comparative study of the volumetric and gravimetric methods. Measurement of Science and Technology. Volume 15. Pages 848-858.
- Beaton, P., Pawlowicz, G., Anderson, A., Berhane, H. and Rokosh, D. 2010. Rock eval, total organic carbon and adsorption isotherms of the Duvernay and Muskwa formations in Alberta: Shale gas data release. Energy Resources Conservation Board.
- Bezerra, D., Oliveira, R., Vieira, R., Cavealcante, C. and Azevedo, D. 2011. Adsorption of CO₂ on nitrogen-enriched activated carbon and zeolite 13. Adsorption. Volume 17. Pages 235-246.
- Busch, A., Alles, S. Gensterblum, Y., Prinz, D. Dewhurst, D.N., Raven, M.D., Stanjek, H. and Krooss, B.M. 2008., Carbon dioxide storage potential of shales. International Journal of Greenhouse Gas Control, Volume 2. Pages 297-307.
- Cavenati, S., Grande, C. and Rodrigues, A. 2004. Adsorption equilibrium of methane, carbon dioxide, and nitrogen on zeolite 13X at high pressures. Journal of Chemical and Engineering Data. Volume 49. Pages 1095-1101.
- Chalmers, G. and Bustin, M. 2008. Lower cretaceous gas shales in northeastern British Columbia, Part II: evaluation of regional potential gas resources. Bulletin of Canadian Petroleum Geology. Volume 56. Pages 22-61.
- Chareonsuppanimit, P., Mohammad, S., Robinson, R., Gasem, K. 2012. High-pressure adsorption of gases on shales: Measurements and modeling. International Journal of Coal Geology. Volume 95. Page 34-46.
- Curtis, J.B. 2002. Fractured shale-gas systems. AAPG Bulletin. Volume 86. Pages 1921-1938.
- Day, S., Sakurovs, R. and Weir S. 2008. Supercritical Gas Sorption on Moist Coals. International Journal of Coal Geology. Volume 74. Pages 203–214.
- DeGance, A. E.1992. Multicomponent High-Pressure Adsorption Equilibria on Carbon Substrates: Theory and Data. Fluid Phase Equilibria. Volume 78. Page 99.
- Delgado, J., Agueda, V., Uguina, M., Sotelo, J., Brea, P. and Grande, C. 2014. Adsorption and diffusion of H₂, CO, CH₄, and CO₂ in BPL activated carbon and 13X zeolite: evaluation of performace in pressure swing adsorption hydrogen purification by simulation. Industries and Engineering Chemistry Research. Volume 53. Pages 15414-15426.

- Dubin. M. 1960. The potential theory of adsorption of gases and vapors for adsorbents with energetically nonuniform surfaces. *Chemistry Review*. Volume 60. Pages 235-241.
- Ellis, G.S., Zhang, T., Lewan, M., Peng, S. and Hu, H. 2014. Experimental study of methane adsorption on organic matter in mudstones: Implications for natural gas storage in Unconventional reservoirs. AAPG annual conventional and exhibition.
- Energy Information Administration (EIA). 2013. Technically Recoverable Shale Oil and Shale Gas Resources: An Assessment of 137 Shale Formation in 41 Countries Outside the United States. U.S. Department of Energy, Washington, June 10, 2013. <http://www.eia.gov/analysis/studies/worldshalegas/>
- Gasparik, M., Ghanizadeh, A., Bertier, P., Gensterblum, Y., Bouw, S., and Krooss, B. M. 2012. High pressure methane sorption isotherms of black shales from the Netherlands. *Energy Fuels* 26. Volume 8. Pages 4995-5004.
- Gasparik, M., Ghanizadeh, A., Gensterblum, Y. and Krooss, B. M. 2013. Multi-temperature method for high-pressure sorption measurements on moist shales. *AIP. Review of Scientific Instruments*. Volume 84. Pages 085116-1 to 9.
- Gasparik, M., Bertier, P., Gensterblum, Y., Ghanizadeh, A. 2014. Geological controls on the methane storage capacity in organic-rich shales. *International Journal of Coal Geology*. Volume 123. Pages 34-51.
- Gou, S. 2013. Experimental study on isothermal adsorption of methane gas on three gas samples from Upper Paleozoic strata of the Ordos Basin. *Journal of Petroleum Science and Engineering*. Volume 110. Pages 132-138.
- Gou, H., Jia, W., Peng, P., Lei, Y., Luo, X., Cheng, M., Wang, X., Zhang, L., Jiang, C. 2014. The composition and its impact on the methane sorption of lacustrine shales from the Upper Triassic Yangchang Formation, Ordos Basin, China. *Marine and Petroleum Geology*. Volume 57. Page 509-520.
- Haydel, J.J. and Kobayashi, R. 1967. Adsorption equilibria in the methane propane-silica gel system at high pressure. *I&EC Fundamental*. Volume 4. Pages 564-554.
- Hauchhum, L. and Mahanta, P. 2014. Carbon dioxide adsorption on zeolites and activated carbon by pressure swing adsorption in a fixed bed. *Int J Energy Environment Eng*. Volume 5. Pages 349-356.
- Hu, H., Zhang, T., Camacho, W., Ellis, G., Lewan, M. and Zhang, X. 2015. Experimental investigation of changes in methane adsorption of bitumen-free Woodford Shale with thermal maturation induced by hydrous pyrolysis. *Marine and Petroleum Geology*. Volume 59. Pages 114-128.

- Hyun, S. H. and Danner, R. P. 1982. Equilibrium adsorption of ethane, ethylene, isobutane, carbon dioxide, and their binary mixtures on 13X molecular sieves. *J. Chem. Eng. Data*. Volume 27. Pages 196–200.
- Ishida, T., Aoyagi, K., Niwa, T., Chen, Y., Murata, S., Chen, Q., Nakayama, Y., 2012. Acoustic emission monitoring of hydraulic fracturing laboratory experiment with supercritical and liquid CO₂. *Geophysical Research Letters*, Volume 39. Pages L16309-1 to 6.
- Jarvie, D.M., Hill, R.J., Ruble, T.E. and Pollastro, R.M., 2007. Unconventional shale-gas systems: The Mississippian Barnett Shale of north-central Texas as one model for thermogenic shale-gas assessment. *AAPG Bulletin*. Volume 91. Pages 475-499.
- Jeon, P.R., Choi, J., Yun, T.S., Lee, C.H. 2014. Sorption equilibrium and kinetics of CO₂ on clay minerals from subcritical to supercritical conditions: CO₂ sequestration at nanoscale interfaces. *Chemical Engineer Journal*. Volume 255. Pages 705-715.
- Ji, L., Zhang, T., Miliken, K., Qu, J., Zhang, X. 2012. Experimental investigation of main controls to methane adsorption in clay-rich rocks. *Applied geochemistry*. Volume 27. Pages 2533-2545.
- Kelemen S.R. and Kwiatek, L.M. 2009. Physical properties of selected block Argonne premium bituminous coal related to CO₂, CH₄, and N₂ adsorption. *International Journal of Coal Geology*. Volume 77. Pages 2–9.
- Kross, B.M, Van Bergen, F., Gensterblum, Y., Siemons, N. 2002. High pressure methane and carbon dioxide adsorption on dry and moisture-equilibrated Pennsylvanian coals. *International Journal of Coal Geology*. Volume 51. Pages 69-92.
- Kuila U. and Prasad, M. 2013. Specific surface area and pore size distribution in clays and shales. *Geophysical Prospecting*. Volume 63. Pages 341-362.
- Lane, H.S., David, E.L., Watson, A.T.E.D. 1991. Characterizing the role of desorption in gas production from Devonian shales. *Energy Sources*. Volume 13. Pages 337-359
- Langmuir, I.1918. The adsorption of gases on plane surface of glass, mica and platinum. *The Research Laboratory of The General Electric Company*. Pages 1361–1402.
- Levine, R. 1987. Influence of coal composition on the generation and retention of coalbed natural gas. *Coalbed Methane Symposium*. Pages 15-18.
- Liu, D., Yuan, P., Liu, H., Li, T., Tan, D., Yuan, W., He, H. 2013. High-pressure adsorption of methane on montmorillonite, kaolinite, and illite. *Applied Clay Science*. Volume 85. Pages 25-30.

- Lu, X., Li, F. and Watson, A. 1995. Adsorption measurements in Devonian shales. *Fuel*. Volume 74. Pages 599-603.
- Lui, Y. and Wilcox, J. 2012. Effects of surface heterogeneity on the adsorption of CO₂ in microporous carbons. *Environmental Science and Technology*. Volume 3. Pages 1940-1947.
- Loucks, R., Reed, R., Ruppel, S., Jarvie, D. 2009. Morphology, genesis, and distribution of nanometer-scale pores in siliceous mudstones of the Mississippian Barnett shale. *Journal of Sedimentary Research*. Volume 79. Pages 848-861.
- Marc, R.B, Bustin, A., Ross, D., Chalmers, G., Murthy, V., Laxmi, C., Cui, X. 2009. Shale gas opportunities and challenges. University of British Columbia.
- Mavor, M.J., Owen, L.B., Pratt, T.J. 1990. Measurement and evaluation of coal sorption isotherm data. SPE 20728. SPE 65th Annual Technical Conference and Exhibition, New Orleans. LA.
- McCarthy, K., Niemann, M., Palmowski, D., Peters, K., Stankiewica, A. 2011. Basic Petroleum Geochemistry for Source Rock evaluation. *Oilfield Review Summer*. Volume 23.
- McEwen, J. Hayman, J. and Yazaydin, O. 2013. A comparative study of CO₂, CH₄ and N₂ adsorption in ZIF08, Zeolite-13X and BPL activated carbon. *Chemical Physics*. Volume 412. Pages 72-76.
- Moghaddam, N.D. 2013. Sorption of methane and ethane on Beligan black shale using a manometric setup. International Research Training Group. Technical University of Delft.
- Mohammad, S., Fitzgerald, J., Robinson, R. L., Gasem, K. A. M. Experimental uncertainties in volumetric methods for measuring equilibrium adsorption. *Energy Fuels* 2009. Volume 23. Pages 2810–2820.
- Montgomery, S.L., Jarvie, D.M., Bowker, K.A., Pallastro, R.M. 2005. Mississippian Barnett Shale, Fort Worth basin, north central Texas” Gas-shale play with multi-trillion cubic foot potential. *AAPG Bulletin*. Volume 89. Pages 155-175.
- National Science Foundation. 2012. Identification of fundamental interfacial and transport phenomena for the sustainable deployment of hydraulic shale fracturing – Role of chemical used, NSF Grant Number CBET-1229931, Workshop Report, September 2012.
- Pini R. 2014. Interpretation of net and excess adsorption isotherms in microporous adsorbents. *Microporous and Mesoporous Material*. Volume 187. Pages 40-52.
- Qinglin H., Sundaram, S.M. and Farooq, S. 2003. Revisiting transport of gases in the micropores of carbon molecular sieves. *Langmuir*. Volume 19. Pages 393-405.

- Rexer, T., Benham, M., Aplin, A., Thomas, M. 2013. Methane adsorption on Shale under simulated geological temperature and pressure conditions. *Energy and Fuels*. Volume 27, pages 3099-3109.
- Rexer, T., Mathia, E., Aplin, A., Thomas, M. 2014. High-pressure methane adsorption and characterization of pores in Posidonia Shales and isolated kerogens. *Energy and fuels*. Volume 28. Pages 2886-2901.
- Ross, D.J.K. and Bustin, R.M., 2009. Characterizing the shale gas resource potential of Devonian- Mississippian strata in the Western Canada sedimentary basin: application of an integrated formation evaluation. *AAPG Bulletin* 92, 87-125
- Santos, J.M. 2012. Gas sorption measurements under effective stress and adsorption layer effect. MSc Thesis, University of Oklahoma, Norman, Oklahoma
- Sircar, S. and Myers, A. L. 1971. Adsorption from liquid mixtures from solids: Thermodynamics of excess properties and their temperature coefficients. *Adsorption Technology*. Volume 67. Pages: 11.
- Sircar, S. and Wang, C. 2013. Design of high pressure differential volumetric adsorption measurements with increased accuracy. Department of Energy and Mineral Engineering. The Pennsylvania State University.
- Siriwardane, R., Shen, M., Fisher, E. and Poston, J. 2001. Adsorption of CO₂ on molecular sieves and activated carbon. *Energy and Fuel*. Volume 15. Page 279-284.
- Tan, J. 2014. Shale gas potential of major marine shale formations in the Upper Yangtze Platforms, South China. PhD Dissertation. University of Berlin.
- Van Bergen, F., Spiers, C., Floor, G. and Bots P. 2009. Strain development in unconfined coals exposed to CO₂, CH₄ and Ar: effect of moisture. *International Journal of Coal Geology*. Volume 77. Pages 43–53
- Valenza, J.J., Drenzek, N., Marques, F., Pagels, M. and Mastalerz, M. 2013. Geochemical controls on shale microstructure. *Geology*. Volume 41. Pages 611 -614.
- Van Hemert, P., Bruining, H., Rudolph, E.S., Wolk, K.H. and Maas, J.G. 2009. Improved manometric setup for the accurate determination of supercritical carbon dioxide sorption. *AIP. Review of scientific instruments*. Volume 80. Pages 1 to 11
- Wakasugi, Y., Ozawa, S. and Ogino, Y. 1981. Physical Adsorption of Gases at High Pressure. *J. Colloid Interface Sci*. Volume 79. Page 399.
- Wang, S., Song, Z., Cao, T. and Song, X. 2013. The methane sorption capacity of Paleozoic shales from the Sichuan Basin, China. *Marine and Petroleum Geology*. Volume 44. Pages 112-119.

- Weniger, P., Kalkreuth, W., Busch, A., Krooss, B. 2010. High pressure methane and carbon dioxide sorption on coal and shale samples from the Parama basin, Brazil. *International Geology Coal*. Volume 84. Pages 190-205.
- Zhang, T., Ellis, G., Ruppel, S., Milliken, K., Yang, R. 2012. Effect of organic-matter type and thermal maturity on methane adsorption in shale-gas systems. *Organic Geochemistry*. Volume 47. Pages 120-131.
- Zhou, L., Zhou. Y., Bai, S. et al. 2001. Determination of the adsorbed phase volume and its application in isotherm modeling for the adsorption of supercritical nitrogen on activated carbon. *Journal of Colloid and Interface. Science*. Volume 239. Pages 33-38.

APPENDIX A-DERIVATION OF EQUATIONS AND UNIT CONVERSIONS

A.1 Unit Conversions

For Equation 3.1, since the desired unit is in SCF/ton, the following conversion has been done to reach that goal. The ideal gas law equation of state has been used. The standard temperature and standard pressure for this equation are 59°F and 14.7 psi.

$$\begin{aligned} \frac{V}{n} &= \frac{RT}{p} \\ \frac{V}{n} &= \frac{RT}{p} = \frac{10.73159 * ft^3 * psi}{R * lb - mol} * \frac{519.67 R}{14.7 psi} * \frac{2000 lb}{1 ton} \\ \frac{V}{n} &= 758960 \frac{ft}{ton * mol} \\ \frac{n}{V} &= 1.318 * 10^{-6} \frac{ton * mol}{ft^3} \end{aligned} \quad (A.1)$$

With the density in g/cm³ and then desired units in SCF/ton, the following conversion has been done to achieve that goal

$$\begin{aligned} \frac{g}{cm^3} &\rightarrow \frac{scf}{ton} \\ \frac{g}{cm^3} &= \frac{1.10231 * 10^{-6} ton}{1 g} * \frac{28318 cm^3}{ft^3} = 0.0311 \frac{ton}{scf} \\ \frac{1}{0.0311 \frac{ton}{scf}} &= 32.1 \frac{scf}{ton} \end{aligned} \quad (A.2)$$

The conversion from mmol/g to SCF/ton is derived and can be observed in the following section. The ideal gas law equation of state has been used to convert to scf/ton

$$\begin{aligned} \frac{V}{n} &= \frac{RT}{p} = \frac{0.08314 * L * bar}{K * mol} * \frac{288.7 * K}{1.013 * bar} * \frac{0.035314 ft^3}{L} \\ \frac{V}{n} &= 0.836 \frac{scf}{mol} \end{aligned} \quad (A.3)$$

Then simple unit conversion has been done to convert mmol/g to mol/ton

$$\frac{mmol}{g} \Rightarrow \frac{1g}{1.1023E^{-6}ton} * \frac{1mol}{1000mmol} = 907.178 \frac{mol}{ton} \quad (A.4)$$

Combine these two conversions, A-3 and A-4 and we will obtain SCF/ton.

$$V = 0.836 \frac{scf}{mol} * 907.178 \frac{mol}{ton}$$

$$V = 759.078 \frac{scf}{ton} \quad (A.5)$$

A.2 Derivation of Equations

This section includes derivations of equations used in this work.

A.2.1 Equation 4.1-Volume ratio in an empty system

This equation is used to determine the volume ratio between dose cell and uptake cell in an empty system using helium gas. In order to do so, helium gas is first injected into dose cell and then expanded into uptake cell. Pressure reading before and after helium expansion is recorded. Next Valve 2 is closed and helium gas is injected into dose cell. The same procedure is repeated until reaching a desire pressure.

For the first helium gas expansion, the following equation is obtained using material balance concept

$$\rho_{DC,1} V_{DC} = \rho_1 (V_{DC} + V_{SC}) \quad (A.6)$$

However, Equation A.6 is only applicable to solve for volume ratio at first step. We need an equation that allows us to determine volume ratio at other pressure steps. For the second step the following equation is obtained:

$$\rho_{DC,2} V_{DC} + \rho_{j-1} V_{SC} = \rho_j (V_{DC} + V_{SC})$$

The above equation can be simplified and generalized to solve to V_{sc} at any other pressure steps, as can be seen in Equation A.7:

$$\rho_{DC,j} V_{DC} + \rho_{j-1} V_{SC} = \rho_j V_{DC} + \rho_j V_{SC}$$

$$V_{SC} (\rho_{j-1} - \rho_j) = V_{DC} (\rho_j - \rho_{DC,j})$$

$$\frac{V_{SC}}{V_{DC}} = \frac{(\rho_j - \rho_{DC,j})}{(\rho_{j-1} - \rho_j)} \quad (\text{A.7})$$

A.2.2 Equation 4.2-Volume ratio with reference volume

Another ratio volume equation is derived in this section. This equation, however, contain a known reference volume (stainless steel spherical ball). The equation derived in this section is then used with Equation A.7 to determine dose cell and uptake cell. The same exact procedure is carried out, but this time a known amount of reference volume is placed inside the uptake cell. For the first helium expansion, the following equation is obtained.

$$\rho_{DC,1}V_{DC} = \rho_1(V_{DC} + V_{SC} - V_R) \quad (\text{A.8})$$

Again, Equation A.8 only works at the first pressure step. We need an equation that allows us to determine volume ratio at other pressure steps. For the second step the following equation is obtained:

$$\rho_{DC,j}V_{DC} + \rho_{j-1}(V_{SC} - V_R) = \rho_j(V_{DC} + V_{SC} - V_R)$$

The above equation can be simplified and generalized to solve to V_{DC} at any other pressure steps, as can be seen in Equation A.9:

$$\begin{aligned} \rho_{DC,j} - \rho_j &= \frac{(V_{SC} - V_R)(\rho_j - \rho_{j-1})}{V_{DC}} \\ \rho_{DC,j} - \rho_j &= \frac{V_{SC}}{V_{DC}}(\rho_j - \rho_{j-1}) - \frac{V_R}{V_{DC}}(\rho_j - \rho_{j-1}) \\ \frac{V_R}{V_{DC}}(\rho_j - \rho_{j-1}) &= \frac{V_{SC}}{V_{DC}}(\rho_j - \rho_{j-1}) - \rho_{DC,j} + \rho_j \\ V_{DC} &= \frac{V_R(\rho_j - \rho_{j-1})}{\rho_{DC,j} + \frac{V_{SC}}{V_{DC}}(\rho_j - \rho_{j-1}) - \rho_j} \end{aligned} \quad (\text{A.9})$$

A.2.3 Equation 4.3-Error analysis in adsorbent volume

In this section, an error analysis has been done to estimate the uncertainties in adsorbent volume. This error analysis incorporates uncertainty in dose volume and uptake volume and

neglect uncertainty in dose density and equilibrium density. The following equation is obtained from helium expansion with adsorbent material inside the uptake cell. It is then simplified to solve for adsorbent volume, as can be seen in Equation A.10

$$\begin{aligned}
\rho_{DC,j}V_{DC} + \rho_{j-1}(V_{SC} - V_S) &= \rho_j(V_{DC} + V_{SC} - V_S) \\
\rho_{DC,j}V_{DC} + \rho_{j-1}V_{SC} - \rho_{j-1}V_S &= \rho_jV_{DC} + \rho_jV_{SC} - \rho_jV_S \\
V_{DC}(\rho_{DC,j} - \rho_j) + V_{SC}(\rho_{j-1} - \rho_j) &= V_S(\rho_{j-1} - \rho_j) \\
V_S &= V_{DC} \frac{(\rho_{DC,j} - \rho_j)}{(\rho_{j-1} - \rho_j)} + V_{SC}
\end{aligned} \tag{A.10}$$

Since adsorbent volume, V_S , is a function of V_{DC} and V_{SC} , then the uncertainty in V_S is obtained by taking the partial derivative of V_S with respect to V_{DC} and V_{SC} . Uncertainty in adsorbent volume can be estimated using Equation A.11.

$$\sigma V_S = \sqrt{\frac{\sigma V_{DC}^2 (\rho_{DC,j} - \rho_j)^2}{(\rho_{j-1} - \rho_j)^2} + V_{SC}^2} \tag{A.11}$$

A.2.4 Equation 4.4- Error analysis in excess adsorption

In this section, an error analysis has been done to estimate the uncertainties in excess adsorption. This error analysis incorporates uncertainty in dose volume, uptake volume, adsorbent volume and neglect uncertainty in dose density and equilibrium density. The following equation is obtained from CO₂ expansion with adsorbent material inside the uptake cell. It is then simplified to solve for adsorbed amount, n_a , as can be seen in Equation A.12

$$\begin{aligned}
\rho_{DC,j}V_{DC} + \rho_{j-1}(V_{SC} - V_S) + n_{i-1}^a &= \rho_j(V_{DC} + V_{SC} - V_S) + n_i^a \\
n_j^a &= n_{j-1}^a + V_{DC}(\rho_{DC,j} - \rho_j) - (V_{SC} - V_S)(\rho_j - \rho_{j-1})
\end{aligned} \tag{A.12}$$

Since adsorbent volume, n_a , is a function of V_{DC} , V_{SC} , and V_S then the uncertainty in n_a is obtained by taking the partial derivative of n_a with respect to V_{DC} , V_{SC} and V_S . Uncertainty in excess adsorbent amount can be estimated using Equation A.13.

$$\sigma m_j^{excess} = \sqrt{(\sigma m_{j-1}^{excess})^2 + \frac{\sigma V_{DC}^2 (\rho_{DC,j} - \rho_j)^2 + (\sigma V_{SC}^2 + \sigma V_S^2)(\rho_j - \rho_{j-1})^2}{m_{AD}^2}} \tag{A.13}$$

A.2.5 Equation 4.9- Excess adsorption amount

In this section, equation is derived to predict excess adsorption at multiple pressure steps. The following equation is obtained from the concept of material balance for step 1.

$$\rho_{DC,1}V_{DC} = \rho_1(V_{DC} + V_{SC} - V_S - V_1^a) + n_1$$

We can further simplify the above equation and solve for gas adsorption at Step 1.

$$n_1 = \rho_{DC,1}V_{DC} - \rho_1(V_{DC} + V_{SC} - V_S - V_1^a) \quad (\text{A.14})$$

At step 2, gas adsorption is estimated using the following equation.

$$\rho_{DC,2}V_{DC} + \rho_1(V_{SC} - V_S - V_1^a) + n_1 = \rho_2(V_{DC} + V_{SC} - V_S - V_2^a) + n_2 \quad (\text{A.15})$$

Substitute Equation A.14 into A.15 and we will obtain Equation A.16:

$$\begin{aligned} \rho_{DC,2}V_{DC} + \rho_1(V_{SC} - V_S - V_1^a) + \rho_{DC,1}V_{DC} - \rho_1(V_{DC} + V_{SC} - V_S - V_1^a) &= \rho_2(V_{DC} + V_{SC} - V_S - V_2^a) + n_2 \\ n_2 &= V_{DC}[(\rho_{DC,2} - \rho_2) + (\rho_{DC,1} - \rho_1)] - \rho_2(V_{SC} - V_S - V_2^a) \end{aligned} \quad (\text{A.16})$$

Equation A.16 is then used and simplified to find operating equation for excess adsorption at any pressure step, and can be seen in equation A.17

$$\begin{aligned} n_2 &= V_{DC}[(\rho_{DC,2} - \rho_2) + (\rho_{DC,1} - \rho_1)] - \rho_2(V_{SC} - V_S - V_2^a) \\ n_j &= V_{DC} \sum_{i=1}^j (\rho_{DC,i} - \rho_i) - \rho_j(V_{SC} - V_S - V_j^a) \\ n_j - V_j^a \rho_j &= V_{DC} \sum_{i=1}^j (\rho_{DC,i} - \rho_i) - \rho_j(V_{SC} - V_S) \end{aligned} \quad (\text{A.17})$$

Knowing the general equation of excess adsorption

$$m^{excess} = n^a - \rho V^a \quad (\text{A.18})$$

Now, Equation A.18 is used and incorporate into A.17, thus obtaining the following Equation A.19 :

$$m^{excess} = V_{DC} \sum_{i=1}^j (\rho_{DC,i} - \rho_i) - \rho_j(V_{SC} - V_S) \quad (\text{A.19})$$

APPENDIX B- GRAPHICAL METHOD

Graphical method is used to estimate the density of adsorbed gas using the relationship between excess adsorption isotherm and equilibrium density. Most of the excess adsorption isotherms from literature studies are demonstrated as a function of equilibrium pressure. Therefore, a conversion between pressures to density is required. This conversion can be made if experimental temperature is known. The following example will demonstrate how to obtain equilibrium density and how adsorbed gas density can be estimated using Graphical method.

The following example is taken from Weniger et al. (2010). CO₂ excess adsorption isotherm curve is plot as a function of equilibrium pressure. The experimental temperature conducted in this test is 45°C. First, equilibrium pressure is first converted into equilibrium density. This can be done by using equation of state (EOS). The result of this step can be seen in Table B.1.

Table B.1: Excess adsorption data from Permian shale in Brazil (Weniger et al., 2010)

Temperature (°C)	Pressure (MPa)	Equilibrium density (g/cm ³)	Excess adsorption (mmol/g)
45	0.08	0.001	0.003
	1.59	0.028	0.050
	3.09	0.059	0.072
	6.26	0.151	0.124
	8.70	0.302	0.144
	9.59	0.430	0.128
	10.17	0.522	0.112
	10.79	0.587	0.094
	11.64	0.641	0.082
	12.41	0.674	0.074
	13.18	0.699	0.072
	14.03	0.721	0.068
	14.61	0.742	0.066
	15.23	0.746	0.064
	15.73	0.755	0.060
	15.97	0.759	0.060
16.39	0.766	0.060	
16.70	0.771	0.058	
17.36	0.781	0.056	

Next, excess adsorption is plotted as a function of equilibrium density. Graphical method is then used to obtain the adsorption gas density, as can be seen in Figure B.1.

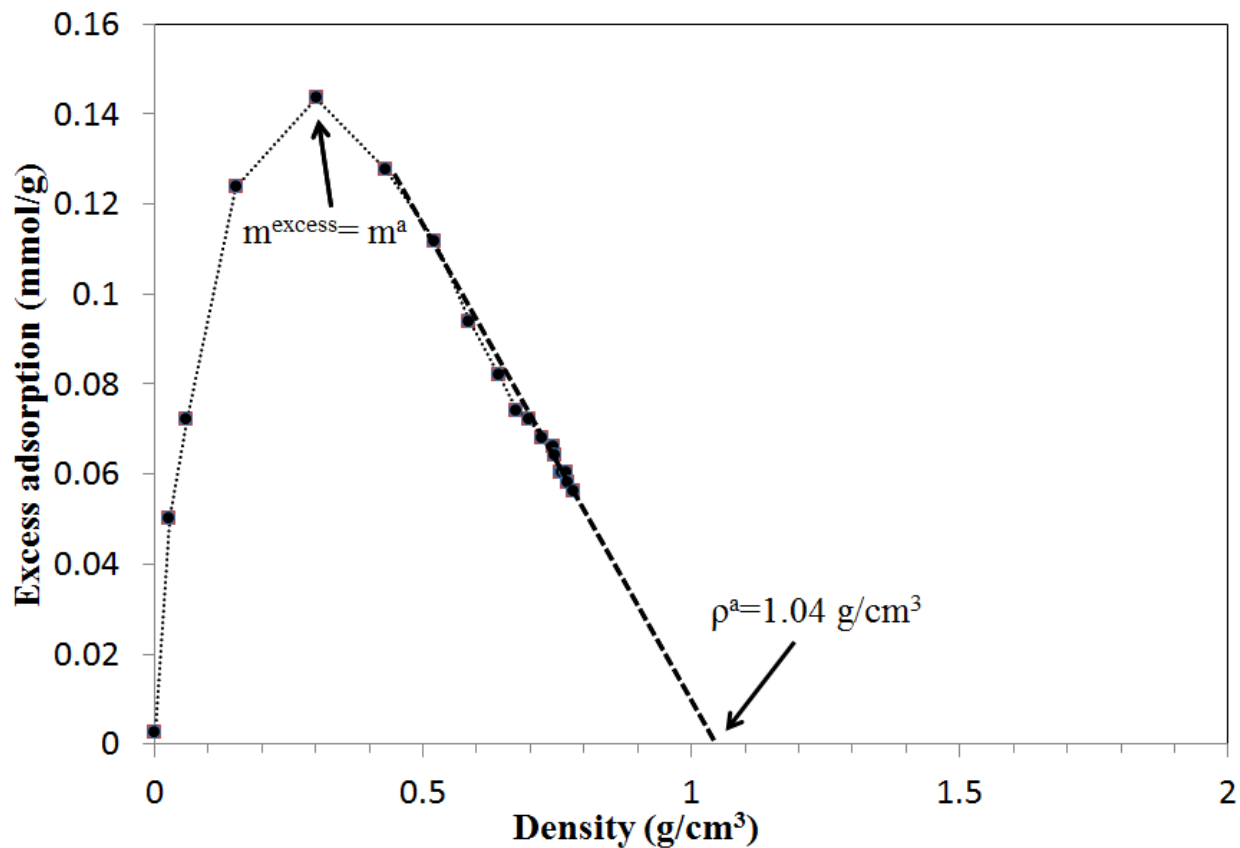


Figure B.1: Excess adsorption isotherms of CO₂ as a function of bulk density measured at 45°C on Permian shale sample. The dashed line has been used to fit a straight line to determine adsorbed gas density. This technique is known as Graphical Method. Weniger et al. (2012)

APPENDIX C-LANGMUIR ADSORPTION ISOTHERM

In order to carry out virtual experiment of excess adsorption in 13X zeolite and other shale plays, adsorption parameters are required to plot excess adsorption isotherm curve. These adsorption parameters are obtained by best fitting using Langmuir adsorption isotherm, from Equation C.1. An example has been performed to show how adsorption parameters, q_{sc} and b , are obtained.

$$m^{excess} = \frac{q_{sc}(b\rho)}{1 + b\rho} \left(1 - \frac{\rho}{\rho^a} \right) \quad (C.1)$$

The excess adsorption data used in this example is from Permian shale sample in Weniger et al. (2010), as can be seen in Table C.1.

Table C.1: Excess adsorption data from Permian shale in Brazil (Weniger et al., 2010)

Temperature (°C)	Pressure (MPa)	Equilibrium density (g/cm ³)	Excess adsorption (mmol/g)
45	0.08	0.001	0.003
	1.59	0.028	0.050
	3.09	0.059	0.072
	6.26	0.151	0.124
	8.70	0.302	0.144
	9.59	0.430	0.128
	10.17	0.522	0.112
	10.79	0.587	0.094
	11.64	0.641	0.082
	12.41	0.674	0.074
	13.18	0.699	0.072
	14.03	0.721	0.068
	14.61	0.742	0.066
	15.23	0.746	0.064
	15.73	0.755	0.060
	15.97	0.759	0.060
	16.39	0.766	0.060
16.70	0.771	0.058	
17.36	0.781	0.056	

The following procedure shows how adsorption parameters, q_{sc} and b , are determined:

- 1) Assuming a value of b and q_{sc} to solve for excess adsorption using equilibrium density.

Name this excess adsorption as m^{excess_1} .

- 2) Adjusting b and q_{sc} value until m^{excess_I} closely match with true excess adsorption as obtained from literature study

Result of b and q_{sc} from the current example can be seen in Table C.2.

Table C.2: Adsorption parameters b and q_{sc} obtained from Langmuir adsorption model. The adsorption isotherm curve is from Permian shale in Brazil (Weniger et al., 2010)

Temperature (°C)	Pressure (MPa)	Equilibrium density (g/cm ³)	Excess adsorption (mmol/g)	B (cm ³ /mmol)	Q _{sc} (mmol/cm ³)	m ^{excess_1} (mmol/g)
45	0.08	0.001	0.003	0.23	0.84	0.0022
	1.59	0.028	0.050			0.0404
	3.09	0.059	0.072			0.0720
	6.26	0.151	0.124			0.1209
	8.70	0.302	0.144			0.1375
	9.59	0.430	0.128			0.1265
	10.17	0.522	0.112			0.1118
	10.79	0.587	0.094			0.0993
	11.64	0.641	0.082			0.0878
	12.41	0.674	0.074			0.0804
	13.18	0.699	0.072			0.0746
	14.03	0.721	0.068			0.0694
	14.61	0.742	0.066			0.0644
	15.23	0.746	0.064			0.0633
	15.73	0.755	0.060			0.0611
	15.97	0.759	0.060			0.0602
	16.39	0.766	0.060			0.0585
	16.70	0.771	0.058			0.0573
17.36	0.781	0.056	0.0549			

APPENDIX D-VIRTUAL EXPERIMENT

Virtual experiments have been conducted to estimate the uncertainties in system volume (dose cell volume, and uptake cell volume), adsorbent volume and excess adsorption. This section describes the procedure on how to perform virtual experiment as well as their assumptions.

D.1 Selection of apparatus size

As mentioned in Section 4.4.1, there are three apparatus size that were available in designing the manometric system, such as 400 cm³, 150 cm³ and 75.6 cm³. It is believed that apparatus size could affect results in excess adsorption; therefore, three virtual experiments have been conducted to determine the best size for our system.

In each of these virtual tests, there are two separate parts that solve for volume ratio (between uptake cell and dose cell), volume ratio in empty system (part 1) and volume ratio with a known reference volume (part 2). There are several assumptions have been made (1) uncertainty of pressure gauge in both parts is the same, up to 0.25% (2) an ideal gas law has been applied to calculate for gas density because helium gas characteristic (3) Cumulative error neglect in the calculation (4) Uncertainty in reference volume is the same for all three virtual experiments. The following example is demonstrated virtual experiment in system volume of 400cc.

Part 1- Volume ratio in empty system-400 cm³

- 1) Create a list of pressure in dose cell. In this example, dosing pressure is increasing at incremental of 10 bars (145 psi) and reach maximum of 50 bars (725 psi).
- 2) The testing temperature is assumed to be 298.15 °K or (25 °C)
- 3) Next, dosing pressure is tasked with a range of uncertainty within +/- 0.25%. This is known as P_{DR_error}
- 4) Using ideal law equation, uncertainty in dosing density can be obtained. This is known as ρ_{DR_error}
- 5) Next, using Equation D.1, uncertainty in equilibrium density can be obtained. This is known as ρ_j_error . Note that Equation D.1 is derived from Equation A.7.

$$\rho_j = \frac{\rho_{DC,j}V_{DC} + \rho_{j-1}V_{SC}}{V_{DC} + V_{SC}} \quad (D.1)$$

- 6) Uncertainty in volume ratio between uptake volume and dose volume can be determined using Equation A.7.

Part 2- Volume ratio with reference volume-400 cm³

- 1) Create a list of pressure in dose cell. In this example, dosing pressure is increasing at incremental of 10 bars (145 psi) and reach maximum of 50 bars (725 psi).
- 2) The testing temperature is assumed to be 298.15 °K or (25 °C)
- 3) Next, dosing pressure is tasked with a range of uncertainty within +/- 0.25%. This is known as P_{DR_error}
- 4) Using ideal law equation, uncertainty in dosing density can be obtained. This is known as ρ_{DR_error}
- 5) Since system volume is 400 cm³, reference volume is 50 cm³. Note that reference volume varies in different system volume.
- 6) Next, using Equation D.2, uncertainty in equilibrium density can be obtained. This is known as ρ_{j_error} . Note that Equation D.2 is derived from Equation A.9

$$\rho_j = \frac{\rho_{DC,j}V_{DC} + \rho_{j-1}(V_{SC} - V_R)}{V_{DC} + V_{SC} - V_R} \quad (D.2)$$

- 7) Using the uncertainty volume ratio result obtained from Part 1, dose cell volume can be determined using Equation A.9.
- 8) Next, uptake cell volume can be obtained using the result from dose cell.
- 9) Finally, the uncertainty in adsorbent volume can be determined using Equation A.10.

The result of part 1 and 2 for volume system of 400 cm³ can be seen in Table D.1 and D.2, respectively. Using the same approach, uncertainty in dose cell volume, uptake cell volume, and adsorbent volume for 150 cm³ and 75.6 cm³ can be obtained. It is concluded that system volume of 75.6 cm³ has the least standard deviation in dose cell, uptake cell, and adsorbent volume.

Table D.1: An example of virtual experiment in an empty volume system to determine volume ratio. This example is conducted for 400 cm³ volume system

Step 1	Step 2	Step 3	Step 4			Step 5		Step 6
Dosing pressure, P _{DR} (bar)	Temperature (°K)	Uncertainty in dosing pressure, P _{DR_error} (bar)	Uncertainty in dosing density, ρ _{DR_error} (mol/L)	True dosing density, ρ _{DR} (mol/L)	True equilibrium density, ρ _j (mol/L)	Uncertainty in equilibrium density, ρ _{j_error} (mol/L)	True volume ratio (%)	Uncertainty in Volume ratio (%)
10	298.15	9.982	0.403	0.403	0.061	0.061	5.609	5.621
20	298.15	20.000	0.807	0.807	0.174	0.174	5.609	5.609
30	298.15	29.963	1.209	1.210	0.331	0.330	5.609	5.619
40	298.15	39.991	1.613	1.614	0.525	0.525	5.609	5.611
50	298.15	49.999	2.017	2.017	0.751	0.750	5.609	5.609

Table D.2: An example of virtual experiment in a system with reference volume to determine dose volume and uptake volume. This example is conducted for 400 cm³ volume system

Step 1	Step 2	Step 3	Step 4	Step 5	Step 6	Step 7	Step 8	Step 9
Dosing pressure, P _{DR} (bar)	Temperature (°K)	Uncertainty in dosing pressure, P _{DR_error} (bar)	Uncertainty in dosing density, ρ _{DR_error} (mol/L)	Reference Volume, V _R (cm ³)	Uncertainty in equilibrium density, ρ _{j_error} (mol/L)	Uncertainty in dose volume, V _{DC} (cm ³)	Uncertainty in uptake volume, V _{DR} (cm ³)	Uncertainty in adsorbent volume, V _R (cm ³)
10	298.15	9.9821	0.4027	45.9854	0.0688	59.6	335.0	6.00
20	298.15	20.0003	0.8068	45.9854	0.1951	60.2	337.4	5.99
30	298.15	29.9629	1.2088	45.9854	0.3684	59.8	335.9	6.00
40	298.15	39.9914	1.6133	45.9854	0.5815	59.9	336.2	5.99
50	298.15	49.9992	2.0171	45.9854	0.8269	60.4	338.9	6.00

D.2 Uncertainty in excess adsorption isotherm

This section describes step by step of how to obtain uncertainty of excess adsorption isotherm. The following example is conducted on New Albany shale. As mentioned before, uncertainty in excess adsorption is only accounted for uncertainty in dose cell, uptake cell and adsorbent volume. Cumulative error in gas density is ignored.

- 1) Create a list of dosing pressure
- 2) Determine dosing density using equation of state
- 3) Solve for the amount of gas in dose cell
- 4) Solve for the amount of gas and equilibrium density after CO₂ expansion. This can be done by using adsorption isotherm equation
- 5) Using equilibrium density, equilibrium pressure can be determined through EOS
- 6) Error analysis is then performed to determine uncertainty in excess adsorption at each pressure step using Equation A.13.
- 7) Percentage error is then determined using Equation D.3.

$$\sigma x = \frac{x_1 - x_o}{x_o} \quad (\text{D.3})$$

The input parameter used in this example can be seen in Table D.3. Table D.4 contains the calculation and results for the example. The uncertainty of excess adsorption can be seen in Figure D.1

Table D.3: Input parameters used to determine uncertainty in excess adsorption of New Albany shale

Solid weight (g)	50
Solid density, ρ_s (g/cm ³)	2.6
Standard deviation in dose volume (cm ³)	0.02
Standard deviation in uptake volume (cm ³)	0.7
Standard deviation in adsorbent volume (cm ³)	0.1
Saturation capacity, q_{sc} (mmol/cm ³)	0.765
b (cm ³ /mmol)	0.212
Temperature (°C)	55
Uncertainty in pressure gauge(%)	0.05

Table D.4: Calculation and results of excess adsorption in New Albany shale using virtual test

Step 1		Step 2	Step 3	Step 4			Step 5		Step 6	Step 7
Dosing pressure, P_{DR} (bar)	Temperature ($^{\circ}K$)	Dosing density, ρ_{DR} (mol/L)	Amount of gas in dose cell (mol)	Amount of gas at equilibrium (mol)	goal seek (mol)	Equilibrium density, ρ_i (mol/L)	Equilibrium pressure, P_j (bar)	Excess adsorption (mmol/g)	Uncertainty in excess adsorption (mmol/g)	Percentage error (%)
10	328.2	0.381	4.719	4.719	4.719	0.073	0.073	0.0043	0.0002	5.0484
20	328.2	0.793	9.831	13.639	13.639	0.213	5.6646	0.0119	0.0005	3.8606
30	328.2	1.244	15.423	26.427	26.427	0.413	10.793	0.0221	0.0007	3.3687
40	328.2	1.743	21.613	42.924	42.924	0.672	17.133	0.0340	0.0011	3.1284
50	328.2	2.304	28.572	63.166	63.166	0.991	24.49	0.0468	0.0014	3.0238
60	328.2	2.947	36.548	87.422	87.422	1.376	32.734	0.0599	0.0018	3.0126
70	328.2	3.704	45.935	116.297	116.297	1.836	41.726	0.0730	0.0022	3.0812
80	328.2	4.627	57.379	150.910	150.910	2.389	51.421	0.0855	0.0028	3.2347
90	328.2	5.807	72.001	193.280	193.280	3.070	61.784	0.0972	0.0034	3.4984
100	328.2	7.386	91.591	246.798	246.798	3.934	72.742	0.1075	0.0042	3.9293
110	328.2	9.428	116.901	314.915	314.915	5.038	83.857	0.1152	0.0053	4.5976
120	328.2	11.464	142.154	394.599	394.599	6.333	93.755	0.1188	0.0065	5.4644
130	328.2	12.982	160.977	477.040	477.040	7.677	101.63	0.1180	0.0076	6.4104
140	328.2	14.053	174.257	556.096	556.096	8.969	107.95	0.1142	0.0084	7.3857
150	328.2	14.849	184.128	629.010	629.010	10.161	113.49	0.1087	0.0091	8.3817

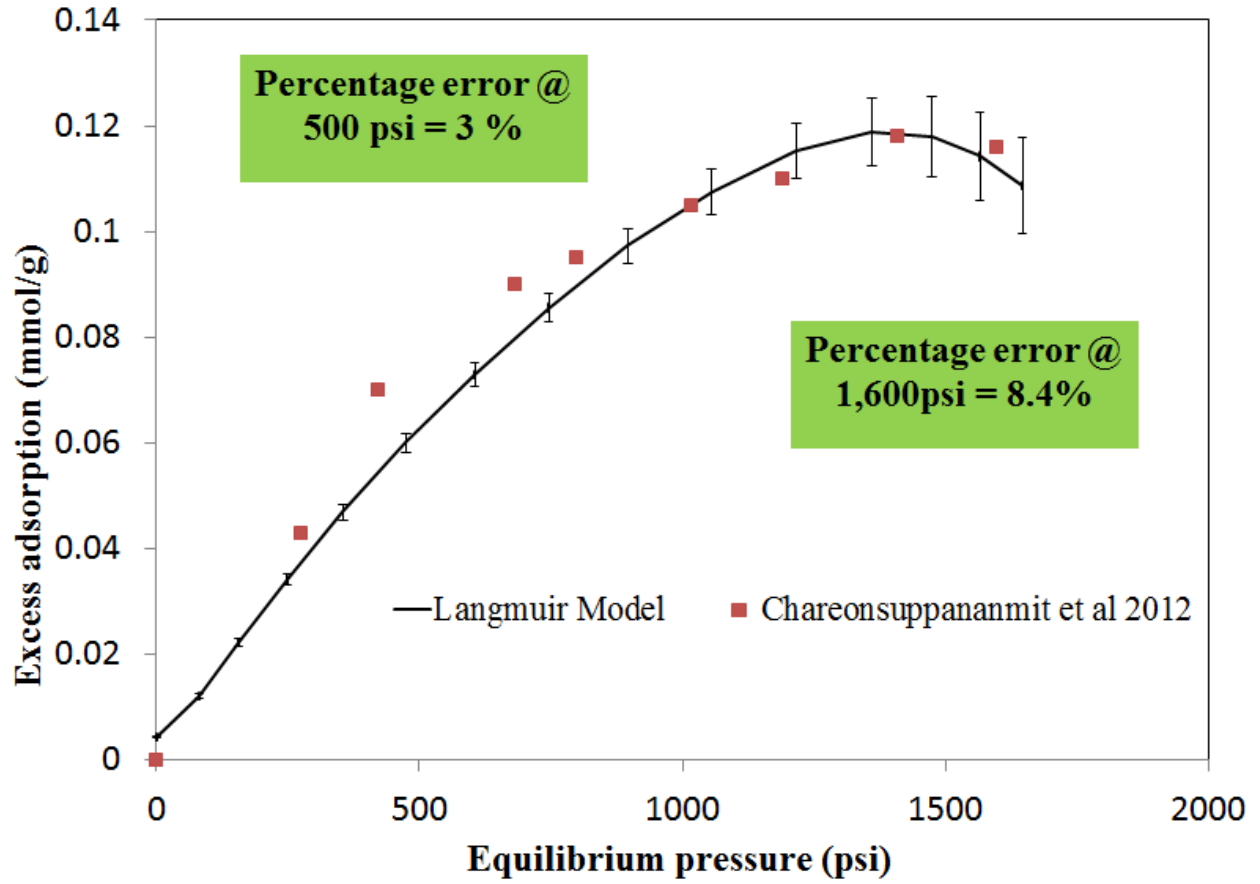


Figure D.1: Uncertainty in excess adsorption for New Albany shale using virtual test.